

Science case: FIREBALL at HiRadMat – Run 3

E. E. Los¹, G. Gregori¹, A. Dyson¹, B. T. Huffman¹, H. Ramm¹, S. Sarkar¹, S. Zhang¹, V. Stergiou^{1, 2}, N. Charitonidis², A. Goillot², P. Alexaki^{2,3}, C. D. Arrowsmith⁴, D. H. Froula⁴, J. W. D. Halliday⁵, R. Bingham^{5,6}, P. J. Bilbao⁷, F. D. Cruz⁷, L. O. Silva⁷, J. T. Gudmundsson^{8,9}, B. Reville¹⁰, T. Vieu¹⁰, C. P. Ridgers¹¹, P. Simon¹², A. G. R. Thomas¹³, L. Willingdale¹³, M. Bochmann¹⁴, and K.-G. Schlesinger¹⁴

¹Department of Physics, University of Oxford, Parks Road, Oxford, OX1 3PU, UK

²European Organization for Nuclear Research (CERN), CH-1211, Geneva 23, Switzerland

³National Kapodistrian Univ. of Athens, Zografou, Attiki, Greece

⁴University of Rochester Laboratory for Laser Energetics, Rochester, NY, 14623, USA

⁵STFC Rutherford Appleton Laboratory, Chilton, Didcot, OX11 0QX, UK

⁶Department of Physics, University of Strathclyde, Glasgow, G4 0NG, UK

⁷GoLP/Instituto de Plasmas e Fusão Nuclear, Instituto Superior Técnico, Universidade de Lisboa, 1049-001, Lisboa, Portugal

⁸Science Institute, University of Iceland, Dunhaga 3, IS-107, Reykjavik, Iceland

⁹Division of Space and Plasma Physics, School of Electrical Engineering and Computer Science, KTH Royal Institute of Technology, SE-100 44, Stockholm, Sweden

¹⁰Max-Planck-Institut für Kernphysik, Saupfercheckweg 1, D-69117, Heidelberg, Germany

¹¹Department of Physics, York Plasma Institute, University of York, York, YO10 5DD, UK

¹²GSI Helmholtzzentrum für Schwerionenforschung GmbH, Planckstraße 1, 64291, Darmstadt, Germany

¹³The Gérard Mourou Center for Ultrafast Optical Science, University of Michigan, Ann Arbor, Michigan 48109, USA

¹⁴BoS GmbH / OuSoCo, Mörbisch am See 7072, Austria

November 25, 2024

1 Proposal Summary

We propose a campaign at HiRadMat which represents the third phase of the platform ‘FIREBALL’, which we have developed to produce dense electron-positron pair beams suitable for studies of processes in a variety of astrophysical environments.

In the first campaign (Fireball 1, or HRMT-62) we demonstrated the capability to produce pairs to address questions in astrophysics concerning the stability of astrophysical jets in ambient plasmas. Specifically, we were able to use the experiment to estimate bounds of the growth rate of beam instabilities related to blazar jets propagating through cosmic void. The apparent stability of the beams in this astrophysical case raises questions about the magnetic fields present in cosmic voids, challenging our understanding of how these fields can be generated. Fireball 1 led to two publications submitted to Nature journals; one paper characterizes the electron-positron beam produced, showing orders of magnitude higher pair yield than previous and future planned experiments (Nat. Commun. **15**, 5029, 2024), and a second paper applies measurements of the beam instability to the astrophysical case of blazar jets (under review in Nature Physics). In the second campaign of FIREBALL (Fireball 2, or HRMT-64), a permanent quadrupole triplet was used to focus the pair beam, and the sensitivity of the Faraday diagnostic was improved. Using this platform, ≈ 2 mT self-generated magnetic fields were measured for the first time. In addition, we studied the energy deposition of relativistic proton beams onto meteorite materials to study asteroid deflection techniques. A third paper has been recently submitted to Nature Communications to describe these results. In the hereby proposed new FIREBALL campaign (Fireball 3, or HRMT-68) we will continue the investigations of HMRT-64 but significantly advance them. We will increase the length of the plasma cell by a factor of 3, allowing the plasma instability growth to enter the non-linear regime. We will field additional diagnostics to measure the spectrum of synchrotron emission and the optical

transition radiation emitted as the pair beam passes through a metal foil. The Faraday rotation diagnostic used to measure the magnetic fields will be supplemented by two b-dot probes. These new measurements will allow the longitudinal pair beam density profile to be measured; as well as provide insight into the plasma instabilities and related radiation mechanisms which are predicted to be central to gamma-ray burst radiative processes.

We will continue the investigation started in HRMT-64 of proton energy deposition into iron-meteorites by using high-energy protons. In the HRMT-64 the meteorite experiment took part as a parasitic proof-of-principle experiment. The sample was irradiated with 440 GeV protons delivered by the SPS. Laser Doppler Vibrometry was utilized to measure the thermally induced stress waves produced by energy deposition in the sample, in real-time. In the experiment we found that one can deposit more energy into the asteroid non-destructively than one would assume from the material parameters measured before irradiation. In HRMT-68 we plan to increase the proton fluence further. We expect this to induce a solid-to-solid phase transition (from centre-cubic to hexagonal) that has important implications in the way momentum is transferred to the sample.

This Science Case contains calculations and simulations for the proposed experiments and a discussion of their practical implementation.

Contents

| | | |
|----------|--|-----------|
| 1 | Proposal Summary | 1 |
| 2 | Scientific Case | 4 |
| 2.1 | Motivation and experimental Goals | 4 |
| 2.1.1 | Physics of relativistic pair beams | 4 |
| 2.1.2 | Asteroid deflection by relativistic proton beams | 5 |
| 2.2 | Complementary nature of Fireball and Meteorite campaigns | 5 |
| 2.3 | Experimental Scheme | 6 |
| 2.3.1 | Fireball | 6 |
| 2.3.2 | Meteorite | 6 |
| 2.4 | Changes from HRMT-64 campaign | 7 |
| 2.4.1 | Increased plasma cell length | 7 |
| 2.4.2 | Target design | 8 |
| 2.4.3 | Longitudinal pair beam density measurement | 8 |
| 2.4.4 | B-dot probes | 8 |
| 2.4.5 | Synchrotron emission | 8 |
| 2.4.6 | Meteorite target | 8 |
| 2.5 | Simulations | 8 |
| 2.5.1 | Monte-Carlo simulations | 8 |
| 2.5.2 | Particle-in-cell simulations: plasma instabilities | 10 |
| 2.5.3 | Particle-in-cell simulations: optical transition radiation | 10 |
| 2.5.4 | Particle-in-cell simulations: synchrotron emission | 11 |
| 3 | Experimental setup | 12 |
| 3.1 | Introduction to HiRadMat facility | 12 |
| 3.2 | Experimental Layout | 12 |
| 3.3 | Target envelope implementation | 13 |
| 3.4 | Plasma discharge | 13 |
| 3.5 | Meteorite | 14 |
| 3.5.1 | HRMT-64 Results | 14 |
| 3.5.2 | HRMT-68 meteorite target and other changes compared to previous experimental run | 15 |
| 4 | Diagnostics | 16 |
| 4.1 | Luminescent screens | 16 |
| 4.2 | Magnetic field diagnostics | 17 |
| 4.2.1 | Faraday rotation | 17 |
| 4.2.2 | B-dot probes | 19 |
| 4.3 | Pair spectrometer | 19 |
| 4.4 | Optical transition radiation | 21 |
| 4.5 | Synchrotron radiation | 21 |
| 4.6 | Diagnostics for meteorite target | 22 |
| 5 | Pulse list | 22 |

2 Scientific Case

2.1 Motivation and experimental Goals

2.1.1 Physics of relativistic pair beams

The environmental conditions in the magnetospheres of pulsars, magnetars and black holes are known to present sites of copious electron-positron pair production [1, 2, 3, 4, 5, 6], and the outflows from these compact objects, in the form of winds or collimated jets, are inevitably pair-plasma enriched. Gamma-Ray Burst (GRB) fireballs [7, 8] represent an extreme example of energetic pair-dominated particle jets, with GRB being among the most luminous events in the universe; the total energy released, in only a few tens of seconds, can exceed that of the entire Milky-Way Galaxy over several years. GRB fireballs have been proposed as engines capable of powering cosmic-rays to the highest energies, of which the acceleration processes and propagation through the cosmos to arrival at Earth remain among the greatest puzzles in high-energy astrophysics. Understanding the transport and stability of energetic particle beams through an ambient plasma is crucial for modelling both the energy dissipation mechanisms that determine the radiative signatures we observe from Earth, as well as the acceleration mechanisms responsible for generating the highest energy particles in the universe. It is commonly suggested that GRB emission results from the synchrotron radiation of relativistic particles energised at internal shocks [9, 10], but the precise mechanisms responsible are not yet fully understood. In both prompt and afterglow GRB emission, it is expected that filamentation beam-plasma instabilities [11, 12, 13] play a role in the growth of magnetic fields associated with synchrotron emission [14, 15]. In these instabilities, relatively strong magnetic fields can develop due to the separation of streaming electron-positron pair beams into current filaments of electrons and positrons. Numerical simulations have suggested that the required field strengths can be amplified in the kind of relativistic collisionless shocks expected to be relevant to GRBs [16, 17]. But, inferences are based on crude energy equipartition arguments, and idealised simulations which are constrained by the ability of numerical techniques to fully capture the extreme conditions in GRB outflows, and suffer from limited spatial and temporal resolution. Experimental platforms which can complement numerical simulations, in exploring the non-linear aspects of beam-plasma instabilities for a range of compositions and densities of beam and background plasmas, are crucial for the verification of models of microphysics that are relied upon to understand extreme astrophysical phenomena such as gamma-ray bursts.

In a recent article [18], we introduced an experimental scheme for generating quasineutral electron-positron beams using 440 GeV/c protons at HiRadMat [19]. This offers a fundamentally different approach of generating pair beams from alternative experimental approaches, in which pairs are generated through the interaction between relativistic electron beams and a high-Z converter material via Trident and Bethe-Heitler processes [20, 21, 22, 23, 24]. We have validated Monte-Carlo simulations that demonstrate the generation of beams at HiRadMat containing $10^{13} - 10^{14}$ electron-positron pairs, several orders of magnitude larger than previous experiments which have produced beams containing approximately 10^8 pairs using laser-wakefield-accelerated electron beams of 10^9 electrons [20, 21, 22, 23, 24].

The characteristics of the generated pair beams lend themselves promisingly to the prospect of an experiment at HiRadMat in which filamentation instabilities can be observed as they propagate through a ~ 1 m long plasma. Namely, the pair beams have a small enough divergence that high beam densities, exceeding 10^{11} cm^{-3} , are maintained for tens of centimetres of propagation. This is important so that the growth rate of filamentation instabilities can remain high enough for them to significantly develop. Additionally, the beams will have durations of hundreds of ps, meaning they extend longitudinally over multiple skin depths of the plasma, allowing longitudinal and obliquely-growing modes of filamentation instability to develop. In the shorter beams of previous experiments where beam duration is no more than 0.1 – 1 ps, these modes are suppressed [23], and we cannot observe the competition with transverse filamentation modes that are expected to affect the growth and saturation of magnetic fields. By demonstrating the experimental feasibility of isolating and studying collisionless beam-plasma instabilities that are presently limited to numerical experiments, we open up the possibility of performing plasma physics experiments at CERN that investigate processes of magnetic field generation which have relevance to many extreme astrophysical environments.

Here we propose an experimental campaign to investigate the microphysics of the fireball model at the HiRadMat facility. We aim to investigate the onset, growth and saturation of the two-stream, oblique and current filamentation instabilities which perturb an electron-positron beam propagating through a background plasma. On our previous campaign, the magnetic fields generated by the current filamentation instability were successfully measured using a Faraday rotation diagnostic. We will build on these results in our next campaign. In the Fireball 3 campaign, we will study the growth of and competition between the two-stream (TS), current filamentation (CFI) and oblique (OBI) instabilities in a longer plasma cell, and with a less divergent pair beam. The increased plasma length will enable these instabilities to be studied at a later stage of development, at which the associated magnetic field strengths are higher, and possibly probe the onset of non-linear growth. We aim to measure both the transverse and longitudinal density modulations in the pair beam, which simulations indicate are evident at this later stage of instability growth and observe the synchrotron radiation emitted as

the pair beam interacts with the magnetic fields.

2.1.2 Asteroid deflection by relativistic proton beams

Understanding the material properties of metal-rich asteroids is of central interest to the study of the planetary core of the Earth [25] and super-Earth exoplanets [26, 27] (as exemplified by NASA’s mission to metallic asteroid 16 Psyche [28]), as well as advanced material science [29, 30, 31, 32, 33, 34] and proposed asteroid deflection concepts, such as employing a kinetic impactor - as it was tested in NASA’s DART mission [35], and intense irradiation through the use of nuclear explosive devices. In the case of the latter, proposed asteroid deflection concepts require the dynamical behavior of asteroid material to be known precisely to model deflection orbits accurately and to predict the efficiency of energy transfer onto the object. In particular, the material behavior when exposed to high energy particle irradiation or large thermal energy deposition must be known.

On Earth, iron meteorites provide samples originating from metal-rich asteroids, and while there exists an extensive body of measurements conducted on such materials, many studies (such as Ref. [36]) explore the properties of cold samples and not material under or after high-energy treatment. In Jain et al. [37], asteroid material response to stresses induced from very high energy/pressure of asteroid collisions is studied from 119 meteorite samples (though the analysis concerns reconstructing billion-year-old events), and in the comprehensive material analysis of Siraj et. al. [38] material strength of meteors that are destroyed in the atmosphere is derived from the ram pressure, but real-time dynamic material responses cannot be determined from either of these studies. Laboratory experiments performed at Sandia National Laboratories used a Z-pinch pulsed power facility to measure the transfer of momentum to meteorite samples when irradiated with soft X-rays, mimicking the localized surface energy deposition expected to be achieved with an actual nuclear device [39], however the destructive nature of the tests did not allow any form of material response to be measured. Finally, more recently, Moore et al. [40] achieved a breakthrough with the first measurement of the entire transfer of momentum imparted onto a scaled asteroid in a lab-based environment, covering the total momentum transfer and not only the momentum carried by the shock wave. However, the experimental setup did not allow any direct form of material response to be recorded since those tests were destructive. It should be noted that the momentum transfer changes as a function of the material properties, which can change under high-energy irradiation.

In our previous campaign (HRMT-64), we conducted an experiment at the High-Radiation-to-Materials (HiRadMat) facility of the European Organization for Nuclear Research (CERN) [41] in which a meteorite sample was exposed to a high intensity of high-energy radiation and the dynamical response of momentum transferred to the sample was precisely measured in real-time. Using Laser Doppler Vibrometry (LDV), we have recorded the thermally induced stress waves produced by energy deposition in the sample. Our initial results suggest that one can deposit much higher amounts of energy into asteroid material without destruction than one would assume from the material parameters as measured before high-energy irradiation. This has important implications for proposed asteroid deflection techniques. The strain-dependent damping behavior observed in the experiment prevents resonant self-destruction of the asteroid material (see [31]), and thus our results suggest that high-energy irradiation could not only harden metal-rich asteroid material but also turn it into new materials comparable to composites with advanced properties [31, 32, 33, 34, 42]). This was not entirely unexpected. That the material of metal-rich asteroids shows properties of composites was also suggested in Ref. [42]. However, in our previous campaign, we were unable (due to the proton flux limitation) to drive the sample material to sufficiently higher stress values that would result in solid-solid phase transitions, which is expected for these materials [37]. This is the focus of the new campaign (HRMT-68) we propose here.

2.2 Complementary nature of Fireball and Meteorite campaigns

In the HRMT-68 campaign, the target design has been chosen to optimise the pair beam absolute density and relative density to the proton beam after \sim m beam propagation. Therefore, a key aspect of the target design is that the generated pair beam has minimal divergence. Graphite was chosen both as this has a high interaction cross-section for protons, and as carbon is a relatively low-Z material. Thus Coulomb scattering of pairs, and hence pair beam divergence, is relatively low, and proton depletion is high, fulfilling both of our requirements. By contrast, as the meteorite target is comprised of high-Z elements, a more divergent pair beam would be produced during the proton beam interaction with the target. The proton density exiting the target would also be higher compared to the graphite target. By comparing the instability growth rates for the two target configurations, we will investigate the effect of changing the relative densities of the proton and pair beams on instability growth. This will allow us to study a key outstanding question in the Fireball model of GRBs: the importance of Baryon loading on the instability growth rate. This is critical as the Fireball model requires pair jets to have a baryon component with a narrowly constrained density relative to that of the pair beam.

2.3 Experimental Scheme

2.3.1 Fireball

For an extensive description of the results obtained in the previous Fireball campaigns, we have attached at the end of this report a copy of a paper we have recently submitted for publication.

An overview of the next fireball experiment for the study of beam-plasma instabilities is provided in figure 1. The experiment will use the 440 GeV proton beam from SPS, containing up to 5×10^{11} particles, which is directed into the HiRadMat experimental area (TNC). The proton beam enters a graphite target, instigating a hadron shower comprised of various secondaries, including neutral pions, π^0 , which rapidly decay into gamma photons, γ . The gamma photons interact with the Coulomb fields in the target, producing electron-positron pairs via the Bethe-Heitler process. Electrons and positron may generate additional pairs via the trident process. The relativistic pair beam propagates through a low-density ($2 \times 10^{12} \text{ cm}^{-3}$) Ar plasma, produced using

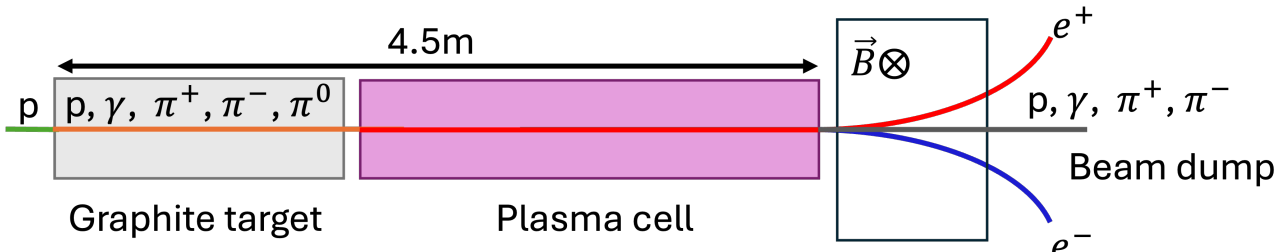


Figure 1: Overview of the fireball setup. A proton beam incident on a graphite target induces a hadron shower. The neutral pion, π^0 , products decay to gamma photons, γ , which produce electron positron pairs via the Bethe-Heitler (and subsequently trident) process when interacting with the Coulomb fields in the target. The pair beam interacts with a low density plasma, seeding instabilities with associated magnetic fields. Following the plasma cell, an electromagnet disperses the pairs onto a detector, while the hadrons deposit their energy in the beam dump.

an inductively-coupled RF discharge. Density perturbations in the beam (equivalent to currents, due to the relativistic motion of the beam) have associated magnetic fields. As the beam propagates through the plasma, the magnetic fields, which are amplified by the plasma response, act to reinforce the initial non-uniformities in the e-e+ relative density, eventually causing the beam to filament.

We aim to measure the growth rates of different plasma instabilities and the strength of their associated magnetic fields. We also seek to study the density modulations in the pair beam which result from these instabilities, and the synchrotron radiation produced when the pairs interact with the magnetic field. Using the scale-invariant properties of these processes, we can map the experimental results to astrophysical GRBs to better understand how their evolution affects observations.

2.3.2 Meteorite

For the part of the experiment which involves the proton energy deposition into a meteorite sample, we will use a very similar design with the only difference that the carbon target is replaced by the meteorite sample. This is accomplished by mounting the graphite and the meteorite targets on a vertical translation stage. We note that while the energy deposition on the meteorite is measured using LDV, the hadronic shower that is developed inside the sample will produce a beam of electrons and positrons that is similar to what we previously on HRMT-64 and thus it will also provide an important comparison point (particularly regarding beam divergence and pair density – see above) against the graphite only converter.

It is common for meteorite samples to be composed of multiple phases of iron-nickel alloy. The fragment utilized in HRMT-64 (imaged in Figure 2) was taken from the Campo del Cielo iron meteorite and it featured a characteristic two-phase crystal structure consisting of Kamacite, i.e., ferritic iron (α structure), and Taenite, i.e. Austenite (γ structure) [43]. Once cut into a cylindrical shape, the phase boundaries become clearer (not to be confused with cracks). Scanning electron microscopy (SEM) and energy-dispersive X-ray spectroscopy reveals small deposits of Schreibersite along the phase boundaries, characterized by a higher phosphorous content. Given the multiple-phase composition, the homogeneity of the dynamical material response, such as the stages of material hardening, affects the efficiency that kinetic energy can be transferred to the sample before it is destroyed [39], as well as the general predictability of the material behavior. If the dynamical material response is inhomogeneous, induced stress waves can take preferred directions depending on ppm-level inclusions [37], making the material behavior unpredictably complex. In contrast, homogeneous hardening can be experimentally controlled, despite the challenge of predicting a dynamical set of material variables, such as yield strength. Modelling the precise deflection orbit of an asteroid is one example where prediction of the material behavior

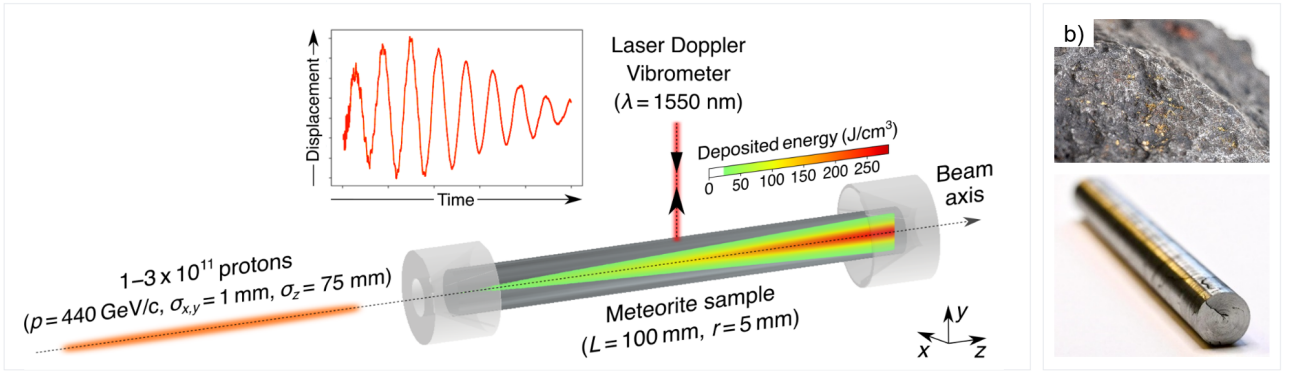


Figure 2: a) Protons with momenta 440 GeV/c are extracted from CERN’s Super Proton Synchrotron in a Gaussian-shaped bunch ($\sigma_{x,y} = 1 \text{ mm}$, $\sigma_z = 75 \text{ mm}$) containing $1 - 3 \times 10^{11}$ protons. The cylindrical meteorite sample ($L = 100 \text{ mm}$, $r = 5 \text{ mm}$) is held in the beam path using conical supports and irradiated along its central axis. The protons generate hadronic and electromagnetic showers of secondary particles that deposit thermal energy via ionization losses in a quasi-adiabatic fashion. The super-imposed colormap shows the expected energy deposition profile obtained from a Monte Carlo simulation (see Methods) when the sample is irradiated with 3×10^{11} protons. Radial vibrations and deformation of the sample due to the induced thermal stress are measured in real-time using a laser to perform Laser Doppler vibrometry (LDV) with $\lambda = 1550 \text{ nm}$ wavelength. b) Campo del Cielo meteorite: surface of raw sample (top) and sample cut into a cylindrical shape (bottom)

plays such a crucial role.

The dynamical response and development of yield strength of asteroid material was examined for the first time experimentally in the HRMT-64 campaign. When such high energy protons collide with atomic nuclei in the sample, hadronization of quarks and gluons leads to the generation of hadronic and electromagnetic cascades of secondary particles. These include (but are not limited to) pions, electrons, positrons, kaons and γ -rays [44, 45], which predominantly lose energy via ionization of atoms in the sample and leads to a fast, isochoric, high-energy deposition that penetrates deeply into the meteorite sample. By measuring the surface vibrations of the sample using Laser Doppler Vibrometry (LDV), the response of the iron meteorite sample resulting from the corresponding thermally-induced stress wave was measured in real time for 27 successive beam irradiations (setup shown in Figure 2). In addition, the gathered material response data have been used to derive the fraction of the primary beam kinetic energy converted into bulk kinetic energy of the sample, providing the momentum transfer. As such, the irradiation of the meteorite sample by the proton beam can also be understood as a laboratory-based surrogate used to test the efficiency of particle beam-based asteroid maneuvers - an entirely new method for asteroid deflection.

The maximum primary proton beam intensity for the meteorite case in HRMT-64 was chosen to be 3×10^{11} protons at 440 GeV in a single-bunch with a Gaussian transverse profile ($\sigma_{x,y} = 1 \text{ mm}$) and duration of $\sigma_t = 250 \text{ ps}$ to study the plastic deformation regime, isolated from solid-to-solid phase transitions, which are intended to be studied in a follow-up experimental campaign at higher intensities. In previous structural analysis of large numbers of meteorites, it was concluded that shocks caused by impacts of colliding asteroids typically lead to transitions to ϵ -phase iron along phase boundaries [37, 43]. Therefore, in the experimental setup, a phase boundary was placed underneath the focal spot of the LDV head to monitor possible preferred directions of the propagation of the induced stress wave. Figure 3 shows the material structure and composition across one of the phase boundaries in another separate piece of the meteorite sample, not utilized for the experiment.

2.4 Changes from HRMT-64 campaign

To facilitate our experimental goals, a number of modifications have been made to the planned campaign, Fireball 3, compared to the previous campaign, Fireball 2, which we summarize below.

2.4.1 Increased plasma cell length

The plasma cell length will be increased from 0.87 m to 3 m. The longer cell will allow plasma instabilities to be investigated at a later stage of development, at which the transverse and longitudinal density modulations in the pair beam and the associated magnetic fields will be more evident.

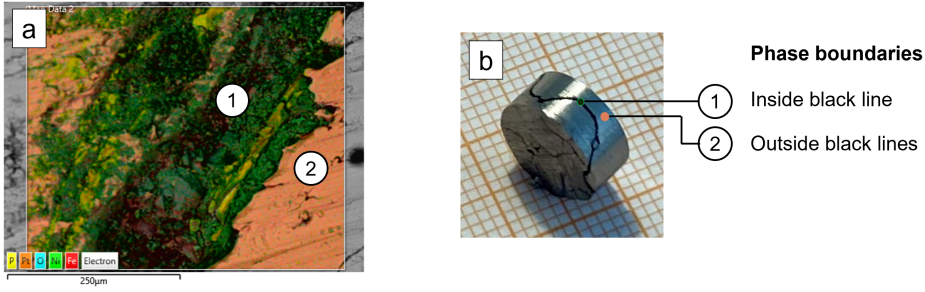


Figure 3: Phase boundary of Campo del Cielo meteorite. The average composition and material characteristics were optically analyzed using scanning electron microscopy (SEM) and energy-dispersive X-ray spectroscopy (EDS). a) SEM-image of phase boundary, b) macroscopic picture of exemplary phase boundary of Campo del Cielo iron meteorite

2.4.2 Target design

The 0.37 m graphite-tantalum target used for Fireball 2 has been replaced with a 1.4 m pure graphite target to maintain a high pair beam to proton beam density ratio 4 m downstream of the target. A pure graphite target also allows the maximum number of incident protons to be increased from 3×10^{11} to 5×10^{11} . This is because of the lower absorption of hadrons (having longer interaction length) and since the pairs that we arrive at the plasma cell are (for the most part) produced at the very end, their intensity is proportional to the proton intensity.

2.4.3 Longitudinal pair beam density measurement

The effect of the two-stream instability on the longitudinal pair beam density will be diagnosed by temporally resolving optical transition radiation generated by the pair beam as it passes through a copper foil.

2.4.4 B-dot probes

Two b-dot probes will be fielded to make time-dependent measurements of the magnetic field strength after 1 m and 3 m of propagation.

2.4.5 Synchrotron emission

The spectrum of synchrotron radiation produced by the pair beam as it interacts with magnetic fields in the plasma will be measured using a gated spectrometer. A comparison between the measured synchrotron radiation and observations of GRBs will provide insight into the validity of the fireball model of GRB generation.

2.4.6 Meteorite target

The most important change compared to HRMT-64 results from the requirement to reach at least 13 GPa of stress in the sample, compared to the 120 MPa in the previous experiment. Since the stress relates quadratically to the beam focus, the aim is to use a beam radius $\sigma_r = 100 \mu\text{m}$ instead of the 1 mm used in HRMT-64. To further increase the stress, we intend to utilize 5×10^{11} protons in a single bunch.

Since the phase transition to a hexagonal lattice is expected to lead to a lower value for the Young's modulus ([46]), the phase transition should be immediately visible on the Fast Fourier Transform (FFT) spectrum of the LDV displacement data. This is the reason why again the LDV head is planned to be used as the crucial diagnostics. As in the previous experiment, it will be supplemented by a PT100 temperature sensor to have control of the temperature development on the meteorite sample surface.

A Monte Carlo simulation using the code FLUKA is ongoing to study the detailed energy deposition profile into the sample at 5×10^{11} protons and the very small focal diameter of $\sigma_r = 100 \mu\text{m}$.

2.5 Simulations

2.5.1 Monte-Carlo simulations

In order to study plasma instabilities over 3 m, it was necessary to re-design the target to ensure that the pair beam to proton beam density ratio, and pair beam absolute density remained high over 3 m propagation after the target.

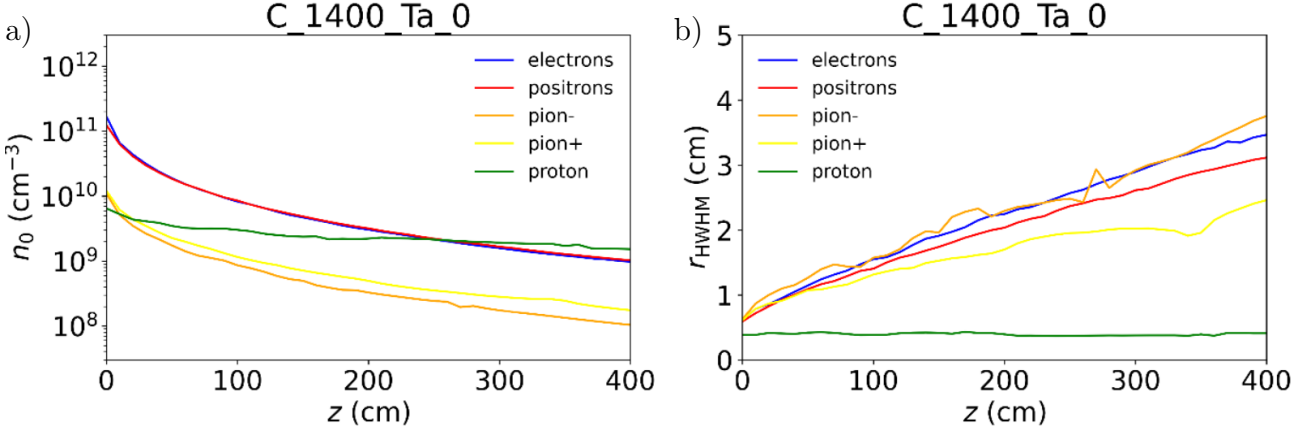


Figure 4: FLUKA simulations for a 3 mm beam of 3×10^{11} protons, incident on a 1.4 m graphite target. a) Density and b) transverse size of the proton and secondary particle beams as a function of propagation distance 0 – 4m after the graphite target.

FLUKA simulations were used to identify a target design which achieved this and produced a quasi-neutral pair beam for a 3 mm diameter proton beam with intensity 3×10^{11} . The optimal target design found to be a 1.4 m graphite target with no tantalum. This design differs substantially from the target used for Fireball 2, which consisted of 0.36 m graphite followed by 10 mm of tantalum. The increased length of the graphite segment further depletes the proton beam, allowing for a higher pair to proton beam density ratio 3 m downstream from the target. The tantalum segment increases both the pair beam yield and divergence. While the boost in pair yield was advantageous for the shorter plasma cell fielded previously, the longer cell in Fireball 3 necessitates a lower beam divergence in order to optimise the pair beam density 3 m downstream. Over such distances, the reduction in pair beam density effected by the higher pair beam divergence more than offsets the higher pair yield. For this reason, a pure graphite target with no tantalum converter will be used.

A further advantage associated with a pure graphite target, as opposed to a composite graphite and Ta target, is the higher conduction coefficient and thermal dissipation of graphite, which allows higher intensity proton beams (up to 5×10^{11}) to be used. The FLUKA simulations for the 1.4 m graphite target are summarised in figures 4 and 5. As seen in figure 4a), the optimal target design ensures the pair beam density exceeds the proton beam density for propagation distances up to 2.5 m downstream of the target, after which the proton and pair beam densities are comparable. Figure 4b) indicates the change in relative density of the pair and proton beams with propagation distance stems from the greater divergence of the pair beam, which causes the transverse size of the pair beam to more than triple after 4 m propagation.

Figure 5 indicates that the pair beam is $> 0.92\%$ neutral 1–4 m after the target. The initial high proportion of electrons stems from the asymmetry of the electron/positron annihilation cross-sections in the target for energies < 10 MeV, which results in a lower proportion of low-energy positrons. The low energy electrons are highly divergent, and thus are lost from the beam after 1 m propagation.

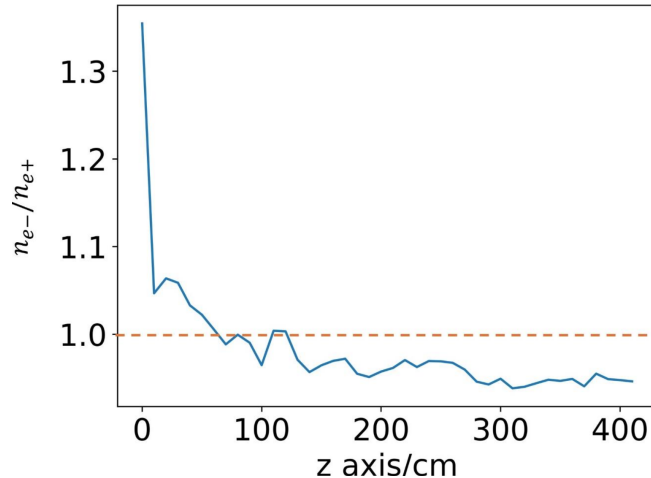


Figure 5: FLUKA simulations of the ratio of electrons to positrons as a function of propagation distance 0 – 4m after the graphite target.

2.5.2 Particle-in-cell simulations: plasma instabilities

The particle-in-cell code, OSIRIS [47], was used to model the plasma instabilities arising from the interaction of the pair beam with the 3 m plasma. For these simulations, a plasma with $2 \times 10^{12} \text{ cm}^{-3}$ density was assumed with a uniform longitudinal profile. The pair beam, comprised of 10^{13} leptons, had a power-law spectrum ranging from $10 - 400 \text{ MeV}$, a longitudinal dimension (1σ) of 7.5 cm, and 2% divergence.

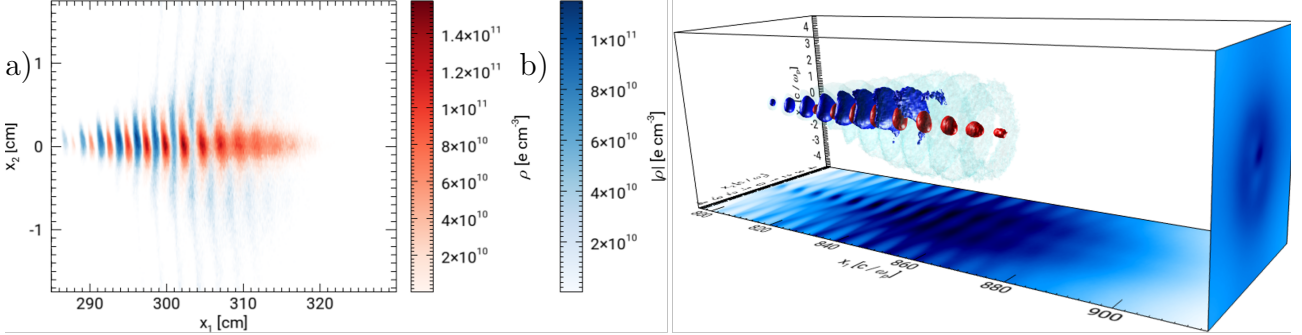


Figure 6: Particle-in-cell simulations of the pair beam density and profile after 11 ns (approximately 11 m) of propagation in the plasma. a) The longitudinal (x axis) and transverse (y axis) dependence of the electron (red) and positron (blue) density. b) An iso-surface of the electron (red) and positron (blue) densities in 3d space.

In figure 6a) and b), the 2D and 3D spatial dependence of the pair beam density are shown, respectively, after 3 m propagation through the plasma. The magnetic field of the proton beam seeds the instability, and determines the filament structure. The electron beam sticks to the proton beam and is thus concentrated in a central filament, while the positrons assume a toroidal structure surrounding the central filament. The resulting difference in divergence may be measured using the pair spectrometer and profile screens. The longitudinal modulation of the electron and positron density and their longitudinal separation results from the two-stream instability. The density modulation scale length $\approx 3 \text{ mm}$ is consistent with the collisionless plasma skin depth of 3.75 mm at a plasma density of $2 \times 10^{12} \text{ cm}^{-3}$.

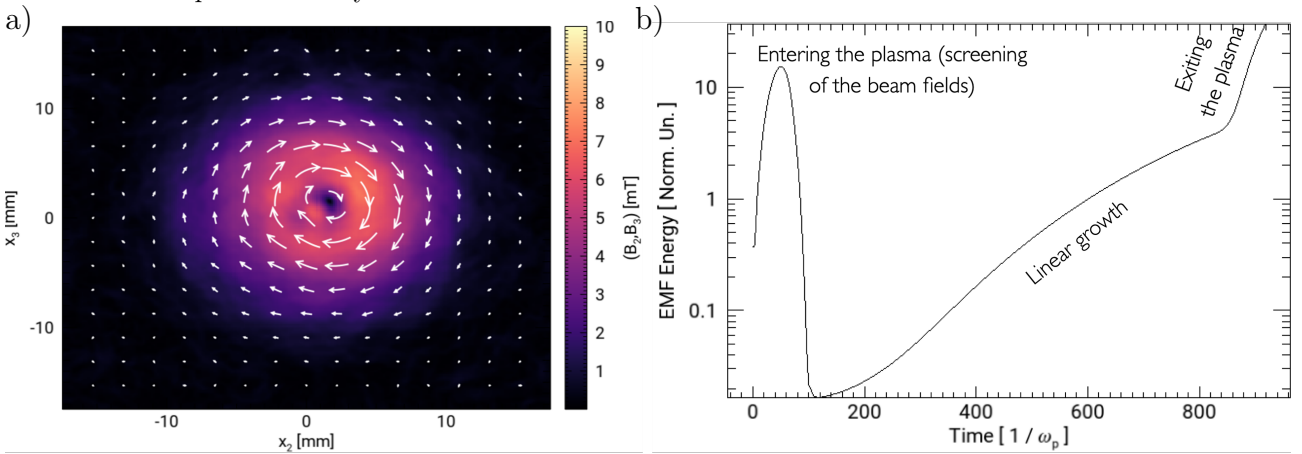


Figure 7: Particle-in-cell simulations of the magnetic fields engendered by plasma instabilities. a) transverse magnetic fields after 3 m plasma propagation. b) Energy of the electromagnetic fields as a function of propagation time in the plasma.

Figure 7a) indicates that 6 mT magnetic field strengths are achievable, approximately two to three times the magnetic field strengths measured in Fireball 2, consistent with an initial linear regime of instability growth and the onset of non-linear growth at later times. This is confirmed by the analysis of the energy in the electromagnetic field shown in figure 7b).

2.5.3 Particle-in-cell simulations: optical transition radiation

The time-resolved incoherent optical transition radiation (OTR) emitted as the pair beam passes through a copper foil situated at the downstream end of the plasma cell will be used to diagnose the longitudinal density profile of the pair beam, which is expected to be modulated by the two-stream instability as illustrated in figure 6.

The particle-in-cell code EPOCH [48] was used to simulate the spectrum, longitudinal and transverse structure of OTR, shown in figure 8. The spectrum is expected to lie in the visible range, between 200 – 1000 nm,

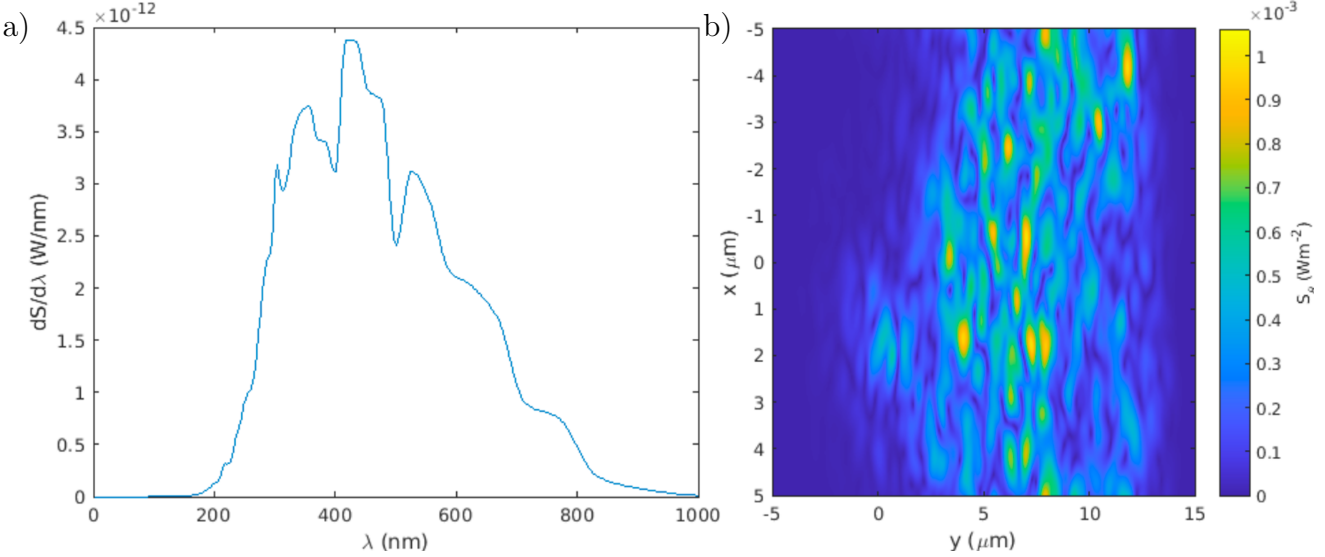


Figure 8: EPOCH simulations of optical transition radiation (OTR) emitted as the pair beam passes through a copper foil placed at the downstream end of the cell. a) The spectrum of incoherent OTR. b) The longitudinal (labelled x) and transverse (labelled y) structure of OTR emission.

with a peak at $\approx 400 \text{ nm}$. EPOCH simulations indicate that the intensity of incoherent OTR will be of order mW m^{-2} for a 10 mm beam of $\approx 1 \text{ ns}$ duration.

Analytic predictions indicate the OTR will be tightly beamed, with 2° angular spread.

2.5.4 Particle-in-cell simulations: synchrotron emission

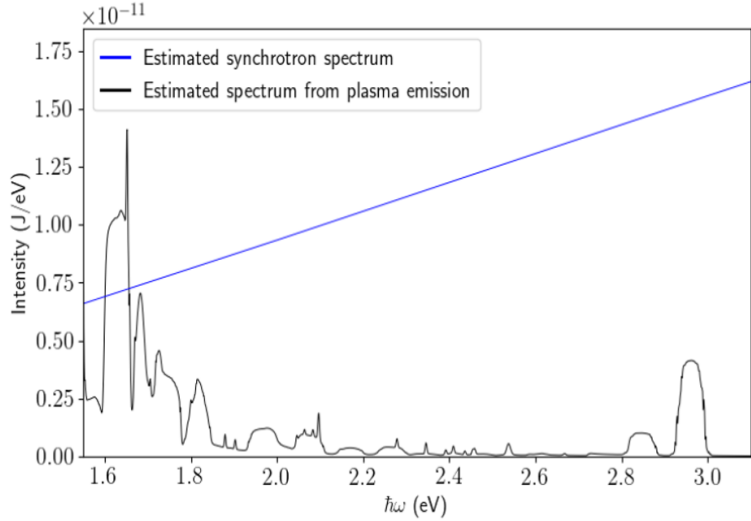


Figure 9: Comparison between the expected synchrotron emission calculated from particle-in-cell simulations, and the expected line emission from the discharge plasma calculated using the PrismSPECT collisional-radiative spectral analysis code. The spectral region shown (from 1.55 – 3.10 eV) corresponds to wavelengths in the visible region of $\lambda = 400 – 800 \text{ nm}$. In the range 2 – 3 eV ($\lambda \simeq 400 – 600 \text{ nm}$), the synchrotron emission appears to be dominant. These simulations assumed a diagnostic exposure time of 2 ns and a collection area of 46 mm^2 .

Synchrotron radiation is emitted by electrons and positrons as they are deflected by the magnetic fields of the current filaments. Emission in the visible region is predicted, with photon critical energies of eV-scale:

$$E_c = \hbar\omega_c = \frac{3}{2}\hbar \frac{eB}{m_e c} \gamma^2 \sim 1.35 \left(\frac{B}{1 \text{ T}}\right) \left(\frac{E}{45 \text{ MeV}}\right)^2 \text{ eV} \quad (1)$$

The radiation is expected to be relativistically beamed along the axis of motion of the pair beam, with an angular spread of $\approx 1^\circ$. Fully 3-dimensional particle-in-cell simulations using the PIC code, OSIRIS, have been used

to estimate the intensity and spectrum of synchrotron emission for a HRMT-62 type experimental setup. The results are shown in figure 9. The intensity of the visible synchrotron radiation emitted by the electron-positron beam is shown for a time $t = 1.75$ ns after entry into the plasma. The collisional-radiative spectral analysis code PrismSPECT was used to simulate the atomic and radiative properties of the discharge plasma, and compare the expected line emission with the synchrotron emission. Simulation of a steady-state, non-LTE, argon plasma was performed with detailed configuration accounting of the visible/UV/EUV transitions for Ar and Ar(I), with the inclusion of bound-bound and bound-free emission. The plasma was modelled with a spherical geometry (2 cm radius), and a two-temperature Maxwellian was assumed. An ideal gas equation of state (with fixed temp at 500 K and pressure at 0.05 mbar) was assumed for the dominant neutral component, while the hot electron component was assumed to have a number density fraction 0.01 and a temperature of 4 eV. The spectral resolution was set as $\lambda/\Delta\lambda = 500$ (a resolution of 1 nm at 500 nm). As expected, it was found that the bound-bound transitions were the dominant source of visible emission, with an intensity around 1×10^{-4} Watt/cm², and stronger at longer visible wavelengths (600–800 nm), which is consistent with the observation of the plasma being pink in hue. In the spectral region 400–600 nm (from 2–3 eV), the synchrotron emission exceeds the line emission from the plasma. This is shown in Fig. 9. To obtain these time-integrated intensities, the synchrotron emission is assumed to last for 800 ps ($\pm 1\sigma$ bunch duration), while the plasma emission assumed to last for 2 ns (the exposure time of the proposed gated-CCD camera). A more detailed analysis will include the absorption of the synchrotron radiation by the plasma, and the synchrotron self-absorption.

3 Experimental setup

3.1 Introduction to HiRadMat facility

An overview of the HiRadMat facility is provided in figure 10. The 440 GeV proton beam from SPS can be extracted into the HiRadMat experimental area. The proton beam has maximum intensity of 5×10^{11} , duration 375 ps and a transverse size at focus which may be varied between 0.1–3 mm using quadrupole electromagnets.

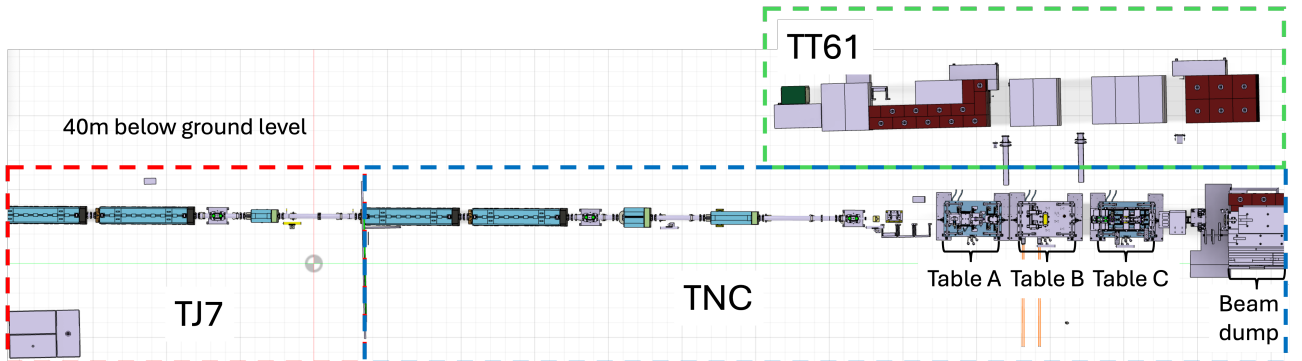


Figure 10: Overview of the HiRadMat facility, showing the three experimental areas, TNC, TT61 and TJ7, the tables on which the experiment is set up, the beam dump, and the permanent radiation shielding.

The HiRadMat facility is located near the Meyrin campus, 40 m below ground level, and consists of three areas; “TNC”, “TT61” and “TJ7”. The primary experimental area, TNC, contains three tables, labeled “A”, “B” and “C” (in order of upstream to downstream), upon which the experiment is set up, followed by the beam dump. The majority of the experiment is constructed at ground level before being lowered by crane into TNC. TT61 and TJ7, which are adjacent to TNC, are separated from TNC by a concrete partition containing multiple feedthroughs, and a metal gate, respectively. Both areas contain shielding blocks or bunkers to protect radiation sensitive equipment from hadron fluence generated as the proton beam interacts with the target and the beam dump.

3.2 Experimental Layout

The experimental layout in TNC and TT61 is summarised in figure 11. The CAD design for the experiment is shown in figure 12. The target is mounted on a telescopic arm on table B which allows it to be driven in and out of the beam. The plasma cell is mounted on a long support arm attached to table C, which extends over table B. The cell will be fixed in place for the duration of the experiment.

The upstream section of the plasma cell (between the first two cross-pieces) is detachable, as is the support on which this section is mounted, allowing table C to be lowered into TNC without collisions. Two luminescent screens, used to image the transverse beam profile, are mounted either end of the plasma cell. The upstream

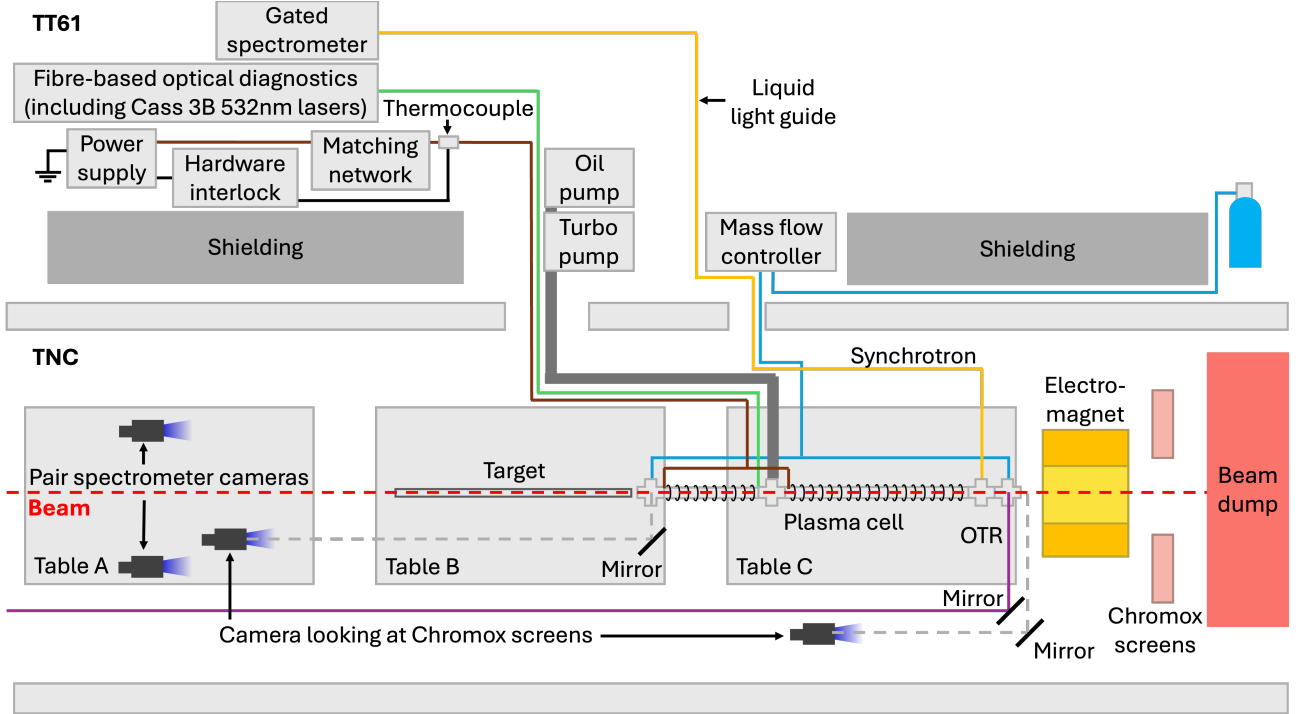


Figure 11: Overview of the experimental layout in TNC and TT61.

luminescent screen will be placed inside the plasma cell, at the centre of the first crosspiece. The downstream screen will be mounted outside the plasma cell, on a fixture attached to the cell itself.

Downstream of the plasma cell, an electromagnet will divert the electrons and positrons onto a pair of luminescent screens either side of the beam path, allowing the pair beam spectrum to be retrieved.

3.3 Target envelope implementation

The graphite target will be 1.4 m long, with 20 mm diameter. The target will be press-fit inside an aluminium envelope which provides a heat sink for the target. The graphite is capped on either side by graphite spacers which allow for the thermal expansion of the target. The target which will be hermetically sealed by 0.1 mm glassy carbon windows clamped by aluminium flanges with Vitron O-rigs to prevent the escape of radioactive carbon dust. The target window material and thickness have been chosen to minimise Coulomb scattering of the pair beam, and hence the pair beam divergence. The target envelop design and CAD drawing are shown in figure 13.

3.4 Plasma discharge

The plasma cell, shown in figure 14, will be 3 m long, with 63.5 mm diameter. A roughing pump and turbo pump, installed in TT61 and connected to the cell by bellows, evacuate the cell to 1×10^{-3} mbar. The cell is filled with Ar gas at $1 - 4 \times 10^{-2}$ mbar by gas feedthroughs at either end of the cell connected to a gas bottle in TT61. The flow rate can be controlled remotely using a mass flow controller installed in TT61.

While astrophysical plasmas primarily consist of Hydrogen and Helium, the plasma instabilities of interest in this experiment are driven by electron motion. For the timescales over which these instabilities develop, the plasma ions are assumed to be immobile, thus the choice of ion species does not affect the physical processes of interest.

The plasma is generated using three inductive coils, each of length 1 m, connected in parallel. The circuit is powered by a 6 kW radio frequency remotely-controllable power supply, Paramount HF 6013 Generator, which operates at 13.56 MHz. A Navigator II digital matching network will be used to maximise transmission from the power supply to the inductive circuit coupled to the plasma. Typically, the reflected power is $\leq 2\%$. The power supply contains a safety feature which cuts the power supply if the reflected power exceeds 0.3 kW. The matching network and power supply are connected to the cell by a coaxial cable which also provides the path to ground. Thus, the plasma vessel and coils are all at floating grounds.

The plasma discharge initiates capacitatively at low power (40 W). Inductive ionisation becomes dominant at 0.1 kW. The inductive coils produce time-varying axial magnetic fields which induce azimuthal electric fields which drive the plasma electrons. The plasma extends through the full 3 m of the cell, although the plasma

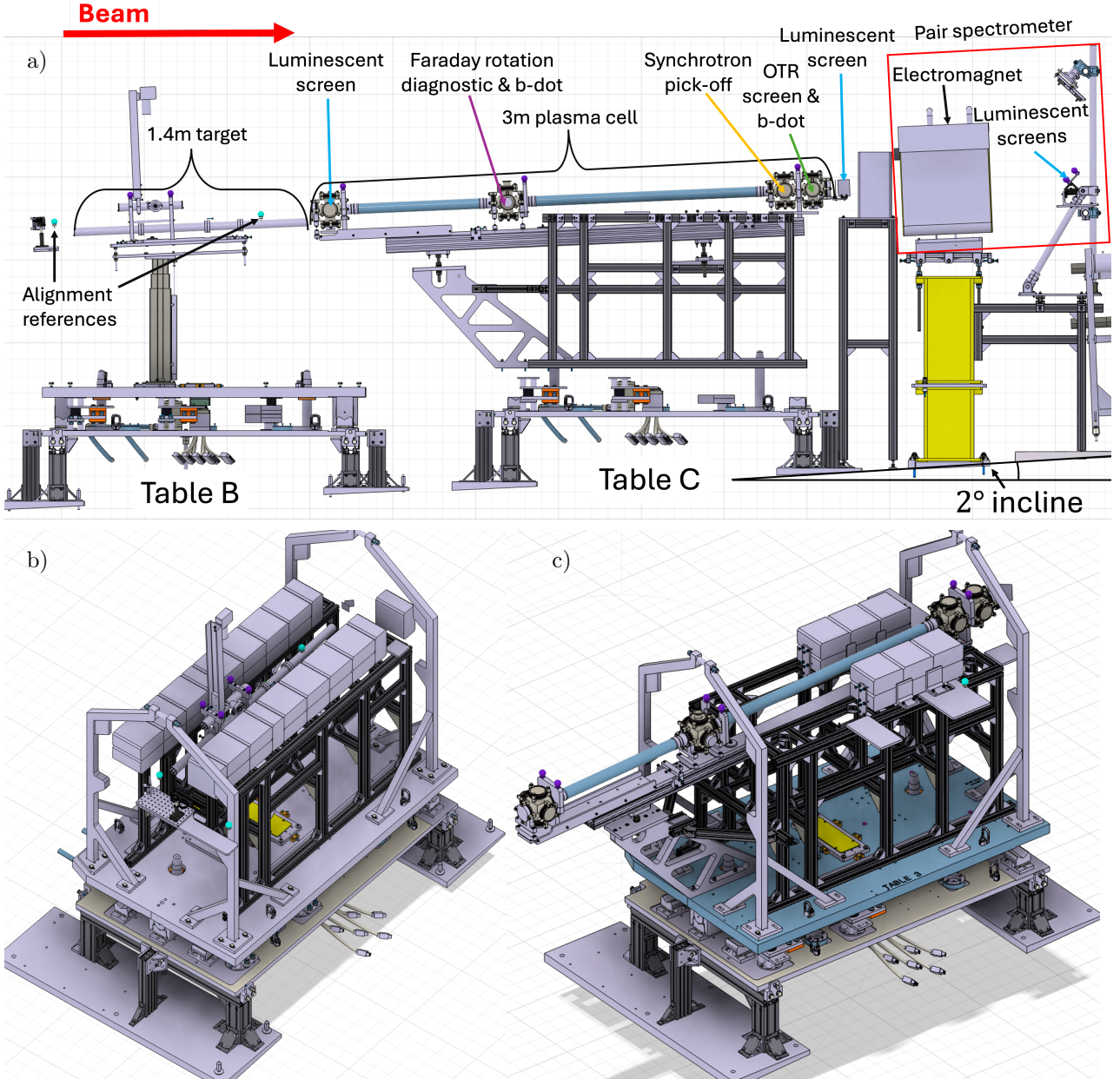


Figure 12: a) CAD design of the Fireball 3 experimental setup on tables B and C in the HiRadMat experimental area, including turquoise alignment references used to align optical diagnostics to the beam axis. b) Detailed overview of table B including the concrete shielding blocks surrounding the target, and purple references used to align experimental components (e.g. the target) with respect to the beam axis. c) Detailed overview of table C.

density is lower in the cross pieces where the discharge cannot be driven directly and is instead sustained by a hot electron population produced in the driven plasma. The gas lines, bellows for vacuum pumps, Faraday rotation diagnostic, upstream Chromox screen, OTR screen and synchrotron pick-off are mounted on the port crosses.

The plasma density is characterised in advance of the experiment using a Langmuir probe, and confirmed on a shot-to-shot basis using optical emission spectroscopy. On past experiments, plasma densities ranging between $10^{11} - 2 \times 10^{12} \text{ cm}^{-3}$ were achieved

A Faraday cage consisting of a copper mesh attached to a wooden frame encloses the plasma discharge to shield the RF fields.

3.5 Meteorite

3.5.1 HRMT-64 Results

The intensity of the primary proton beam used for each sample irradiation is shown in Figure 15, and examples of the laser doppler vibrometer (LDV) raw data, showing the radial surface displacement as a function of time,

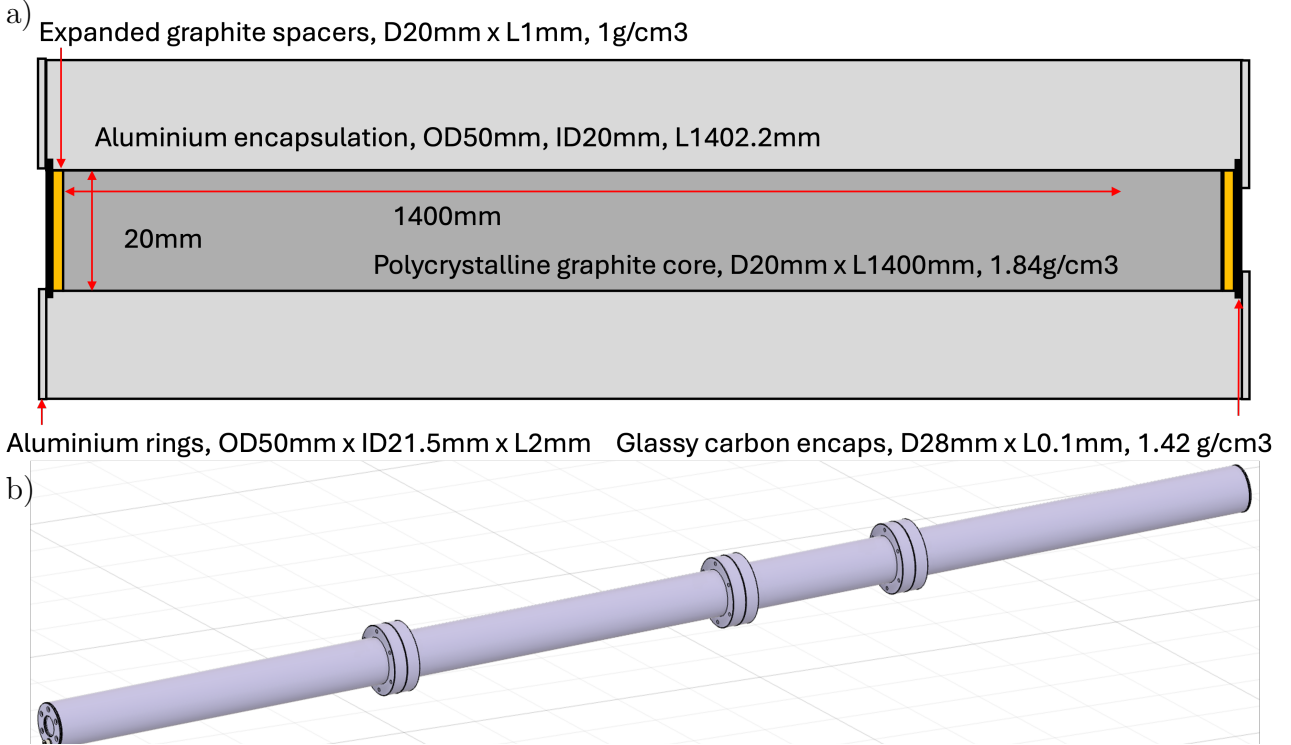


Figure 13: a) Diagram of the target and envelope. b) CAD drawing of the target envelope.

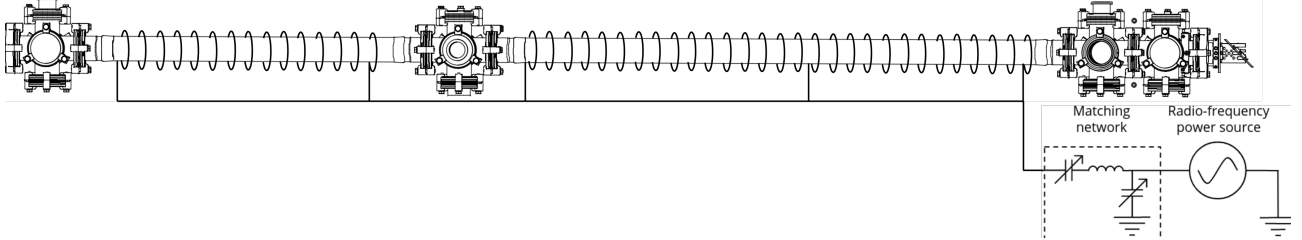


Figure 14: The Plasma cell design for Fireball 3.

are shown in Figure 16a). For the first 10 shots onto the sample, the primary beam intensity was 1×10^{11} protons, and damped oscillatory behavior was observed in the radial displacement of the sample surface. When the primary beam intensity was increased to 3×10^{11} protons, non-oscillatory behavior was suddenly observed. This behavior persisted even when the beam intensity was reduced to 1×10^{11} protons for 3 shots. Eventually, oscillatory behavior returned. Figure 16b) shows the Fourier Transform (FFT) spectrum of the LDV displacement data in the first and final shots showing oscillatory behavior. The similarity of the spectra confirms that the meteorite sample did not experience a catastrophic failure, but instead the collapse of oscillations indicates energy expended into plastic deformations of the meteorite sample, embodied in an increasing density of dislocations in the dominating Kamacite phase [43].

There are two critical differences between our results and previous results on the strain hardening of Kamacite: First, we have shown that the strain hardening occurs on the very short timescales of proton beam deposition, which means we have clarified that parameters like yield strength have to be treated as dynamical variables under high-energy deposition. This dynamical behavior can be experimentally controlled since the LDV data gives a real-time measurement of the oscillatory reaction of the surface material. Secondly, the sample returned to a very clear oscillatory behavior at high intensity.

Furthermore, it is suggested that with irradiation of an asteroid by a high energy, highly penetrating particle beam, it may be possible to deposit much higher amounts of energy into iron meteorite material without destruction than one would naively assume from the materials properties measured before high-energy irradiation.

3.5.2 HRMT-68 meteorite target and other changes compared to previous experimental run

The goal of the meteorite experiment as part of the HRMT-68 campaign is to extend the level of stress in the target beyond 13 GPa. At this pressure a phase transition to a hexagonal lattice structure is expected for the

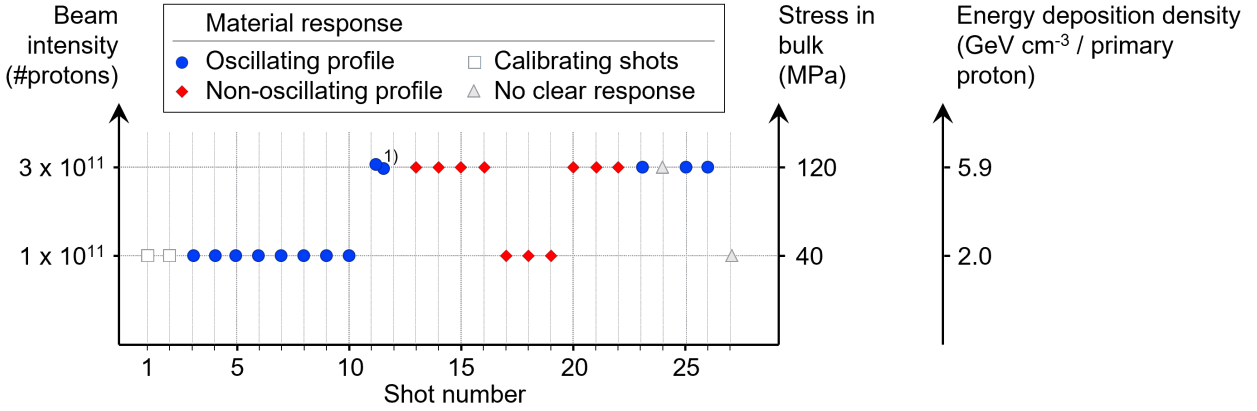


Figure 15: Material response based on displacement graph profiles per proton beam shot, distinguished by beam intensity (in number of protons), stress in bulk (in MPa), and energy deposition density (in GeV cm^{-3} per primary proton). 1) cumulated measurement data of two shots, no separate data available for individual shots 11 and 12

Fe-Ni alloys of the meteorite, similar to the martensitic phase transition of steel. In the HRMT-64 setting, the pressure was low enough to avoid phase transitions. This allowed us to study the effects of high intensity high energy deposition and high strain rate without any change in the crystal structure, leading to the results described above.

The natural next step is therefore to extend this to a stress regime which includes a phase transition. Again, the pressure level is chosen to include the first phase transition but to avoid the complications of phase transitions at still higher pressure where the resulting crystal structures are complex and not well studied ([49], [50], [51], [52], [53]). On the other hand, the phase transition at 13 GPa has a crystal structure which is well known from the study of meteorites which have experienced high stress levels ([37]).

While the dimensions of the meteorite sample (a cylinder of 5 mm radius and 100 mm length) and the conical support structure will remain unchanged compared to the previous experiment, we will use a different specimen for the meteorite. The choice of Campo del Cielo for HRMT-64 was determined by the medium size of the blocks of the two different crystal structures of Kamacite and Taenite. This ensured that even in the unlikely case that reflections of the elastic wave at these blocks would have occurred, the resulting frequency shift would still have led to a spectrum within the range of the LDV. Since it is now known from the previous experiment that this does definitely not occur, the sample is planned to be chosen from the Swedish Muonionalusta fall ([42]). Some slices of this meteorite reach very high levels of yield strength already (see Figure 17) which are expected to be the result of shock impacts. This should not only increase the probability of realizing the phase transition in HRMT-68, but also secure the sample against catastrophic failure.

4 Diagnostics

4.1 Luminescent screens

The transverse profile of the pair and proton beams will be characterised using Chromox luminescent screens mounted in the upstream plasma cell cross-piece, and external to the cell, attached to the downstream cross-piece.

The luminescent screens will be imaged by digital CMOS cameras placed in TNC, transverse to the beam axis such that the high-energy hadron equivalent dose, $\text{HEEq} < 0.8 \times 10^{17}$, at which the cameras fail on 50% of shots.

Figure 18a) depicts the downstream Chromox screen and Al blocker foil, which minimises its exposure to ambient optical light. In figure 18b), good agreement is seen between the simulated (using FLUKA) and measured Chromox screen response to the proton beam (measured with the target driven out) and its response to the pair beam (with hadron components) generated using a 0.36 m carbon, 10 mm Ta target; this was used for the Fireball 2 experiment). It is assumed that the scintillation brightness is directly proportional to the energy deposited in the screen.

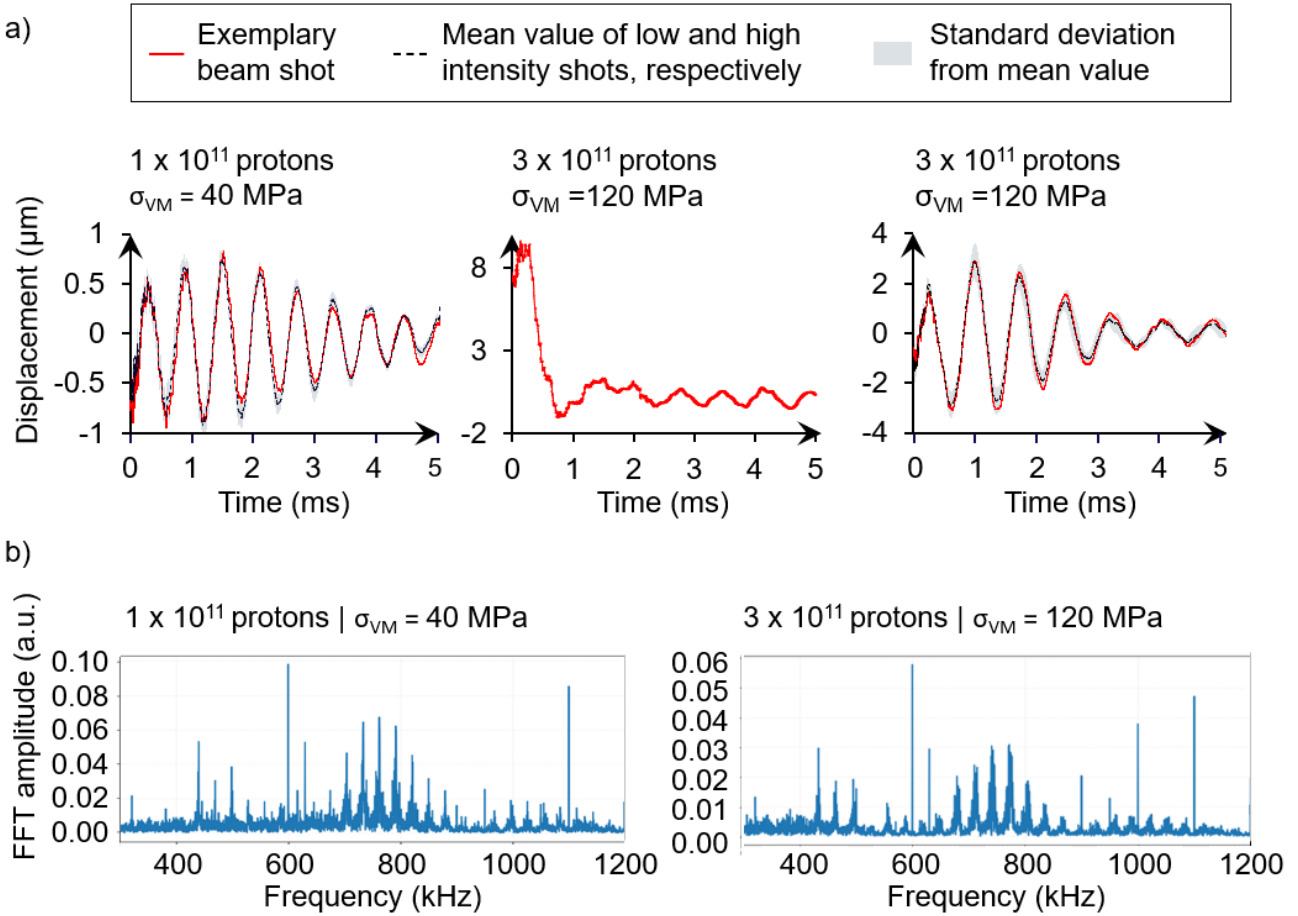


Figure 16: LDV displacement data and FFT spectrum a) Radial meteorite surface displacement in μm over time in ms, gathered by LDV. Left) the oscillatory profile for example beam shot 4 (red line), the mean value (black dashed line) and, standard deviation of beam shots 3, 4, 5, 6, 7, 8, 9 and 10; middle) the non-oscillatory displacement profile for example beam shot 21, i.e. "plastic" profile; right) the recurrence to oscillatory displacement profile for example beam shot 23 (red line), the mean value (black dashed line) and standard deviation for beam shots 11/12 (cumulative), 23, 25, and 26, b) Fast Fourier Transform (FFT) spectrum of the meteorite sample oscillations: left) example beam shot 4, low intensity at 1×10^{11} protons and right) example beam shot 23, high intensity at 3×10^{11} protons

4.2 Magnetic field diagnostics

4.2.1 Faraday rotation

Figure 19 provides an overview of the experimental setup for the Faraday rotation diagnostic. A magnetised plasma becomes birefringent, as the charge and mass difference of the plasma electrons and ions results in asymmetries between the left- and right-handed cyclotron motion of the plasma. A linearly polarised laser incident on the plasma is split into orthogonally polarised left and right polarised components which experience different indices of refraction. As a result of this, the total linear polarisation, derived from the sum of these components, rotates as a function of propagation distance through the plasma. The angle of rotation, $\Delta\theta$, is given by the path integrated magnetic field;

$$\Delta\theta = V \int B(l) dl \quad (2)$$

where V is the Verdet constant of the medium through which the laser propagates. The plasma has a small Verdet constant. To increase the angle of rotation and thus the sensitivity of the diagnostic, a terbium gallium garnet crystal (TGG) is inserted into the plasma. This has a high Verdet constant of 230 rad T m at room temperature for a probe laser of wavelength 532 nm , which will be used in the experiment.

The TGG crystal was encased in a ceramic sheath to insulate it from the plasma, and was placed 5 mm away from the beam axis to prevent irradiation by the proton beam.

While the magnetic fields of the electron and positron filaments are expected to cancel when averaged over the whole beam, the magnetic fields over lengths scales $\geq \lambda_s \approx 3 \text{ mm}$, where the skin depth, λ_s is the length-scale of a filament, do not cancel. The length of the TTG crystal, 10 mm, and degree of insertion into the pair

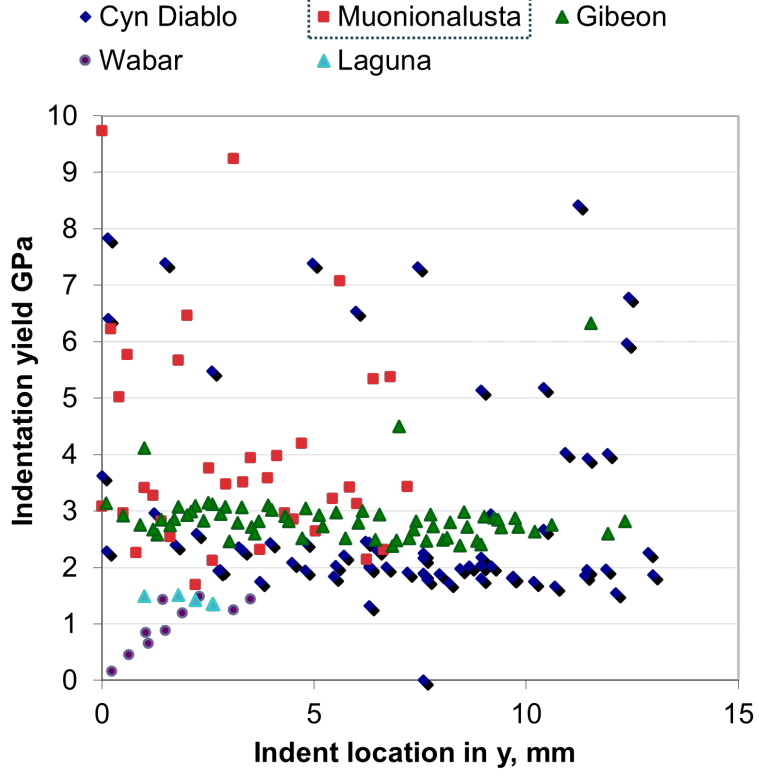


Figure 17: Yield Strength of different meteorite species. Measurements performed on different meteorite species [42]

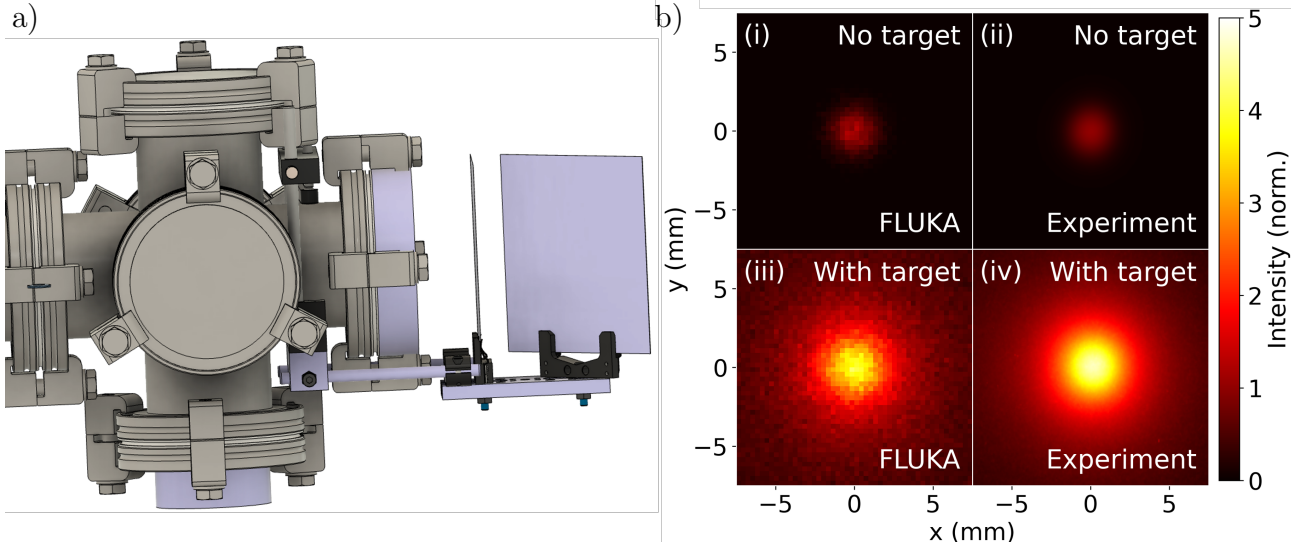


Figure 18: a) CAD design of downstream luminescent Chomox profile screen, mounted on the final cross-piece of the plasma cell, at 45° to the beam axis. A thin Al blocking foil is mounted in front of the luminescent screen. b) FLUKA simulations and experimental measurements of the luminescent screen response to the proton beam (upper) and pair beam (lower).

beam is carefully chosen to ensure the magnetic fields do not cancel over the laser path. The Faraday rotation diagnostic employed during the Fireball 2 experiment measured 2-3 mT magnetic fields for a 0.87 m plasma, as illustrated in figure 20. We will employ a similar diagnostic for Fireball 3 to measure the magnetic fields generated in a 3 m plasma.

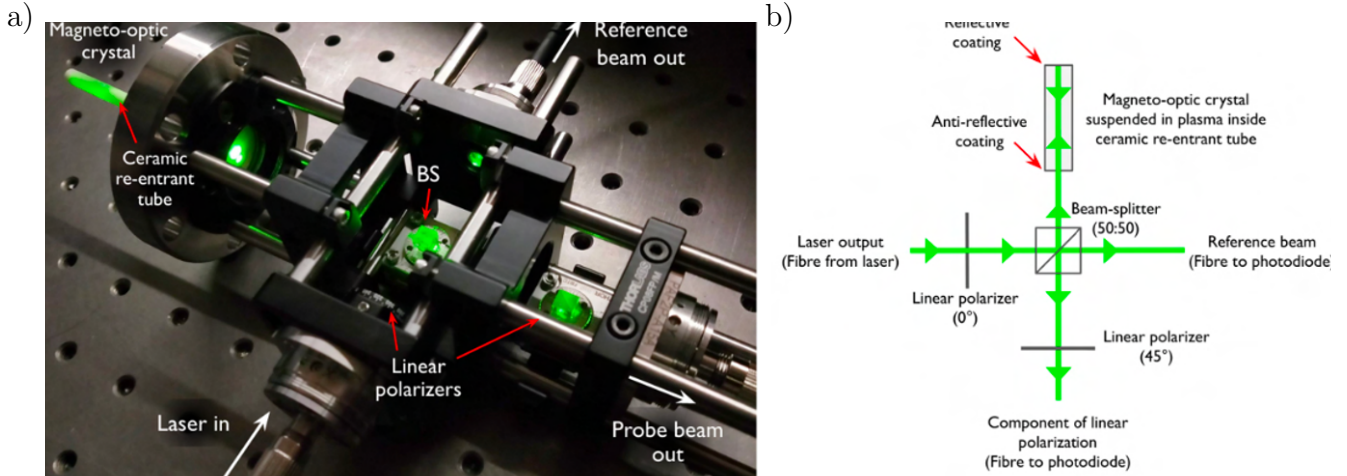


Figure 19: a) Photograph of the Faraday rotation diagnostic. b) Diagram depicting the beam components and laser path for the Faraday rotation diagnostic.

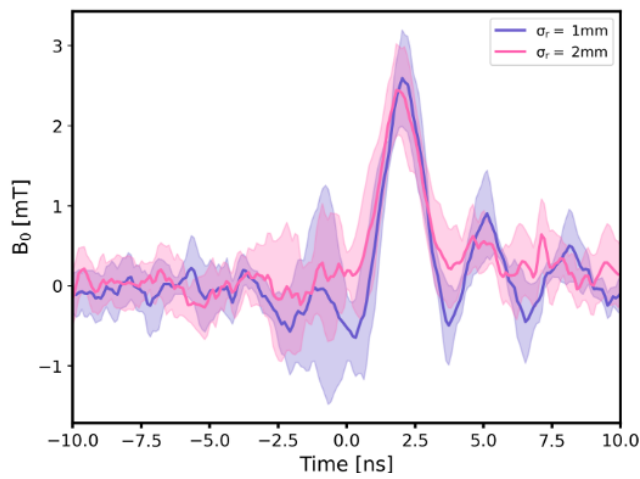


Figure 20: Magnetic field measurement using the Faraday rotation diagnostic employed for Fireball 2.

4.2.2 B-dot probes

B-dot probes will be mounted in two of the plasma cell crosspieces, 1 m and 3 m downstream of the upstream window of the plasma cell. The b-dot probes we plan to field consist of a single loop of 2 mm diameter wire, as illustrated in figure 21. A time-varying magnetic field induces a potential difference, V_{ind} across the coil, in accordance with Faraday's law of induction:

$$V_{ind} \propto \frac{d\Phi}{dt} = N \frac{d \int \vec{B} \cdot d\vec{A}}{dt} \quad (3)$$

where Φ is the magnetic flux, \vec{B} denotes the magnetic field and the integral is over the cross-sectional area of the coil. Figure 21b) summarises the electrical circuit to be used in HRMT-68 which will be used to measure the induced voltage.

In figure 21c), the time-varying magnetic fields predicted by the PIC code, OSIRIS, after 3 m of plasma are shown alongside the response of the b-dot probe, modelled using the electronic circuit simulator code, SPICE. The b-dot probe measured a corresponding voltage of 40 V, as shown in figure 21d).

4.3 Pair spectrometer

The pair spectrometer will measure the number and energy spectra of electron-positron pairs generated by the target-converter setup, to confirm the electron-positron beam characteristics indicated by our FLUKA simulations. The pair spectrometer will also measure the difference in divergence between electrons and positrons (latter should be more divergent) due to the development of plasma instabilities.

Since the bulk of the electrons and positrons in the beam have much smaller momenta than the hadrons (most of the pairs have momenta $\ll 1$ GeV), dipole magnets can be used to deflect them out of the beam to

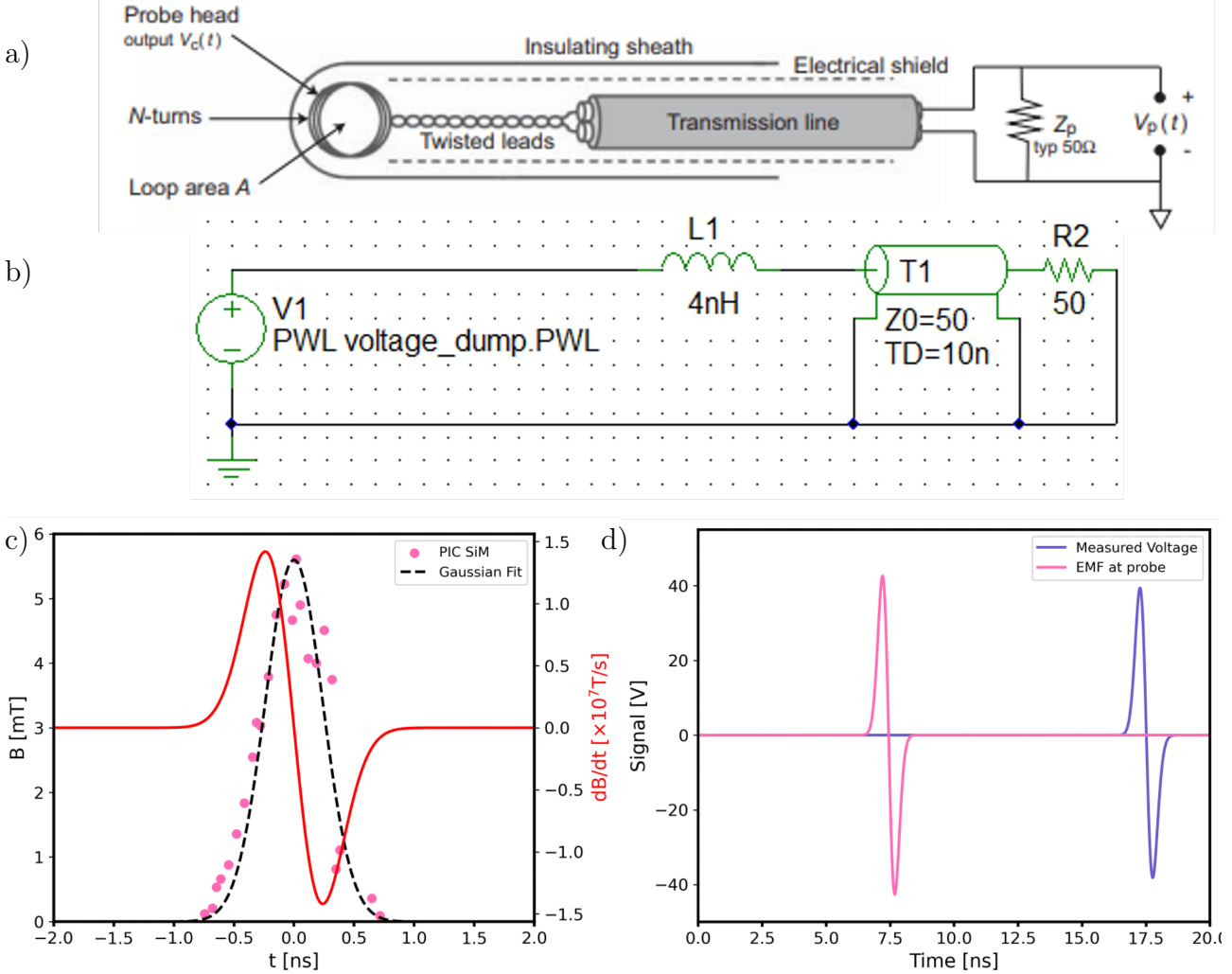


Figure 21: a) Overview of a b-dot probe. b) Circuit drawing for the b-dot probes to be used for HRMT-68. c) Particle-in-cell simulation results for the time-varying magnetic field generated by the pair beam after propagating through the 3 m of plasma cell, and the corresponding Gaussian fit, shown alongside the magnetic field driven in the b-dot probe. d) Voltage signal induced in the b-dot probe by the time-varying magnetic fields shown in c).

study their energy distribution, while the hadrons are deflected less and are absorbed mostly by the beam dump. The use of an MNPA-type dipole (used in HRMT-62 and HRMT-64) is proposed also for this experiment. The installation procedure of this magnet in TNC tunnel is known and was followed successfully in the previous experiment [54]. This magnet is relatively short in length relative to the breadth of its magnet gap, compared with other electromagnets in the Magnets Kit. This means the charged particles can be deflected by large angles to far off-axis, away from the peak fluence of gamma rays and other particle species. The advantages of using an MNPA electromagnet instead of a smaller permanent magnet setup are that the MNPA has a larger bending power, allowing 100s of MeV/c electrons and positrons to be deflected; the magnet gap is very large, so more of the beam can be collected; the large iron yoke of the magnet acts to shield the line of sight from the converter and plasma cell, reducing the background in the deflected region; and the field strength within the magnet gap can be controlled so that the range of the energies that are sampled by detectors can be easily modified. The energy spectrum of electrons and positrons is measured by using the MNPA-type dipole to deflect pairs from the beam axis onto Chromox luminescence screens (see Figure 22). The internal magnetic field of the electromagnet is varied over multiple shots to capture different energy ranges of pairs on the screens. When the electromagnet is turned on, an excess of signal is observed > 200 mm off-axis that can only be explained by the presence of positrons. Data obtained when the magnet is turned off provides a lower bound of the measured spectrum. The full spectrum of electrons (blue) and positrons (red) is constructed by piecing together spectra obtained at different magnet settings. An absolute calibration is obtained by fitting image intensities to images of the screens irradiated by a known flux of protons. The errors associated with the absolute calibration are represented by the shaded regions, and histograms show the comparison with the energy spectra of pairs simulated by FLUKA. We conclude that the studies so far demonstrate the viability for our main diagnostics with the experimental

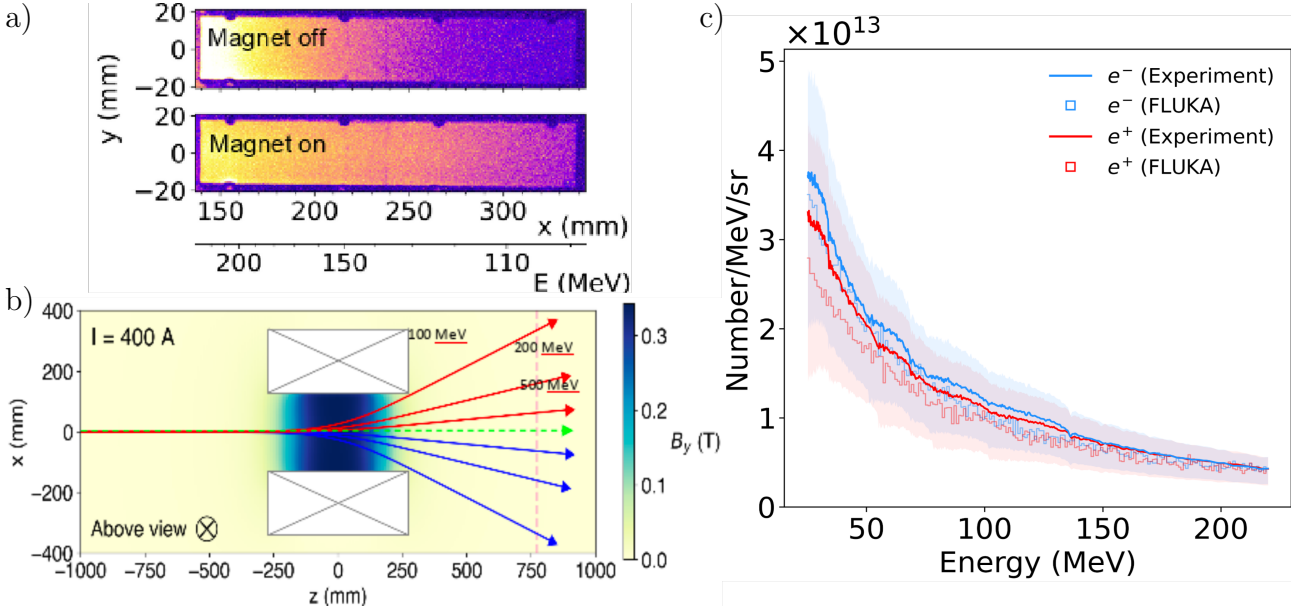


Figure 22: a) Raw image data of the luminescence screen onto which positrons are deflected. b) Electromagnet setup and imaging lines for the luminescence screens. c) Experimental results from HRMT-62 compared to FLUKA predictions.

configuration in its currently proposed form.

4.4 Optical transition radiation

A thin (0.5 mm) copper foil will be placed in the beam path. As the pair beam passes through the foil, it induces an oscillating dipole in the foil which emits broadband optical transition radiation (OTR), which peaks in the visible spectrum. The backward OTR will be transported to the streak camera using an optical imaging line, shown in figure 23a). The imaging line will have $\approx 24\%$ transmission efficiency if an anti-reflection (AR) coating with 99.75% transmission is used, which is the industry norm.

The streak camera consists of a ORCA-Flash4.0 V2 camera mounted on a C7700 Hamamatsu streak unit. The streak unit has 5 ps resolution for an 11 ns sweep time (temporal acquisition window of the streak unit). The optics introduce an additional dispersion of 3.2 ps, thus the OTR diagnostic has ≈ 8 ps resolution, which is sufficient to resolve density modulations in the pair beam on the order of the skin depth, which is 10 ps for a plasma density of $2 \times 10^{12} \text{ cm}^{-3}$.

The layout of the imaging line for the OTR emission in TNC and TJ7 is shown in figure 23. The first two lenses will be mounted on optical breadboards attached to table C, while the remaining optics will be set up on free-standing tripods or optical benches. The streak camera will be mounted inside the concrete bunker in TJ7, which will provide additional shielding from secondaries produced by the beam. The streak camera requires an early trigger with < 1 ns jitter, which will be provided by a beam line monitor mounted above the beamline in TJ7, 13 m away from the camera. FLUKA simulations have been used to confirm the signal will be sufficient to trigger the Stanford box used to trigger the streak camera.

4.5 Synchrotron radiation

A thin pellicle with a reflective coating will be used to pick-off the synchrotron emission, which simulations (see figure 9) indicate will peak near visible wavelengths. The synchrotron emission will be focussed into a 15 m liquid light guide, chosen for its high efficiency of light transport over ~ 10 m distances. A motorised filter wheel placed between the pellicle and the first focussing optic will contain right- and left- handed polarising filters, allowing the polarisation of the optical emission to be studied. The light guide will transport the signal to a gated spectrometer (Andor iStar DH734-18U-03, mounted on an Aryelle 200 spectrometer), installed in TT61.

The Andor iStar has a minimum exposure time of 2 ns, over which time the intensity of synchrotron emission should exceed that of the optical plasma emission, as indicated in figure 9. The gated spectrometer will be triggered using a signal from a beam line monitor placed at the downstream end of table A. An overview of the experimental setup for the synchrotron diagnostic is provided in figure 24.

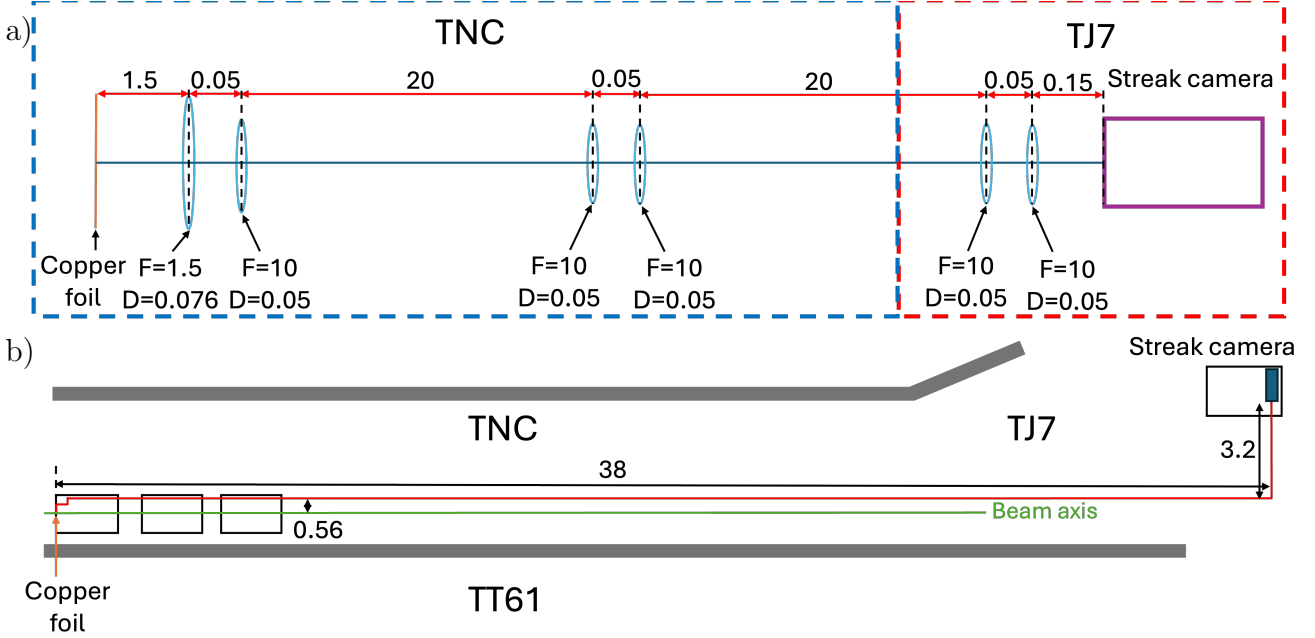


Figure 23: a) Imaging line used to transport the OTR signal, generated in the furthest downstream plasma cell cross-piece, to the streak camera, positioned in a concrete bunker in TJ7.

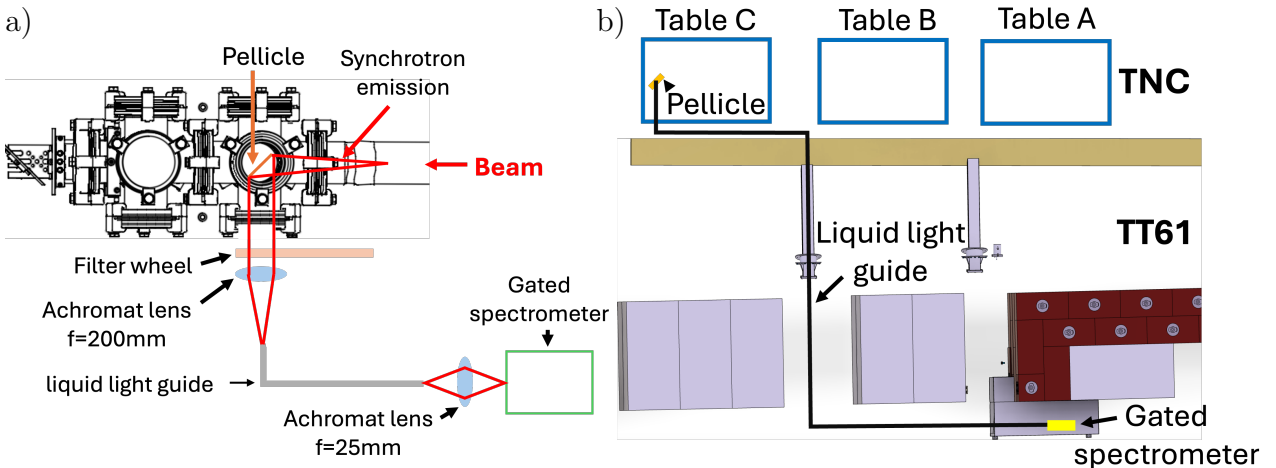


Figure 24: a) The layout of the optical components used to transport and image the synchrotron emission. b) The relative positions of the synchrotron pellicle, liquid light guide path and the gated spectrometer

4.6 Diagnostics for meteorite target

A laser doppler vibrometer (LDV) with $\lambda = 1550$ nm mounted directly above the meteorite target will be used to measure the oscillations induced in the meteorite target by the proton beam. The LDV compares a laser beam which is scattered from the target to a reference beam. The doppler-shift induced in the scattered laser light by the oscillatory target motion is used to extract the amplitude and frequency of the target oscillations.

The crystalline structure of the meteorite target will be probed following the completion of the experiment using the neutron beam at the ISIS facility at Rutherford Appleton Laboratories.

5 Pulse list

During HRMT-64, beam intensities up to 3.2×10^{11} were achieved for a single proton bunch with 4σ bunch length of 1 ns. The majority of extracted bunches had intensity 3×10^{11} . Over the course of the fireball campaign, a total of 4×10^{13} protons were extracted. This corresponds to a very low irradiation level. Several focussing configurations were employed to vary the 1σ proton beam size at focus from 1 – 3 mm. All of the experimental objectives were accomplished within 4 days.

For the HRMT-68 campaign, we propose a similar integrated proton intensities. For the fireball experiment,

we will primarily use proton beams with 3×10^{11} intensity, 3 mm 1σ transverse size and 1 ns duration. Some shots will use beam intensities of 5×10^{11} . For the meteorite campaign, we will use proton beams with intensities up to 5×10^{11} , 0.1 mm 1σ transverse size and a 4σ bunch length of 1 ns. Overall, we expect the same total number of proton irradiation as in the previous campaigns.

References

- [1] Peter Goldreich and William H. Julian. Pulsar Electrodynamics. , 157:869, August 1969.
- [2] Jonathan Arons. Pair creation above pulsar polar caps-geometrical structure and energetics of slot gaps. *Astrophysical Journal, Part 1, vol. 266, Mar. 1, 1983, p. 215-241. Research supported by the Commissariat a l'Energy Atomique and John Simon Guggenheim Foundation*, 266:215–241, 1983.
- [3] R. D. Blandford and R. L. Znajek. Electromagnetic extraction of energy from kerr black holes. *Monthly Notices of the Royal Astronomical Society*, 179(3):433–456, 07 1977.
- [4] Mitchell C. Begelman, Roger D. Blandford, and Martin J. Rees. Theory of extragalactic radio sources. *Rev. Mod. Phys.*, 56:255–351, Apr 1984.
- [5] H. Richard Miller and Paul J. Wiita. *Active Galactic Nuclei*, volume 30. 1988.
- [6] J. F. C. Wardle, D. C. Homan, R. Ojha, and D. H. Roberts. Electron–positron jets associated with the quasar 3c279. *Nature*, 395(6701):457–461, 1998.
- [7] P. Meszaros and M. J. Rees. Relativistic Fireballs and Their Impact on External Matter: Models for Cosmological Gamma-Ray Bursts. , 405:278, March 1993.
- [8] Tsvi Piran. The physics of gamma-ray bursts. *Rev. Mod. Phys.*, 76:1143–1210, Jan 2005.
- [9] Andrei Gruzinov. Gamma-ray burst phenomenology, shock dynamo, and the first magnetic fields. *The Astrophysical Journal*, 563(1):L15, nov 2001.
- [10] Philip Chang, Anatoly Spitkovsky, and Jonathan Arons. Long-term evolution of magnetic turbulence in relativistic collisionless shocks: Electron-positron plasmas. *The Astrophysical Journal*, 674(1):378, feb 2008.
- [11] S. A. Bludman, K. M. Watson, and M. N. Rosenbluth. Statistical mechanics of relativistic streams. ii. *The Physics of Fluids*, 3(5):747–757, 09 1960.
- [12] Roswell Lee and Martin Lampe. Electromagnetic instabilities, filamentation, and focusing of relativistic electron beams. *Phys. Rev. Lett.*, 31:1390–1393, Dec 1973.
- [13] B. B. Godfrey, W. R. Shanahan, and L. E. Thode. Linear theory of a cold relativistic beam propagating along an external magnetic field. *Physics of Fluids*, 18(3):346–355, March 1975.
- [14] Mikhail V. Medvedev and Abraham Loeb. Generation of magnetic fields in the relativistic shock of gamma-ray burst sources. *The Astrophysical Journal*, 526(2):697, dec 1999.
- [15] A. Bret. Weibel, two-stream, filamentation, oblique, bell, buneman...which one grows faster? *The Astrophysical Journal*, 699(2):990, 2009.
- [16] Jun-Ichi Sakai, Reinhard Schlickeiser, and P. K. Shukla. Simulation studies of the magnetic field generation in cosmological plasmas. *Physics Letters A*, 330(5):384–389, September 2004.
- [17] Mikhail V. Medvedev and Anatoly Spitkovsky. Radiative cooling in relativistic collisionless shocks: Can simulations and experiments probe relevant gamma-ray burst physics? *The Astrophysical Journal*, 700(2):956, jul 2009.
- [18] C. D. Arrowsmith, N. Shukla, N. Charitonidis, R. Boni, H. Chen, T. Davenne, A. Dyson, D. H. Froula, J. T. Gudmundsson, B. T. Huffman, Y. Kadi, B. Reville, S. Richardson, S. Sarkar, J. L. Shaw, L. O. Silva, P. Simon, R. M. G. M. Trines, R. Bingham, and G. Gregori. Generating ultradense pair beams using 400 GeV/c protons. *Phys. Rev. Res.*, 3:023103, May 2021.
- [19] I Efthymiopoulos, C Hessler, H Gaillard, D Grenier, M Meddahi, P Trilhe, A Pardons, C Theis, N Charitonidis, S Evrard, H Vincke, and M Lazzaroni. HiRadMat: A New Irradiation Facility for Material Testing at CERN. 2011.

- [20] G. Sarri, K. Poder, J. M. Cole, W. Schumaker, A. Di Piazza, B. Reville, T. Dzelzainis, D. Doria, L. A. Gizzi, G. Grittani, S. Kar, C. H. Keitel, K. Krushelnick, S. Kuschel, S. P. D. Mangles, Z. Najmudin, N. Shukla, L. O. Silva, D. Symes, A. G. R. Thomas, M. Vargas, J. Vieira, and M. Zepf. Generation of neutral and high-density electron–positron pair plasmas in the laboratory. *Nature Communications*, 6(1):6747, 2015.
- [21] G. J. Williams, B. B. Pollock, F. Albert, J. Park, and Hui Chen. Positron generation using laser-wakefield electron sources. *Physics of Plasmas*, 22(9):093115, 09 2015.
- [22] Tongjun Xu, Baifei Shen, Jiancai Xu, Shun Li, Yong Yu, Jinfeng Li, Xiaoming Lu, Cheng Wang, Xinliang Wang, Xiaoyan Liang, Yuxin Leng, Ruxin Li, and Zhizhan Xu. Ultrashort megaelectronvolt positron beam generation based on laser-accelerated electrons. *Physics of Plasmas*, 23(3):033109, 03 2016.
- [23] J. Warwick, T. Dzelzainis, M. E. Dieckmann, W. Schumaker, D. Doria, L. Romagnani, K. Poder, J. M. Cole, A. Alejo, M. Yeung, K. Krushelnick, S. P. D. Mangles, Z. Najmudin, B. Reville, G. M. Samarin, D. D. Symes, A. G. R. Thomas, M. Borghesi, and G. Sarri. Experimental observation of a current-driven instability in a neutral electron-positron beam. *Phys. Rev. Lett.*, 119:185002, Nov 2017.
- [24] G. J. Williams, Hui Chen, J. Kim, S. Kerr, and H. Y. Khater. Comment on “table-top laser-based source of femtosecond, collimated, ultrarelativistic positron beams”. *Phys. Rev. Lett.*, 124:179501, May 2020.
- [25] Orson L Anderson. Properties of iron at the earth’s core conditions. *Geophysical Journal International*, 84(3):561–579, 1986.
- [26] Yimei Fang, Yang Sun, Renhai Wang, Feng Zheng, Feng Zhang, Shunqing Wu, Cai-Zhuang Wang, Renata M Wentzcovitch, and Kai-Ming Ho. Structural prediction of fe-mg-o compounds at super-earth’s pressures. *Physical Review Materials*, 7(11):113602, 2023.
- [27] M Harmand. Phase diagrams of iron and iron oxides at super-earth interior conditions. In *LMJ User Meeting, Bordeaux, France*, 2023.
- [28] Peter Lord, Scott Tilley, David Y Oh, Dan Goebel, Carol Polanskey, Steve Snyder, Greg Carr, Steven M Collins, Gregory Lantoine, Damon Landau, et al. Psyche: Journey to a metal world. In *2017 IEEE Aerospace Conference*, pages 1–11. IEEE, 2017.
- [29] General Atomic. Nuclear pulse space vehicle study: Vol. i summary. Technical report, Technical report, performed under NASA Contract NAS 8-11053, George C . . . , 1954.
- [30] George Dyson. Project orion: the atomic spaceship, 1957-1965. (*No Title*), 2002.
- [31] Diqing Wan. Strain amplitude dependent damping of high damping high strength magnesium matrix composites. Available at SSRN 4154949.
- [32] Komal Chawla and Samit Ray-Chaudhuri. Amplitude dependent damping behaviour of fundamental mode for cfrp composite tubes: Effect of cross-section. *Journal of Sound and Vibration*, 476:115313, 2020.
- [33] Hui Li, Yi Niu, Zelin Li, Zhonghao Xu, and Qingkai Han. Modeling of amplitude-dependent damping characteristics of fiber reinforced composite thin plate. *Applied Mathematical Modelling*, 80:394–407, 2020.
- [34] A Wolfenden, DM Mc Daniels, and RU Vaidya. Temperature dependence of dynamic young’s modulus and mechanical damping in scs-6/beta-21s titanium metal matrix composites. *Journal of materials science letters*, 19(7):595–599, 2000.
- [35] Angela M Stickle, Megan Bruck Syal, Andy F Cheng, Gareth S Collins, Thomas M Davison, Galen Gisler, Nicole Güldemeister, Tamra Heberling, Robert Luther, Patrick Michel, et al. Benchmarking impact hydromechanics in the strength regime: Implications for modeling deflection by a kinetic impactor. *Icarus*, 338:113446, 2020.
- [36] Leos Pohl and Daniel T Britt. Strengths of meteorites—an overview and analysis of available data. *Meteoritics & Planetary Science*, 55(4):962–987, 2020.
- [37] Anant V Jain, Robert B Gordon, and Michael E Lipschutz. Hardness of kamacite and shock histories of 119 meteorites. *Journal of Geophysical Research*, 77(35):6940–6954, 1972.
- [38] Amir Siraj and Abraham Loeb. Interstellar meteors are outliers in material strength. *The Astrophysical Journal Letters*, 941(2):L28, 2022.
- [39] AR Miles. Asteroid deflection via standoff nuclear explosions. In *Asteroid Deflection Research Symposium, Arlington, VA*, 2008.

- [40] Nathan W Moore, Mikhail Mesh, Jason J Sanchez, Marc-Andre Schaeuble, Chad A McCoy, Carlos R Aragon, Kyle R Cochrane, Michael J Powell, and Seth Root. Simulation of asteroid deflection with a megajoule-class x-ray pulse. *Nature Physics*, pages 1–7, 2024.
- [41] I. Efthymiopoulos, C. Hessler, H. Gaillard, D. Grenier, M. Meddahi, P. Trilhe, A. Pardons, C. Theis, N. Charitonidis, S. Evrard, H. Vincke, and M. Lazzaroni. Hiradmat: A new irradiation facility for material testing at cern. In *Proceedings of the 2nd Int. Particle Accelerator Conf.*, volume IPAC2011, pages 1665–1667, 2011.
- [42] Roberta N Mulford and Bassem El-Dasher. Mechanical properties of several fe-ni meteorites. Technical report, Los Alamos National Laboratory (LANL), Los Alamos, NM (United States), 2010.
- [43] W Osuch, R Błoniarz, G Michta, and I Suliga. Evolution of the dislocation structure of iron meteorite. *Archives of Metallurgy and Materials*, 65(1):485–492, 2020.
- [44] Charles D Arrowsmith, N Shukla, Nikolaos Charitonidis, R Boni, H Chen, T Davenne, A Dyson, DH Froula, Jon Tomas Gudmundsson, BT Huffman, et al. Generating ultradense pair beams using 400 gev/c protons. *Physical Review Research*, 3(2):023103, 2021.
- [45] CD Arrowsmith, Pascal Simon, PJ Bilbao, AFA Bott, Stephane Burger, Hui Chen, FD Cruz, Tristan Davenne, Ilias Efthymiopoulos, DH Froula, et al. Laboratory realization of relativistic pair-plasma beams. *Nature Communications*, 15(1):5029, 2024.
- [46] Petr Šittner, Ludek Heller, Jan Pilch, Caroline Curfs, Thiery Alonso, and Denis Favier. Young’s modulus of austenite and martensite phases in superelastic niti wires. *Journal of materials engineering and performance*, 23:2303–2314, 2014.
- [47] R. A. Fonseca, L. O. Silva, F. S. Tsung, V. K. Decyk, W. Lu, C. Ren, W. B. Mori, S. Deng, S. Lee, T. Katsouleas, and J. C. Adam. Osiris: A three-dimensional, fully relativistic particle in cell code for modeling plasma based accelerators. In Peter M. A. Sloot, Alfons G. Hoekstra, C. J. Kenneth Tan, and Jack J. Dongarra, editors, *Computational Science — ICCS 2002*, pages 342–351, Berlin, Heidelberg, 2002. Springer Berlin Heidelberg.
- [48] T D Arber, K Bennett, C S Brady, A Lawrence-Douglas, M G Ramsay, N J Sircombe, P Gillies, R G Evans, H Schmitz, A R Bell, and C P Ridgers. Contemporary particle-in-cell approach to laser-plasma modelling. *Plasma Physics and Controlled Fusion*, 57(11):113001, 2015.
- [49] Simone Anzellini, Daniel Errandonea, Leonid Burakovskiy, John E Proctor, Robin Turnbull, and Christine M Beavers. Characterization of the high-pressure and high-temperature phase diagram and equation of state of chromium. *Scientific reports*, 12(1):6727, 2022.
- [50] Leonid Dubrovinsky, Saiana Khandarkhaeva, Timofey Fedotenko, Dominique Laniel, Maxim Bykov, Carlotta Giacobbe, Eleanor Lawrence Bright, Pavel Sedmak, Stella Chariton, Vitali Prakapenka, et al. Materials synthesis at terapascal static pressures. *Nature*, 605(7909):274–278, 2022.
- [51] Martin G Gorman, S Elatresh, Amy Lazicki, Marc ME Cormier, SA Bonev, D McGonegle, R Briggs, AL Coleman, SD Rothman, L Peacock, et al. Experimental observation of open structures in elemental magnesium at terapascal pressures. *Nature Physics*, 18(11):1307–1311, 2022.
- [52] NA Smirnov. Ab initio calculations of structural stability, thermodynamic and elastic properties of ni, pd, rh, and ir at high pressures. *Journal of Applied Physics*, 134(2), 2023.
- [53] Samuel R Baty, Leonid Burakovskiy, Darby J Luscher, Simone Anzellini, and D Errandonea. Palladium at high pressure and high temperature: A combined experimental and theoretical study. *Journal of Applied Physics*, 135(7), 2024.
- [54] P. Simon and F. Maria-Velotti. Hiradmat temporary modifications for the fireball experiment (hrm-c-ec-0001).

¹

Suppression of pair beam instabilities in a ² laboratory analogue of blazar pair cascades

³ C. D. Arrowsmith^{1*}, F. Miniati¹, P. J. Bilbao², P. Simon^{3,4}, A. F. A. Bott¹,
⁴ S. Burger³, H. Chen⁵, F. D. Cruz², T. Davenne⁶, A. Dyson¹, I. Efthymiopoulos³,
⁵ D. H. Froula⁷, A. Goillot³, J. T. Gudmundsson^{8,9}, D. Haberberger⁷,
⁶ J. W. D. Halliday¹, T. Hodge^{1,10}, B. T. Huffman¹, S. Iaquinta¹, G. Marshall¹⁰,
⁷ B. Reville¹¹, S. Sarkar¹, A. A. Schekochihin¹, L. O. Silva², R. Simpson⁵,
⁸ V. Stergiou^{1,3,12}, R. M. G. M. Trines⁶, T. Vieu¹¹, N. Charitonidis³, R. Bingham^{6,13},
⁹ G. Gregori¹

¹⁰ Department of Physics, University of Oxford, Parks Road, Oxford, OX1 3PU, UK.

¹¹ GoLP/Instituto de Plasmas e Fusão Nuclear, Instituto Superior Técnico, Universidade de
¹² Lisboa, 1049-001, Lisboa, Portugal.

¹³ European Organization for Nuclear Research (CERN), CH-1211 Geneva 23, Switzerland.

¹⁴ GSI Helmholtzzentrum für Schwerionenforschung GmbH, Planckstraße 1 64291 Darmstadt,
¹⁵ Germany.

¹⁶ Lawrence Livermore National Laboratory, 7000 East Ave, Livermore, California, 94550,
¹⁷ USA.

¹⁸ STFC Rutherford Appleton Laboratory, Chilton, Didcot, OX11 0QX, UK.

¹⁹ University of Rochester Laboratory for Laser Energetics, Rochester, NY, 14623, USA.

²⁰ Science Institute, University of Iceland, Dunhaga 3, IS-107, Reykjavik, Iceland.

²¹ Division of Space and Plasma Physics, School of Electrical Engineering and Computer
²² Science, KTH Royal Institute of Technology, SE-100 44, Stockholm, Sweden.

²³ AWE, Aldermaston, Reading, Berkshire, RG7 4PR, UK.

²⁴ Max-Planck-Institut für Kernphysik, Saupfercheckweg 1, D-69117, Heidelberg, Germany.

²⁵ School of Applied Mathematics and Physical Sciences, National Technical University of
²⁶ Athens, Athens 157 72, Greece.

²⁷ Department of Physics, University of Strathclyde, Glasgow, G4 0NG, UK.

²⁸ *Corresponding author(s). E-mail(s): charles.arrowsmith@physics.ox.ac.uk;

Dated: November 21, 2024

29 Abstract

30 The generation of dense electron-positron pair beams in the laboratory can enable direct
 31 tests of theoretical models of γ -ray bursts and active galactic nuclei. We have successfully
 32 achieved this using ultra-relativistic protons accelerated by the Super Proton Synchrotron at
 33 CERN [1]. In the first application of this experimental platform, the stability of the pair beam
 34 is studied as it propagates through a metre-length plasma, analogous to TeV γ -ray induced
 35 pair cascades in the intergalactic medium. It has been argued that pair beam instabilities
 36 disrupt the cascade, thus accounting for the observed lack of reprocessed GeV emission from
 37 TeV blazars. If true this would remove the need for a moderate strength intergalactic magnetic
 38 field to explain the observations. We find that the pair beam instability is suppressed if the
 39 beam is not perfectly collimated or monochromatic, hence the lower limit to the intergalactic
 40 magnetic field inferred from γ -ray observations of blazars is robust.

41 Main

42 TeV-blazars are a class of active galactic nuclei (AGN) with relativistic jets pointing towards Earth which
 43 emit γ -rays with a hard spectrum extending to TeV energies [2]. These propagate through the intergalactic
 44 medium (IGM), often through cosmic voids where matter exists as a tenuous, collisionless plasma, and are
 45 expected to scatter with extragalactic background light, triggering electromagnetic cascades of electron-
 46 positron (e^\pm) pairs, which subsequently inverse-Compton scatter on cosmic microwave background (CMB)
 47 photons to produce GeV energy γ -rays. But this is at odds with astronomical observations accumulated over
 48 more than a decade which have set stringent limits on the expected GeV γ -rays [3]. The leading hypothesis
 49 is that e^\pm pairs are deflected by intergalactic magnetic fields (IGMF) [4], thereby the GeV emission is spread
 50 into diffuse halos that are not resolved by current γ -ray telescopes [5, 6] but should be detectable by the
 51 Cherenkov Telescope Array [7]. The required strength and coherence length of the magnetic field is however
 52 sufficiently large that an astrophysical origin is unlikely; it may well be a relic of the early Universe [8, 9].

53 An alternative possibility is that a substantial fraction of the pairs' energy is dissipated via electromag-
 54 netic beam-plasma instabilities [10–13], before they inverse-Compton scatter with CMB photons [14, 15].
 55 Such instabilities lead to exponential amplification of electromagnetic fields via the unstable separation of
 56 electrons and positrons into current filaments, and in extreme scenarios, significant dissipation of the bulk
 57 kinetic energy and the onset of collisionless shocks. Whether these indeed play a role in the blazar-induced
 58 pair cascade, and similar situations involving streaming e^\pm pairs such as in gamma-ray bursts (GRBs),
 59 depends on the initial linear stage of the instability (characterized by a linear growth rate), and subsequent
 60 quasi-linear evolution which determines the transition to the saturation stage. When non-idealized condi-
 61 tions are considered, for example finite divergence and energy spread, plasma kinetic theory suggests that
 62 such beam instabilities may be suppressed.

63 For relativistic pair beams with a low density compared with the ambient plasma, the fastest-growing
 64 modes of electromagnetic beam instability are oriented obliquely to the beam direction [16], with a charac-
 65 teristic scale comparable to the plasma skin depth, $\lambda_s = c/\omega_p$, where $\omega_p = (4\pi n_p e^2/m_e)^{1/2}$ is the plasma
 66 frequency, n_p is the ambient plasma electron density, e is the elementary charge and m_e is the electron rest
 67 mass. The theoretical growth rate for a monoenergetic pair beam is given by [12]:

$$\Gamma = \frac{\sqrt{3}}{2^{4/3}} \omega_p \left(\frac{n_\pm}{n_p \gamma_\pm} \right)^{1/3} \left[\frac{k_\perp^{2/3}}{k_\parallel^{2/3}} - \frac{3k_\perp^2}{8k_\parallel^2} (\Delta\theta)^2 \left(\frac{2n_p \gamma_\pm}{n_\pm} \right)^{2/3} \right], \quad (1)$$

68 where k_\parallel and k_\perp are the parallel and perpendicular components of the wavevector relative to the beam's
 69 propagation axis, whilst n_\pm , γ_\pm and $\Delta\theta = \Delta p_\perp/p_\parallel$ are the number density, relativistic Lorentz factor, and
 70 transverse momentum spread of the pair beam, respectively (see Supplementary Information). The factor
 71 in square brackets accounts for transverse thermal motion of the beam, which tends to unity for a suffi-
 72 ciently collimated beam, $\Delta\theta \ll (n_\pm/n_p \gamma_\pm)^{1/3}$, with the fastest-growing modes oriented transversely to beam
 73 propagation. However, if the transverse momentum spread is large enough, $\Delta\theta \gtrsim (n_\pm/n_p \gamma_\pm)^{1/3}$, particle
 74 trajectories cross the characteristic scale of unstable modes before current fluctuations can be amplified,
 75 leading to stabilisation of small-scale transverse modes, reduction of the growth rate, and tilting of the
 76 fastest-growing mode towards the longitudinal direction. This is likely to be important in the astrophysical
 77 context, where relativistic pair beams are neither perfectly collimated nor monoenergetic.

78 It has been argued that suppression of pair beam instability growth rates prevents their significant
 79 development before the pairs inverse-Compton scatter with CMB photons [17–19]. However, this conjecture
 80 is difficult to check using simulations due to their limited spatial and temporal range. Nor has the theory
 81 been validated experimentally due to the challenge of producing pair beams with the necessary high density

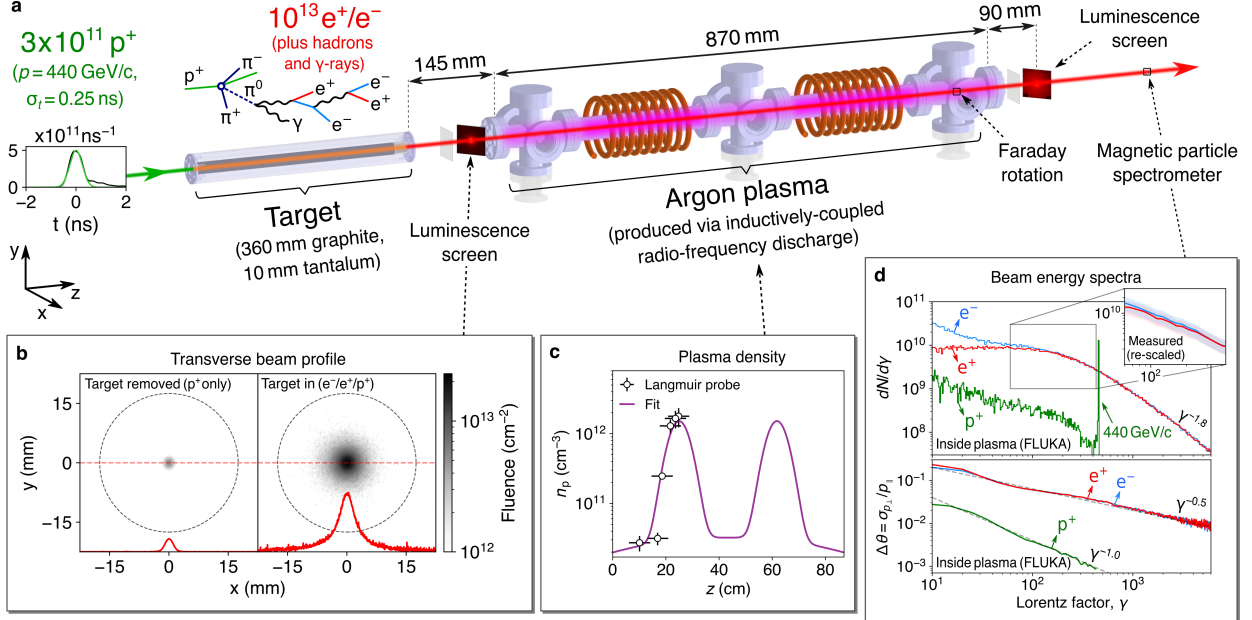


Fig. 1 Experimental setup. (a) Protons with $440 \text{ GeV}/c$ momentum are extracted from the SPS accelerator with temporal profile measured using an integrating current transformer (inset). The protons irradiate a solid target (360 mm graphite plus 10 mm tantalum) with a maximum fluence exceeding 3×10^{11} protons in a single bunch of duration 0.25 ns ($1-\sigma$) and transverse size $\sigma_r = 1 \text{ mm}$. A secondary beam is generated via hadronic and electromagnetic cascades, containing a dominating fluence of electron-positron pairs ($N_{e^\pm} > 10^{13}$), plus hadrons, γ -rays and other secondaries. (b) Measurements of the transverse beam profile using 70 mm \times 50 mm \times 0.25 mm chromium-doped ceramic (Chromox) luminescence screens, viewed by a digital camera at a standoff distance of 3.8 m. The spatial resolution is limited to $100 \mu\text{m}$ by the Chromox translucence. (c) Downstream of the target, the beam passes though a metre-length argon plasma produced by an inductively-coupled radio-frequency discharge. The longitudinal plasma density profile is measured using a Langmuir probe and confirmed during the experiment using optical emission spectroscopy. Pair beam filamentation due to beam-plasma instability is measured using a luminescence screen placed downstream of the plasma (camera positioned at a standoff distance 3.9 m), and a Faraday rotation diagnostic measures the growth of magnetic fields inside the plasma. (d) The electron and positron energy spectra are measured using a magnetic particle spectrometer (re-scaled according to the size of the collecting aperture) [1].

and quasi-neutrality [20]. But experimental studies now become possible due to our recent breakthrough demonstration that relativistic e^\pm pair beams can be efficiently produced using ultra-relativistic proton beams accelerated by the Super Proton Synchrotron (SPS) at CERN [1]. Here, we investigate the stability of e^\pm pair beams as they propagate through a metre-length ambient plasma to test whether the beam-plasma instabilities are indeed suppressed under non-idealized conditions, analogous to astrophysical situations involving e^\pm pairs streaming through the IGM. We discuss the implications for blazar pair cascades in cosmic voids and comment on the robustness of the lower limit to the IGMF inferred from observations of blazar γ -ray spectra.

The experimental setup is shown in Figure 1. Over 3×10^{11} protons are extracted from the SPS and delivered to the HiRadMat (High-Radiation to Materials) facility [21] with momentum $440 \text{ GeV}/c$ in a single LHC-type bunch (transverse size $\sigma_r = 1 \text{ mm}$ and duration $\sigma_t = 0.25 \text{ ns}$). The proton beam irradiates a custom designed solid target consisting of a graphite rod with a tantalum converter. Hadronic interactions of the protons with carbon nuclei generates a copious number of neutral pions (π^0), which decay to produce a highly-collimated beam of GeV-energy γ -rays. Inside the tantalum, the γ -rays trigger electromagnetic cascades of relativistic electron-positron pairs, leading to a secondary quasi-neutral beam containing over 10^{13} relativistic e^\pm pairs, along with a much smaller number of protons and other secondary products [22]. Characterization of the secondary beam is provided by Monte-Carlo simulations performed using FLUKA [23–25], a standard code capable of accurately describing hadronic and electromagnetic cascades in the target. The simulations are validated against luminescence screen measurements of the transverse beam profile and the e^\pm energy spectra in a magnetic particle spectrometer [1]. The pairs exhibit a multi-power-law spectrum in momentum, $dN_\pm/dE \propto E^{-m}$, with spectral index $m \approx 1 - 2$. The beam propagates through an inductively coupled argon discharge plasma, with the plasma conditions (density and temperature) measured prior to the experiment using a Langmuir probe, and confirmed non-invasively during the experiment using optical emission spectroscopy (details provided in the Supplementary Information). The plasma density is characterised by two identical bumps reaching a peak density of $n_p = 2 \times 10^{12} \text{ cm}^{-3}$ when the discharge vessel is filled with argon to a pressure $p_g = 4 \text{ Pa}$ and the inductive coils are supplied with 1 kW of radio-frequency power, corresponding to an absorbed power $P_{\text{abs}} = 240 \text{ W}$ [26]. Importantly, the basic conditions required to sustain collective plasma modes in the laboratory experiment are fulfilled,

specifically that the physical size of the pair beam exceeds the expected size of current filaments. Similar to many astrophysical situations, the ambient plasma is relativistically cold ($k_B T_e \sim \text{eV}$), and the plasma is collisionless (the rate of electron-neutral collisions, ν_{en} , and electron-ion collisions, ν_{ei} , is much smaller than the plasma frequency, ω_p), meaning a collisionless kinetic description of the plasma is justified. The development of beam-plasma instability is probed using two diagnostics. The generation of magnetic fields is measured using a time-resolved, magneto-optic Faraday rotation probe, positioned near the end of the plasma discharge (81 cm downstream of the beam entry), and modulations in the transverse beam profile arising from the formation of electron/positron filaments is measured using a chromium-doped alumina (Chromox) luminescence screen positioned 90 mm downstream of the plasma (see Methods).

Experimental results

The experimental results of both diagnostics are summarized in Figure 2. The inset of Figure 2a shows the orientation of the magneto-optic terbium gallium garnet (TGG) crystal used to perform the Faraday rotation measurement, positioned 81 cm into the plasma. A linearly-polarized laser beam ($\lambda = 532 \text{ nm}$) is passed twice through the TGG crystal, reflecting at the rear surface. Magnetic fields oriented along the length of the crystal will cause the polarization of the laser beam to rotate, which is detected by a time-resolved measurement of the intensity of the laser after passing through a second polarizing filter oriented at 45° to the initial polarization. The light is collected by a fast photodiode ($t_{10-90\%} = 0.44 \text{ ns}$) and the measured intensity is given by $V = V_0 \cos^2(\langle B \rangle \mathcal{V} L + 45^\circ)$, where $\langle B \rangle = \frac{2}{L} \int \mathbf{B} \cdot \hat{\mathbf{x}} dx$ is the mean component of the magnetic field along the propagation axis of the laser beam, $\mathcal{V} = 217 \pm 15 \text{ rad T}^{-1} \text{ m}^{-1}$ is the measured Verdet constant, $L = 12 \text{ mm}$ is the length of the crystal, and $V_0 = 14 \text{ mV}$ is the intensity measured when the two polarizing filters are aligned and $\langle B \rangle = 0$. The pre-factor of 2 accounts for the double pass of the crystal. Magnetic fields can be measured on the timescales of the beam duration ($t_{10-90\%} = 0.42 \text{ ns}$) with a single-shot sensitivity limited to $B_{\text{sens}} = 5 \text{ mT}$ by the intrinsic electronic noise (full characterization provided in the Supplementary Information). Since the timing is consistent between shots, the signal-to-noise ratio can be improved by combining signals from multiple shots. Five measurements of the pair beam are obtained and the mean intensity change (ΔV) and standard deviation are plotted in Figure 2a, showing

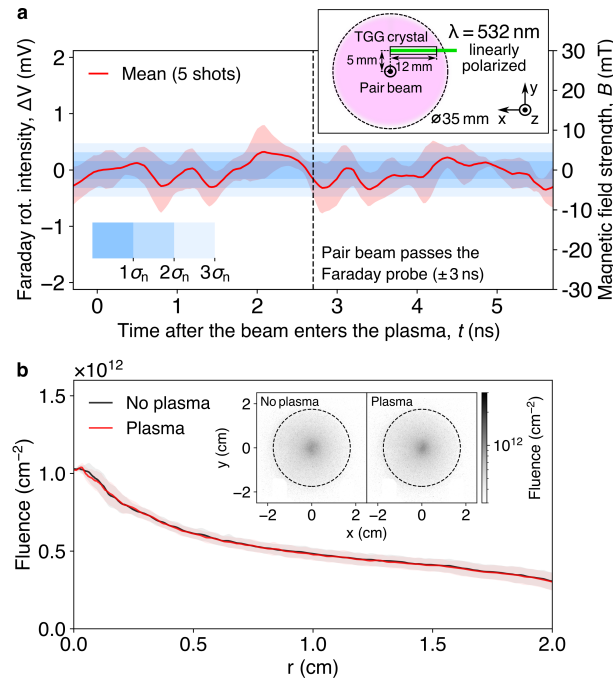


Fig. 2 Magnetic field and beam profile measurements. (a) Magnetic fields are measured at the end of the plasma using a time-resolved Faraday rotation technique. A linearly polarized laser beam ($\lambda = 532 \text{ nm}$) is passed twice through a magneto-optic crystal (TGG, 12 mm length, 2 mm diameter), suspended in the plasma by a ceramic re-entrant tube (orientation shown in the inset), before passing through a second polarizing filter offset by 45° from the initial polarization. The change in laser intensity measured by a fast photodiode ($\Delta V = V - V_0/2$) is plotted as a function of time, with the pair beam expected to pass the probe 2.7 ns after the beam enters the plasma (the signal is shown a few ns before and afterwards to account for the uncertainty in the exact timing). The mean signal from five shots is plotted, with corresponding standard deviation represented by the red shaded region. The blue shaded regions show the standard deviation of the intrinsic electronic noise. (b) The transverse beam profile is measured using a Chromox luminescence screen positioned 90 mm downstream of the plasma discharge. The residual primary proton beam is subtracted from the images (see Methods), leaving the fluence of electron-positron pairs (plus additional secondaries). The radial lineouts are shown when the plasma is present ($p_g = 4 \text{ Pa}$, $P_{\text{abs}} = 240 \text{ W}$) and when there is no plasma ($p_g = 0.5 \text{ Pa}$, $P_{\text{abs}} = 0 \text{ W}$), with the image data shown in the inset. The shaded regions represent the standard deviation of the lineout pixel counts.

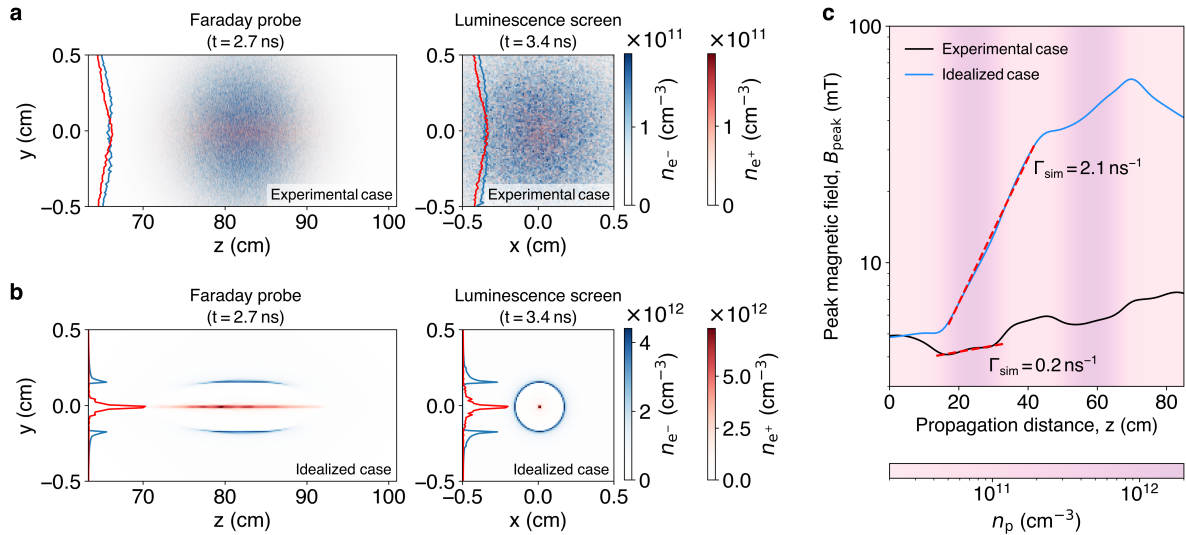


Fig. 3 Three-dimensional particle-in-cell simulations. 3D simulations of the beam-plasma interaction are performed using the particle-in-cell code OSIRIS [27] for two cases: (a) with conditions closely resembling the experimental beam and ambient plasma (labelled ‘experimental’), and (b) an idealized case with a collimated, monoenergetic ($\gamma_{\pm} = 10^3$) pairs (labelled ‘idealized’). In (a) and (b), the left panels show a central slice of the electron and positron densities in the longitudinal plane (x - z) at the time when the beam passes the Faraday probe ($t = 2.7$ ns after entering the plasma), whilst the right panels show a central slice of the transverse plane (x - y) when the beam passes the downstream luminescence screen ($t = 3.4$ ns). (c) The peak magnetic field is plotted as a function of propagation distance through the plasma, with the background shading showing the ambient plasma density. The maximum growth rate of the peak magnetic field is obtained by the shown fits (red-dashed). The anti-correlation of magnetic field and plasma density is an effect of the varying level of return current.

that the maximum deviation of the mean signal corresponds to $\langle B \rangle = 5$ mT, small enough that a precise measurement remains limited by the electronic noise floor. We conclude that an upper limit of the measured field is $\langle B \rangle_{\text{exp}} \leq 5$ mT, given that a value consistently larger than 5 mT in five repeated measurements leads to a statistically significant detectable signal (at the 2.2σ level). A corresponding upper bound of the instability growth rate is estimated assuming that the magnetic field grows exponentially from an azimuthally oriented seed field, B_0 , produced by the net current of the residual proton beam propagating on-axis: $\langle \Gamma_{\text{exp}} \rangle = t_{\text{prop}}^{-1} \log [\langle B \rangle_{\text{exp}} / B_0] \leq 0.7$ ns $^{-1}$, where $t_{\text{prop}} = 2.7$ ns is the propagation time of the pair beam through plasma, and $B_0 = 0.78 \pm 0.13$ mT is calculated from the precise net current distribution obtained from a FLUKA simulation (see Supplementary Information). For comparison, the beam instability growth rate calculated from linear kinetic theory (using Eq. 1) assuming a perfectly collimated beam gives a maximum growth rate $\Gamma = 2.0$ ns $^{-1}$, significantly higher than the growth rate observed in the experiment. The slower observed rate is explained by suppression due to the finite thermal spread of the pairs in the experiment.

Further experimental evidence for the suppression of the growth rate is provided by the images of the transverse beam profile (Figure 2b), showing that there is no observable difference when the plasma is present. It is possible that a small current separation is obscured due to the equal sensitivity of the screen to electrons and positrons, but the development of high-contrast, mm-scale filaments on fast timescales can be ruled out and a slower-than-predicted growth rate remains the most plausible explanation. A reduced growth rate can result from reduction of the pair beam’s density as it diverges, but it is calculated that this cannot explain the extent of the observed suppression.

Particle-in-cell simulations

The effects of finite thermal spread of the e^{\pm} pairs are explored further by performing three-dimensional (3D3V) particle-in-cell (PIC) simulations using the fully relativistic, massively parallel PIC code OSIRIS [27]. In the simulations, a moving window follows an electron-positron-proton beam at the speed of light to model conditions closely resembling the experimental pair beam and the ambient plasma (see Methods). The idealized case of a perfectly collimated, monoenergetic pair beam is considered for comparison. The results are shown in Figure 3. In both cases, current separation of electrons and positrons is observed on the scale of the plasma skin depth. The residual primary protons co-propagating on-axis provide a seed magnetic field for the instability, which causes the positron density to increase on-axis and the azimuthal magnetic field is amplified exponentially. Otherwise, the protons do not play a dynamical role during the experiment timescale due to their much larger inertia. In the case where the e^{\pm} pairs are collimated and monoenergetic, filaments become completely separated and emerge on much smaller spatial scales. The peak

168 magnetic field is vastly increased ($B_{\max} = 60$ mT) with a peak growth rate well-matched by the theoretical
 169 prediction of Eq. 1 ($\Gamma_{\text{sim}} = 2.1 \text{ ns}^{-1}$), as shown in Figure 3c. By contrast, when the finite thermal spread of
 170 pairs is accounted for, the small-scale modes are stabilized, and the peak magnetic field and growth rate are
 171 significantly reduced ($B_{\max} = 7$ mT, $\Gamma_{\text{sim}} = 0.2 \text{ ns}^{-1}$). The simulated magnetic fields provide a prediction
 172 of the Faraday rotation measurement of $\langle B \rangle_{\text{sim}} = 1.7$ mT, leading to an estimated average growth rate
 173 $\langle \Gamma_{\text{sim}} \rangle = 0.3 \text{ ns}^{-1}$, consistent with the experimentally-obtained bound $\langle \Gamma_{\text{exp}} \rangle \leq 0.7 \text{ ns}^{-1}$.

174 Discussion

175 To assess whether beam-plasma instabilities are important for blazar-induced pair beams propagating
 176 through cosmic voids, the characteristics of the blazar pair cascade are obtained using a Monte-Carlo
 177 model, described in Elyiv et al. [28] and used by e.g. Neronov & Vovk [4] and Miniati & Elyiv [17] (mod-
 178 elled parameters given in Table 1). The blazar spectral emission is taken to be a power-law distribution,
 179 $dN_{\gamma}/dE_{\gamma} \propto E_{\gamma}^{-1.8}$ in the range $10^3 \leq E_{\gamma}/m_e c^2 \leq 10^8$, with equivalent isotropic luminosity $10^{45} \text{ erg s}^{-1}$,
 180 using a model for the extragalactic background light described by Aharonian [29]. The obtained pair den-
 181 sity is model-dependent, but $n_{\pm, \text{blz}} \sim 10^{-23} (1+z)^{9.5} \text{ cm}^{-3}$ [14, 17] is considered to be reasonable, where
 182 z is the redshift and this dependence is valid for TeV blazars with $z \lesssim 1$ [14]. The mean Lorentz factor of
 183 pairs is $\langle \gamma_{\pm} \rangle \sim 10^5$, whilst pairs that inverse-Compton scatter with CMB photons to produce GeV emis-
 184 sion have a much higher Lorentz factor ($\gamma_{\pm} \sim 10^7$). The density of free electrons in the void is estimated
 185 by $n_{p, \text{IGM}} = \Omega_b f_{\text{IGM}} \rho_c / m_p$, where Ω_b is the cosmological baryon density parameter, f_{IGM} is the relative
 186 fraction of baryons in the IGM, m_p is the proton rest mass, and $\rho_c = 3H_0^2/8\pi G$ is the critical mass density
 187 of the Universe, where H_0 is the Hubble constant and G is the gravitational constant. The IGM is assumed
 188 to be fully ionized [30]. The fraction of baryons in the IGM, f_{IGM} , is constrained by recent measurements
 189 of the dispersion measure of extragalactic fast radio bursts to be $f_{\text{IGM}} \approx 0.4 - 0.8$ [31, 32]. A void den-
 190 sity $n_{p, \text{IGM}} = 2 \times 10^{-7} (1+z)^3 \text{ cm}^{-3}$ is obtained by assuming $f_{\text{IGM}} = 0.8$ and using standard cosmological
 191 parameters from Planck [33]: $\Omega_b h^2 = 0.02237 \pm 0.00015$, where $h = H_0/100 \text{ km s}^{-1} \text{ Mpc}^{-1}$.

192 Under these conditions, $\Delta\theta \gg (n_{\pm}/n_p \gamma_{\pm})^{1/3}$, and electromagnetic beam instability is strongly sup-
 193 pressed. The dependence of the linear growth rate on beam and plasma parameters in the limit of large $\Delta\theta$
 194 can be obtained from Eq. 1: $\Gamma = \sqrt{2/3} \omega_p (n_{\pm}/2n_p \gamma_{\pm})^{2/3} / \Delta\theta$, and used to scale the experimentally obtained
 195 upper bound of the growth rate to estimate the maximum growth rate for the blazar pair cascade:

$$\Gamma_{\text{blz}} [\text{s}^{-1}] \leq 3 \times 10^{-11} \left(\frac{\Gamma_{\text{exp}}}{0.7 \text{ ns}^{-1}} \right). \quad (2)$$

196 The linear growth timescale, $\tau_{\text{ins}} \equiv 1/\Gamma_{\text{blz}}$, is plotted in Figure 4 alongside the theoretical estimates of
 197 Eq. 1 for blazar-jet pair densities in the range $n_{\pm, \text{blz}} = 10^{-25} - 10^{-21} \text{ cm}^{-3}$, and compared with the
 198 inverse-Compton cooling time of pairs with CMB photons:

$$\tau_{\text{IC}} [\text{s}] = 3.8 \times 10^{13} \left(\frac{E_e}{1 \text{ TeV}} \right)^{-1} (1+z)^{-4}. \quad (3)$$

199 Although the scaled growth rate is suppressed compared with the predicted rate for collimated, monoener-
 200 getic pairs, it may still be large compared with the rate of inverse-Compton cooling, leading to the possible
 201 generation of transverse magnetic fields and angular spreading of the pair beam. However, the magnetic
 202 field is estimated to saturate at the field strength

$$B_{\perp, \text{sat}} [\text{mT}] \lesssim 2 \times 10^{-26} \left(\frac{\Gamma_{\text{blz}}}{3 \times 10^{-11} \text{ s}^{-1}} \right)^2, \quad (4)$$

203 corresponding to the particle-trapping condition [34]. This is compared in Figure 4 with lower limits on the
 204 IGMF imposed by the lack of observed GeV cascade emission in Fermi/LAT and MAGIC telescope data:
 205 $B_{\text{IGM}} [\text{mT}] \geq 4 \times 10^{-11} (\lambda_B/4 \times 10^{-10} \text{ pc})^{-1/2}$, assuming a magnetic field coherence length comparable to
 206 the ambient plasma's skin depth ($\lambda_B \sim \lambda_s$). This shows that even if many e -folding lengths of instability
 207 can develop, the generated magnetic fields are much too small to cause the required angular spreading to
 208 explain blazar-jet observations. After the saturation of electromagnetic modes, longitudinal electrostatic
 209 oscillations may continue to grow at the slower quasi-linear rate [35], but the velocity spread of pairs is
 210 much too large for significant coupling of the pair beam's kinetic energy into large-amplitude, resonantly
 211 driven plasma waves. We can thus rule out experimentally that beam-plasma instabilities affect TeV blazar
 212 pair cascades, hence the inferred lower bound on the intergalactic magnetic field strength is robust.

Table 1 Pair beam and plasma parameters in the experiment and blazar jets in cosmic voids.

| Parameter | Experiment | Typical blazar jet (luminosity 10^{45} erg s $^{-1}$) at a distance 300 Mpc |
|---|--------------------|--|
| Ambient plasma density, n_p (cm $^{-3}$) | 10^{12} | 2×10^{-7} |
| Collisionality, ν_e/ω_p | 10^{-3} | 10^{-13} |
| Pair density, n_{\pm} (cm $^{-3}$) | 5×10^{10} | 10^{-23} |
| Mean Lorentz factor, $\langle \gamma_{\pm} \rangle$ | 10^3 | 10^5 |
| Transverse momentum spread, $\Delta\theta$ | 0.025 | 10^{-4} |

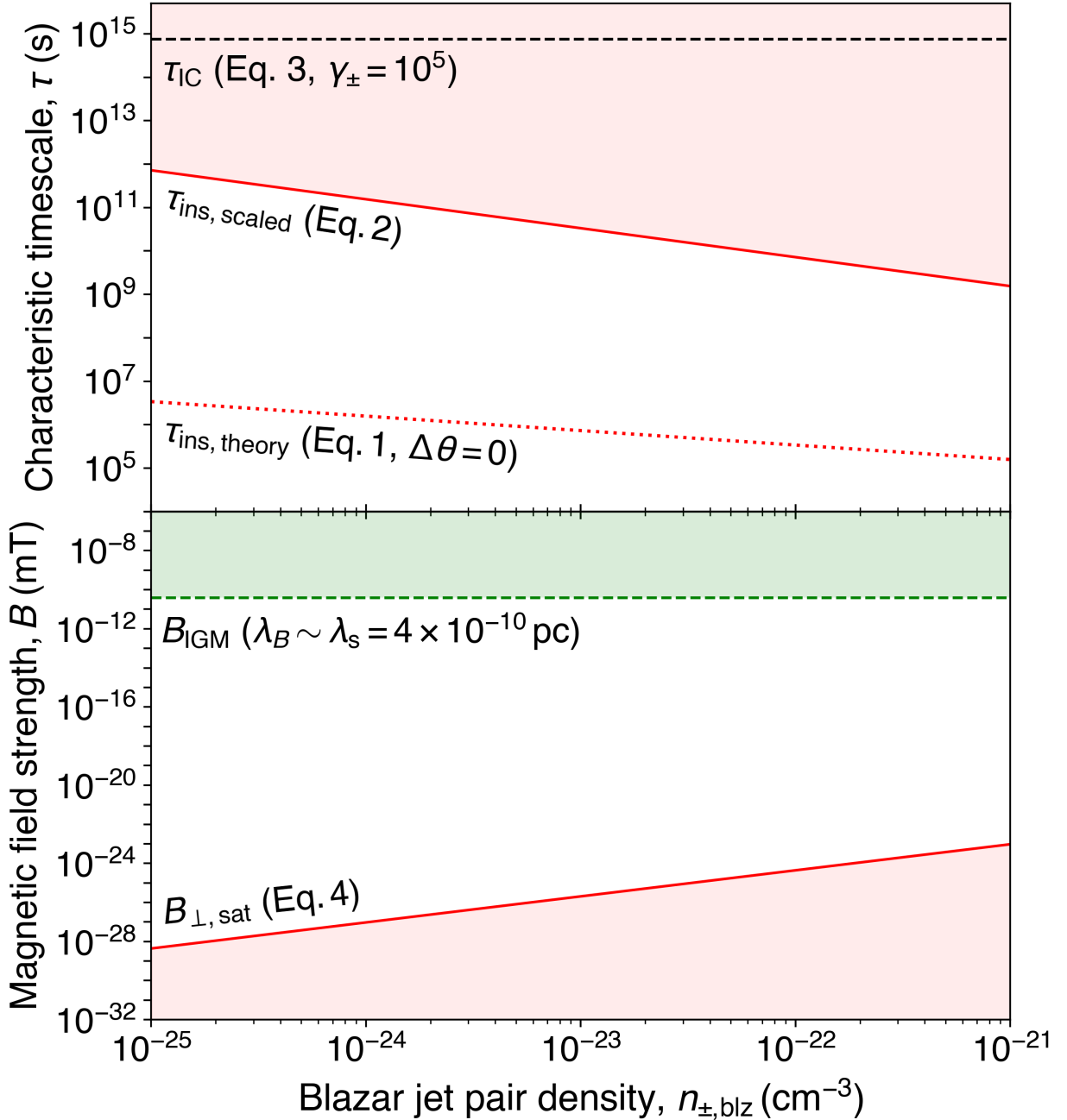


Fig. 4 Characteristic timescales and magnetic field strengths relevant to blazar-induced pair beams in cosmic voids. Upper panel: The experimentally obtained bound on the growth rate of electromagnetic pair beam instability ($\Gamma_{\text{exp}} \leq 0.7 \text{ ns}^{-1}$) is scaled using Eq. 2 to obtain a lower bound on the linear growth rate for blazar-induced pair beams propagating through cosmic void (red solid). The growth timescale is much larger than theoretical predictions assuming a collimated, monoenergetic pair beam (Eq. 1, $\Delta\theta = 0$, red dotted), but short compared with the inverse-Compton cooling time of pairs with CMB photons (Eq. 3, $\gamma_{\pm} = 10^5$, black dashed). Lower panel: The strength of the magnetic field at instability saturation is similarly scaled from the experimentally obtained bound (red solid), and compared with lower bounds on the magnetic field strength based on blazar spectral measurements, at a coherence length comparable to the ambient skin depth (green dashed). It is assumed in all cases that the redshift is $z \lesssim 1$.

213 **References**

- 214 [1] Arrowsmith, C. D., Simon, P., Bilbao, P. J. *et al.* Laboratory realization of relativistic pair-plasma
215 beams. *Nature Communications* **15**, 5029 (2024).
- 216 [2] Şentürk, G. D., Errando, M., Böttcher, M. & Mukherjee, R. Gamma-ray Observational Properties of
217 TeV-detected Blazars. *The Astrophysical Journal* **764**, 119 (2013).
- 218 [3] Aharonian, F. *et al.* A low level of extragalactic background light as revealed by γ -rays from blazars.
219 *Nature* **440**, 1018–1021 (2006).
- 220 [4] Neronov, A. & Vovk, I. Evidence for strong extragalactic magnetic fields from Fermi observations of
221 TeV blazars. *Science* **328**, 73–75 (2010).
- 222 [5] Archambault, S. *et al.* Search for magnetically broadened cascade emission from blazars with VERITAS.
223 *The Astrophysical Journal* **835**, 288 (2017).
- 224 [6] Ackermann, M. *et al.* The search for spatial extension in high-latitude sources detected by the Fermi
225 Large Area Telescope. *The Astrophysical Journal Supplement Series* **237**, 32 (2018).
- 226 [7] Abdalla, H. *et al.* Sensitivity of the Cherenkov Telescope Array for probing cosmology and fundamental
227 physics with gamma-ray propagation. *Journal of Cosmology & Astroparticle Physics* **2021**, 048 (2021).
- 228 [8] Miniati, F., Gregori, G., Reville, B. & Sarkar, S. Axion-Driven Cosmic Magnetogenesis during the
229 QCD Crossover. *Physical Review Letters* **121**, 021301 (2018).
- 230 [9] Vachaspati, T. Progress on cosmological magnetic fields. *Reports on Progress in Physics* **84**, 074901
231 (2021).
- 232 [10] Weibel, E. S. Spontaneously growing transverse waves in a plasma due to an anisotropic velocity
233 distribution. *Physical Review Letters* **2**, 83 (1959).
- 234 [11] Fried, B. D. Mechanism for instability of transverse plasma waves. *Physics of Fluids* **2**, 337 (1959).
- 235 [12] Fainberg, Y. B., Shapiro, V. & Shevchenko, V. Nonlinear theory of interaction between a monochromatic
236 beam of relativistic electrons and a plasma. *Soviet Physics JETP* **30**, 528 (1970).
- 237 [13] Rudakov, L. I. Collective Slowing Down of an Intense Beam of Relativistic Electrons in a Dense Plasma
238 Target. *Soviet Journal of Experimental and Theoretical Physics* **32**, 1134 (1971).
- 239 [14] Broderick, A. E., Chang, P. & Pfrommer, C. The cosmological impact of luminous TeV blazars. I.
240 Implications of plasma instabilities for the intergalactic magnetic field and extragalactic gamma-ray
241 background. *The Astrophysical Journal* **752**, 22 (2012).
- 242 [15] Schlickeiser, R., Ibscher, D. & Supsar, M. Plasma effects on fast pair beams in cosmic voids. *The*
243 *Astrophysical Journal* **758**, 102 (2012).
- 244 [16] Shaisultanov, R., Lyubarsky, Y. & Eichler, D. Stream instabilities in relativistically hot plasma. *The*
245 *Astrophysical Journal* **744**, 182 (2011).
- 246 [17] Miniati, F. & Elyiv, A. Relaxation of blazar-induced pair beams in cosmic voids. *The Astrophysical*
247 *Journal* **770**, 54 (2013).
- 248 [18] Sironi, L. & Giannios, D. Relativistic pair beams from TeV blazars: a source of reprocessed GeV
249 emission rather than intergalactic heating. *The Astrophysical Journal* **787**, 49 (2014).
- 250 [19] Perry, R. & Lyubarsky, Y. The role of resonant plasma instabilities in the evolution of blazar-induced
251 pair beams. *Monthly Notices of the Royal Astronomical Society* **503**, 2215–2228 (2021).
- 252 [20] Chen, H. & Fiúza, F. Perspectives on relativistic electron–positron pair plasma experiments of
253 astrophysical relevance using high-power lasers. *Physics of Plasmas* **30**, 020601 (2023).
- 254 [21] Efthymiopoulos, I. *et al.* Petit-Jean-Genaz, C. (ed.) *HiRadMat: A New Irradiation Facility for Material*
- 255 Testing at CERN.
- (ed.Petit-Jean-Genaz, C.) *2nd International Particle Accelerator Conference, San*

- 256 *Sebastian, Spain, 4 – 9 Sep 2011*, 1665–1667 (2011).
- 257 [22] Arrowsmith, C. D. *et al.* Generating ultradense pair beams using 400 GeV/c protons. *Physical Review Research* **3**, 023103 (2021).
- 259 [23] Ahdida, C. *et al.* New Capabilities of the FLUKA Multi-Purpose Code. *Frontiers in Physics* **9**, 788253 (2022).
- 261 [24] Battistoni, G. *et al.* Overview of the FLUKA code. *Annals of Nuclear Energy* **82**, 10–18 (2015).
- 262 [25] Vlachoudis, V. *et al.* FLAIR: A Powerful but User Friendly Graphical Interface for FLUKA. *Proc. Int. Conf. on Mathematics, Computational Methods & Reactor Physics (M&C 2009)*, Saratoga Springs, New York (2009).
- 265 [26] Arrowsmith, C. D., Dyson, A., Gudmundsson, J. T., Bingham, R. & Gregori, G. Inductively-coupled plasma discharge for use in high-energy-density science experiments. *Journal of Instrumentation* **18**, P04008 (2023).
- 268 [27] Fonseca, R. A. *et al.* in *OSIRIS: A three-dimensional, fully relativistic particle in cell code for modeling plasma based accelerators* (eds Sloot, P. M. A., Hoekstra, A. G., Tan, C. J. K. & Dongarra, J. J.) *Computational Science — ICCS 2002, International Conference Amsterdam, The Netherlands, April 21–24, 2002 Proceedings, Part III*, Vol. 2331 of *Lecture Notes in Computer Science* 342–351 (Springer-Verlag, Berlin, Germany, 2002).
- 273 [28] Elyiv, A., Neronov, A. & Semikoz, D. Gamma-ray induced cascades and magnetic fields in the intergalactic medium. *Physical Review D* **80**, 023010 (2009).
- 275 [29] Aharonian, F. A. *TeV blazars and cosmic infrared background radiation*, Vol. 27 of *International Cosmic Ray Conference*, 250 (2001). [astro-ph/0112314](#).
- 277 [30] Meiksin, A. A. The physics of the intergalactic medium. *Reviews of Modern Physics* **81**, 1405 (2009).
- 278 [31] Li, Z. *et al.* Cosmology-independent estimate of the fraction of baryon mass in the IGM from fast radio burst observations. *The Astrophysical Journal* **876**, 146 (2019).
- 280 [32] Lemos, T., Gonçalves, R. S., Carvalho, J. C. & Alcaniz, J. S. Cosmological model-independent constraints on the baryon fraction in the IGM from fast radio bursts and supernovae data. *The European Physical Journal C* **83**, 138 (2023).
- 283 [33] Aghanim, N. *et al.* Planck 2018 results-VI. Cosmological parameters. *Astronomy & Astrophysics* **641**, A6 (2020).
- 285 [34] Davidson, R. C., Hammer, D. A., Haber, I. & Wagner, C. E. Nonlinear development of electromagnetic instabilities in anisotropic plasmas. *The Physics of Fluids* **15**, 317–333 (1972).
- 287 [35] Breizman, B. & Ryutov, D. Quasilinear relaxation of an ultrarelativistic electron beam in a plasma. *Soviet Physics JETP* **33** (1971).
- 289 [36] Lynch, G. R. & Dahl, O. I. Approximations to multiple Coulomb scattering. *Nuclear Instruments and Methods in Physics Research Section B: Beam Interactions with Materials and Atoms* **58**, 6–10 (1991).

291 **Methods**

292 **Electron-positron pair production target**

293 The target used to produce the secondary beam consists of a 360 mm length cylinder of isostatic graphite
294 (SGL Carbon R6650, 1.84 g cm^{-3}) and a 10 mm thickness tantalum converter, both with a diameter of
295 20 mm. The graphite and tantalum are encased inside a 400 mm length, 50 mm diameter cylinder of high-
296 strength T9 aluminium alloy that acts as both a confinement vessel and a heat sink. The tantalum is press-
297 fit to ensure maximal thermal contact. 2 mm thickness expanded graphite pieces (SGL Carbon Sigraflex,
298 1 g cm^{-3}) separate the target components to allow thermal expansion and reduce contact stresses during
299 irradiation, while 2 mm thickness Sigradur G glassy carbon beam windows are clamped onto either end of
300 the target by aluminium flanges with Viton O-rings to seal the target materials hermetically. Radiative
301 and convective cooling via the outer surface of the target housing leads to cooling of the target to room
302 temperature within a few seconds following the beam impact, while the beam-induced maximum strain of
303 the tantalum remains in all cases well below its plastic deformation limit, i.e. the target is not destroyed
304 when irradiated by the proton beam and can be reused for many (potentially thousands of) shots.

305 **Inductively coupled argon plasma discharge**

306 The plasma discharge is composed of a vacuum chamber constructed from three six-way port crosses (non-
307 ferrous, 304L-grade stainless steel), separated by two sections of glass tube (15 cm length), terminated at
308 each end by a 4 mm-thick glassy carbon beam window. The total length of the discharge region is $L = 87 \text{ cm}$,
309 with an inner diameter $d = 3.5 \text{ cm}$. Inductive coils wrap around the sections of glass tube (1 cm diameter
310 copper pipe, with 8.5 turns, and coil-winding inner diameter 7.5 cm). The coils and surrounding metallic
311 segments of the chamber are connected to a zero ground potential. The vacuum pump, argon gas line
312 and Faraday probe are attached at the port crosses. Before operation, the chamber is evacuated to a base
313 pressure $p_{g,\text{base}} = 5 \text{ mPa}$, before filling with argon gas (purity 99.999%) to a pressure $p_g = 4 \text{ Pa}$. Radio-
314 frequency power is supplied to the coils at a frequency $f = 13.56 \text{ MHz}$ using a commercially available 1
315 kW radio-frequency power generator (Advanced Energy CESAR 1310) via an impedance-matching network
316 (Advanced Energy Navio). The power absorbed by the plasma corresponds to approximately 25% of the
317 supplied power. A plasma is produced by inductive coupling inside the coils with plasma density exceeding
318 $n_p \gtrsim 10^{12} \text{ cm}^{-3}$, whilst a lower density plasma ($n_p \sim 10^{10} - 10^{11} \text{ cm}^{-3}$) is sustained between the coils by
319 electrostatic/capacitive coupling. The discharge is ignited several seconds before the beam's arrival and is
320 deactivated several seconds after the beam has passed. Further details and extensive plasma characterization
321 are provided in Ref. [26].

322 **Time-resolved magneto-optic Faraday rotation probe**

323 A continuous-wave diode laser (Z-Laser ZM18, $\lambda = 532 \text{ nm}$, $P = 40 \text{ mW}$) is transported to the Faraday
324 probe's location via optical fibre and linearly polarized using a nanoparticle linear film polarizer, chosen for
325 its high extinction ratio (10,000:1), high transmission ratio (73%) at $\lambda = 532 \text{ nm}$ and high damage threshold.
326 The laser beam is split using a 50:50 beamsplitter and the transmitted beam is used as a reference beam to
327 monitor changes in the intensity of the probe laser beam, whilst the reflected beam is directed transversely
328 to the particle-beam axis through a 12 mm length, 2 mm diameter terbium-gallium-garnet (TGG) magneto-
329 optic crystal suspended in the plasma at the end of a ceramic re-entrant tube (inner length 70 mm, outer
330 diameter 5 mm). The crystal is positioned 81 cm into the plasma at a closest distance of 5 mm to the particle-
331 beam axis (orientation shown in Figure 2). The crystal has an anti-reflective coating on the front surface
332 and a highly reflective coating on the rear surface to reflect the probe beam so that it makes a double
333 pass of the crystal, thereby doubling the Faraday rotation for a given magnetic field. The reflected probe
334 beam passes through a second linear polarizer oriented at a 45° angle to the first and is coupled into a 7 m
335 length optical fibre (silica core, glass clad, step index with 0.22 NA, $\phi 200 \mu\text{m}$ core). The light is collected
336 by a 2 GHz bandwidth photodiode (Thorlabs DET025AFC/M) and a shielded coaxial cable connects the
337 photodiode to a 3 GHz oscilloscope (LeCroy WavePro 7300A). A schematic of the design is provided in the
338 Supplementary Information along with measurements of the Verdet constant, intrinsic noise and instrument
339 response function, measuring instrument sensitivity to magnetic fields of magnitude $B_{\text{sens}} = 5 \text{ mT}$ and a
340 time resolution of 0.44 ns (10 – 90% rise time). The Verdet constant of the crystal is measured again at the
341 end of the beam time to confirm that the instrument's sensitivity has not degraded due to radiation damage.

342 **Chromium-doped alumina luminescence screens**

343 Chromium-doped alumina-ceramic luminescence screens (Chromox, Al_2O_3 : 99.5%, Cr_2O_3 : 0.5%) are used
344 to measure the transverse beam profile before and after the beam passes through the plasma. When energy

345 is deposited in the screen by ionizing particles and radiation, luminescence light is emitted isotropically,
 346 strongest at wavelengths $\lambda_1 = 691$ nm, and $\lambda_2 = 694$ nm with decay times 3 – 6 ms. Screens are oriented
 347 at 45° to the beam path and viewed directly by a digital camera (Basler acA1920-40gm GigE camera with
 348 Sony IMX249 CMOS sensor and Canon EF 75 – 300 mm f/4-5.6 III lens) at a standoff distance 4 m with an
 349 exposure time 24 ms. It is reasonably assumed that the vast majority of particles incident on the screens are
 350 relativistic and deposit approximately the same amount of energy in a minimum-ionizing fashion. The spatial
 351 resolution is limited due to screen translucence to 100 μm (attenuation length, $\mu = 0.8 \text{ mm}^{-1}$), capable of
 352 resolving the filament formation in the pair beam since the size of unstable modes is expected to be several
 353 mm. The screen downstream of the plasma is positioned $d_{\text{scr}} = 90$ mm from the glassy carbon beam window,
 354 and a blocker foil (50 μm aluminium) is placed before the screen to minimize stray optical light. In Figure 2,
 355 the residual protons in the transverse beam profile are subtracted from the raw image by fitting the proton
 356 peak to a 2D Gaussian with initial parameters $\sigma_x = \sigma_y = 1$ mm and integrated intensity corresponding
 357 to the expected number of residual primary protons that do not significantly scatter inelastically with the
 358 target, a fraction given by $N_{\text{res}}/N_{\text{inc}} = \exp(-L_C/\lambda_C) \exp(-L_{\text{Ta}}/\lambda_{\text{Ta}}) = 0.42$, where $L_C = 360$ mm and
 359 $L_{\text{Ta}} = 10$ mm are the lengths of graphite and tantalum, and $\lambda_C = 466$ mm and $\lambda_{\text{Ta}} = 115$ mm are their
 360 corresponding nuclear interaction lengths. The calculation of N_{res} is in agreement with FLUKA Monte-
 361 Carlo simulations. Coulomb scattering of e^\pm pairs in the glassy carbon beam window is only expected to
 362 significantly affect the pairs with a much lower energy than the mean, with a point source diverging to a
 363 size $\sigma_{\text{spread}} \approx 0.3 \text{ mm} (\gamma_\pm/\langle\gamma_\pm\rangle)^{-1}$ [36].

364 Particle-in-cell (PIC) simulations

365 Three-dimensional (3D3V) PIC simulations were performed using the OSIRIS code at the exascale LUMI
 366 supercomputer (Finland). Simulations use a moving window travelling at c along the z -direction that follows
 367 relativistic electrons, positrons and protons in the secondary beam as they propagate through the ambient
 368 plasma. The electron-positron-proton beam is initialised before entrance of the plasma, centred at $z =$
 369 -20 cm and $x = y = 0$. The density and momentum phase-space distributions are accurately modelled by
 370 fitting analytical forms to the distributions at the entrance of the plasma cell, after the glassy carbon window,
 371 obtained from a FLUKA simulation (as described in the Supplementary Information). The longitudinal
 372 density profile of the plasma is chosen to match closely the measured electron density profile of the plasma
 373 discharge (plotted alongside Langmuir probe data in the inset of Figure 1): double peaked with maximum
 374 plasma density $n_0 = 1.78 \times 10^{12} \text{ cm}^{-3}$ (functional form provided in the Supplementary Information). All
 375 quantities in the simulations are normalized to the peak plasma density n_0 (associated plasma period
 376 $\omega_{\text{pe}}^{-1} = 13.29$ ps, and plasma skin-depth $c/\omega_{\text{pe}} = 3.98$ mm). The moving window has absorbing boundary
 377 conditions and dimensions $L_x \times L_y \times L_z = 3.5 \text{ cm} \times 3.5 \text{ cm} \times 40 \text{ cm}$, discretised into $879 \times 879 \times 10050$ cells.
 378 This yields a spatial resolution $\Delta x = 0.01 c/\omega_{\text{pe}} = 0.096$ mm. The simulations employ a time resolution
 379 $\Delta t = 0.0057 \omega_{\text{pe}}^{-1} = 43.7$ fs, fulfilling the 3D Courant-Friedrichs-Lowy condition: $c\Delta t < \Delta x/\sqrt{3}$. We employ
 380 8 macro-particles per cell (for each species), and utilize quadratic interpolation with first-order binomial
 381 current smoothing. The numerical parameters were carefully chosen after a convergence study with 2D3V
 382 PIC simulations.

383 **Acknowledgments.** We thank Prof. C. Joshi (UCLA), Dr. F. Albert (LLNL), Dr. C. Densham (STFC
 384 Rutherford Appleton Laboratory) and G. Marshall (AWE) for useful discussions, as well as T. Lev-
 385 ens (CERN) and Dr. T. Ma (LLNL) for supporting this experiment. This project has received funding
 386 from the European Union’s Horizon Europe Research and Innovation programme under Grant Agree-
 387 ment No 101057511 (EURO-LABS). The work of G.G. was partially supported by UKRI under grants
 388 no. ST/W000903/1 and EP/Y035038/1, while A.F.A.B. was also supported by UKRI (grant number
 389 MR/W006723/1). The work of P.J.B. and L.O.S. was supported by FCT (Portugal)-Foundation for Science
 390 and Technology under the Project X-maser (No. 2022.02230.PTDC) and Grant No. UI/BD/151559/2021.
 391 The work of D.H.F. and D.H. was supported by the U.S. Department of Energy under Award Number
 392 DE-NA0004144. The work of A.A.S. was supported in part by the Simons Foundation via a Simons Investi-
 393 gator Award. We also acknowledge funding from AWE plc., and the Central Laser Facility (STFC). FLUKA
 394 simulations were performed using the STFC Scientific Computing Department’s SCARF cluster. OSIRIS
 395 simulations were performed at LUMI-C (Finland) within EuroHPC-JU Project No. EHPC-REG-2021R0038.
 396 UK Ministry of Defence © Crown Owned Copyright 2024/AWE.

397 **Author contributions.** This project was conceived by G.G., R.B. and F.M. The experiment was designed
 398 by C.D.A., G.G., P.S., N.C. and R.B., and carried out by C.D.A., P.S., N.C., G.G., T.H., R.S., J.W.D.H.,
 399 P.J.B., S.B., F.D.C., A.G., D.H., S.I., V.S., T.V. and B.T.H. The data analysis was carried out by C.D.A.
 400 The manuscript was written by C.D.A., with input from G.G., R.B., N.C., F.M., L.O.S., B.R., P.J.B and
 401 S.S. Numerical simulations were performed by C.D.A., P.S., P.J.B. and L.O.S. Further experimental and

402 theoretical support was provided by A.D., I.E., D.H.F., A.F.A.B., A.A.S., J.T.G., B.T.H., S.S., H.C., T.D.
403 and R.M.G.M.T.

404 **Competing interests.** The authors declare no competing interests.

405 **Supplementary information.** Supplementary Information file provided.

406 section*Suppression of pair beam instabilities in a

407 laboratory analogue of blazar pair cascades

408 **Supplementary information**

| | | |
|-----|--|----|
| 409 | 1 Langmuir probe measurements of the plasma electron temperature and density profiles | 13 |
| 410 | 2 Optical emission spectroscopy of the argon plasma | 13 |
| 411 | 3 Design and characterization of the Faraday rotation probe | 15 |
| 412 | 4 Monte-Carlo simulations of the secondary beam generation | 16 |
| 413 | 5 Obtaining a value for B_0 | 17 |
| 414 | 6 Fitting analytical forms to the momentum phase space of secondary beam components | 18 |

415 **1 Langmuir probe measurements of the plasma electron
416 temperature and density profiles**

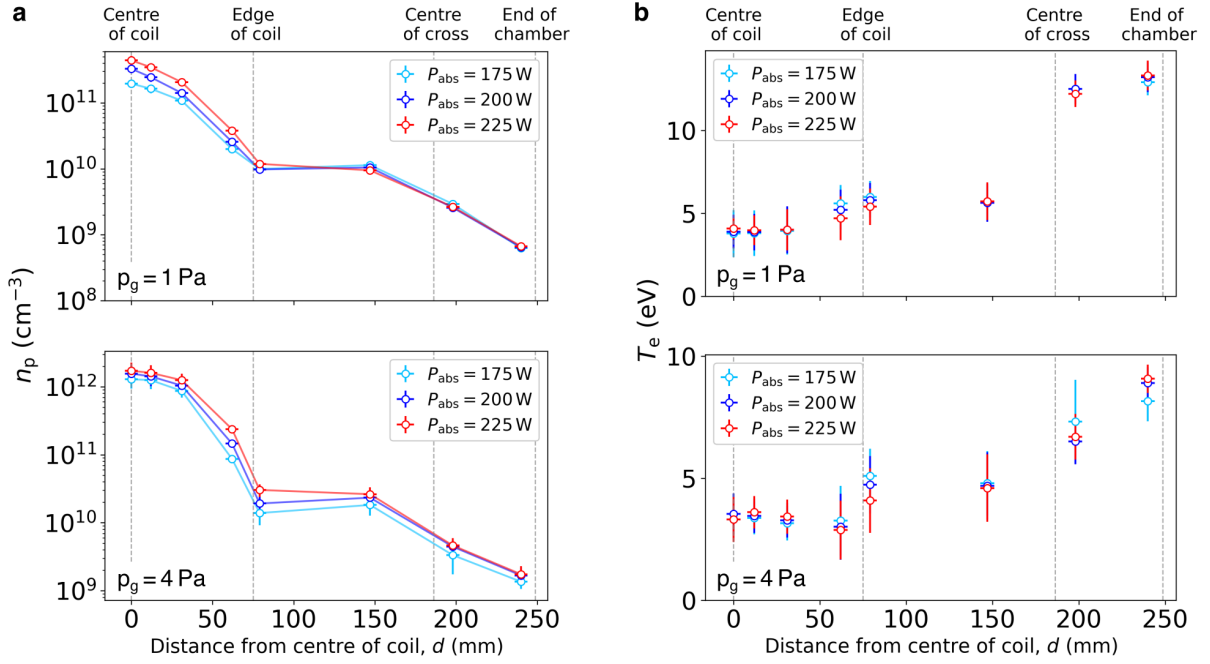
417 The plasma is characterized extensively for a range of argon gas fill pressures (p_g) and absorbed powers
418 (P_{abs}) prior to the experiment using a Langmuir probe. A commercially available Langmuir probe unit was
419 used (manufactured by Impedans, Ireland) with a single probe tip configuration in combination with an RF
420 compensation electrode. The probe tip is made of tungsten wire (length 4 mm, radius 0.195 mm), held in
421 position by an alumina tube (radius 2 mm). The probe tip is connected to the data acquisition unit via a
422 series of RF chokes to filter RF interference. The probe is inserted into the plasma at different positions along
423 the axis to obtain the electron density, ion density, electron temperature and energy distribution function.
424 The density and temperature profiles measured from the centre of the coil to the end of the discharge are
425 shown in Supplementary Figure 1, for absorbed powers: $P_{\text{abs}} = 175 \text{ W}, 200 \text{ W}, 225 \text{ W}$, and fill pressures:
426 $p_g = 1 \text{ Pa}$ and 4 Pa . The highest plasma densities are measured when the probe tip is positioned under the
427 centre of the inductive coil. At any given pressure, the peak plasma density scales approximately linearly
428 with the absorbed power. In particle-in-cell simulations the longitudinal plasma density profile is modelled
429 by:

$$n_p(z) = \frac{n_0 \left[e^{-(z-z_1)^2/(2\sigma_c^2)} + e^{-(z-z_2)^2/(2\sigma_c^2)} + n_{\min} \right]}{(1 + e^{-z/20}) (1 + e^{-(z+l)/20})}, \quad (5)$$

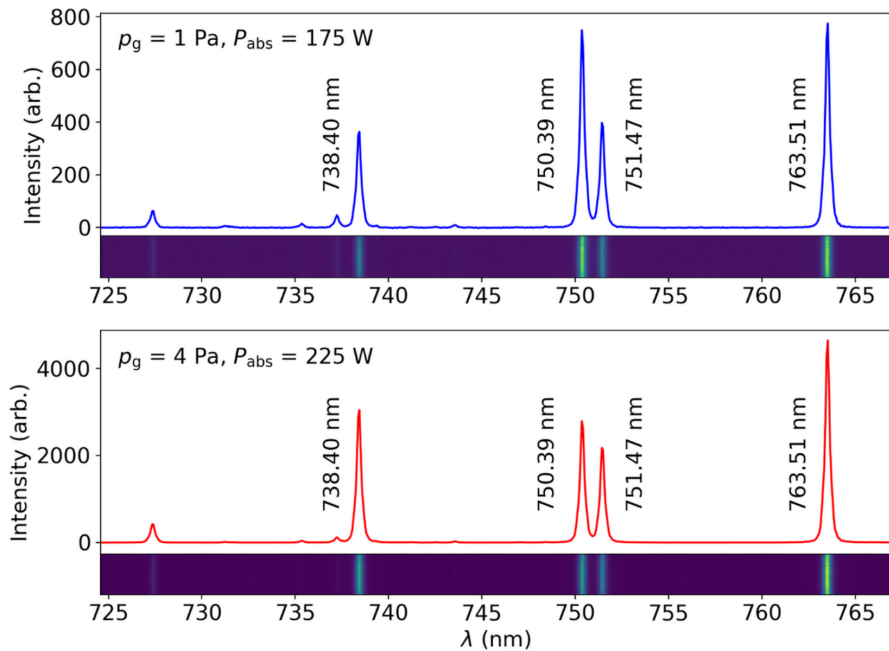
430 where $\sigma_c = 3.75 \text{ cm}$, $l = 87 \text{ cm}$, $n_{\min} = 0.02$, and $z_1 = 24.88 \text{ cm}$ and $z_2 = 61.88 \text{ cm}$ correspond to the centres
431 of the inductive coils. These parameters correspond to argon fill pressure $p_g = 4 \text{ Pa}$ and absorbed power
432 $P_{\text{abs}} = 240 \text{ W}$ (shown in Figure 1c of the main text).

433 **2 Optical emission spectroscopy of the argon plasma**

434 A Langmuir probe is too invasive to perform in-situ measurements during the experiment, so optical spec-
435 trographs of the plasma emission are collected and the spectra are compared with those obtained prior
436 to the experiment simultaneously with Langmuir probe measurements. Spectroscopic measurements were
437 performed using a Princeton Instruments Acton SpectraPro Czerny-Turner spectrometer coupled to a Hamam-
438 matsu Orca flash camera (with a 2 s exposure time). Light was collected from a 2 mm area at the centre of
439 the inductive coil using a collimating lens, which coupled the light into an optical fibre and transported it
440 to the slit of the spectrometer. The optical fibre is multi-mode with core diameter 105 μm and numerical
441 aperture 0.1. The slit width was 70 μm and the grating had a line density 600 g/mm. A calibrated white
442 light source was used to account for any spectral dependence on transmission/reflection of the optics or
443 spatial variation in the camera sensitivity. An argon-mercury lamp was used to calibrate the spectrum and
444 obtain the instrument function. The spectra were measured in the spectral region $\lambda = 725 - 770 \text{ nm}$, where
445 emission lines are prominent and variation in the line ratios is observed for different plasma conditions. Raw
446 data and lineouts for two sets of plasma conditions are shown in Supplementary Figure 2. Emission from
447 argon in the neutral state Ar(I) dominates the observed emission due to the low ionization fraction.



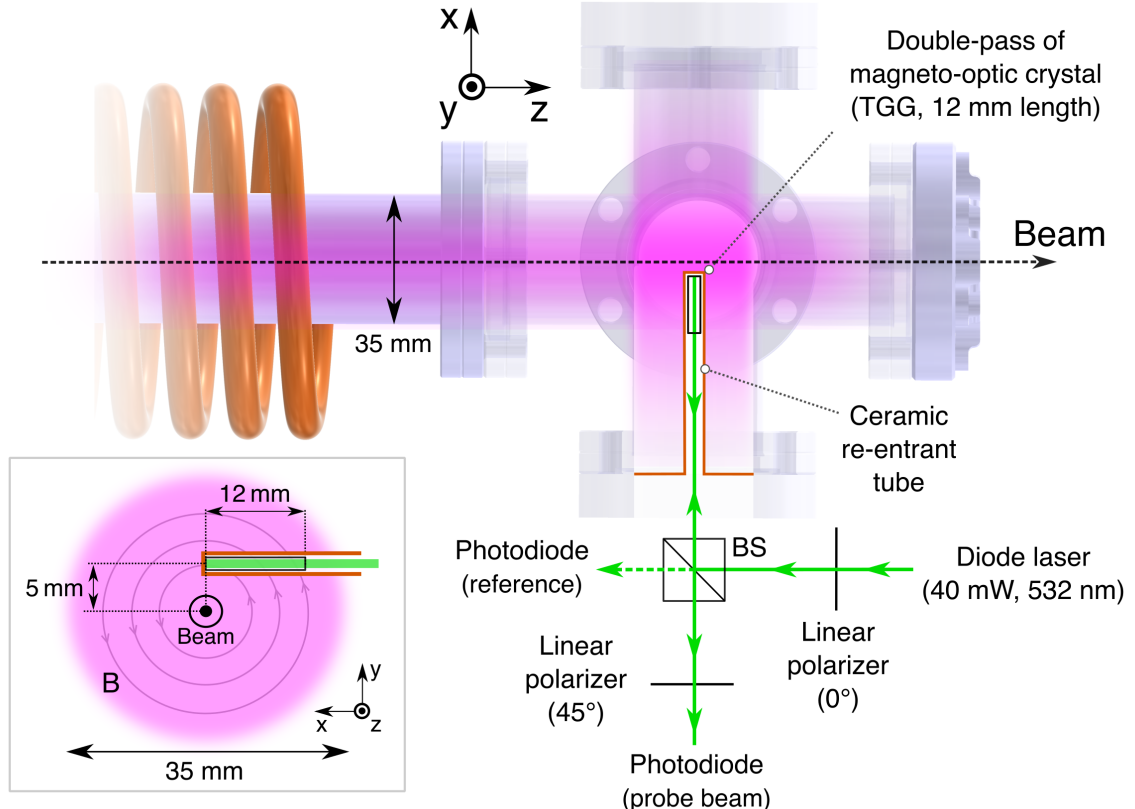
Supplementary Fig. 1 Langmuir probe measurements of the plasma density and temperature. (a) The plasma density, $n_p = (n_e + n_i)/2$ and (b) electron temperature, T_e , measured at different axial positions along the discharge relative to the centre of one of the inductive coils. Three power settings and pressure settings are measured: $P_{\text{abs}} = 175 \text{ W}$, 200 W , 225 W , and fill pressures: $p_g = 1 \text{ Pa}$ and 4 Pa . The vertical dashed lines correspond to: the centre of the coil ($z = 0 \text{ mm}$), the edge of the coil ($z = 75 \text{ mm}$), the centre of the six-way cross ($z = 186 \text{ mm}$), and the end of the chamber ($z = 245 \text{ mm}$).



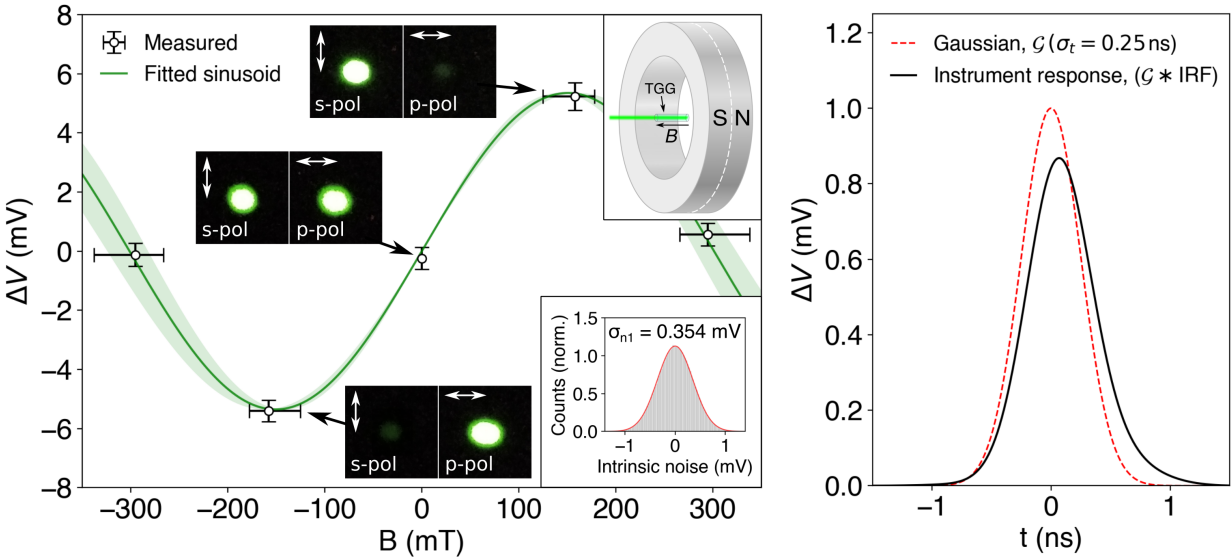
Supplementary Fig. 2 Optical emission spectroscopy of the argon plasma. The optical emission from the plasma at the centre of the inductive coil is measured in the spectral range $\lambda = 725 - 770 \text{ nm}$ for two sets of plasma conditions. Upper panel: $p_g = 1 \text{ Pa}$, $P_{\text{abs}} = 175 \text{ W}$, corresponding to a plasma electron density $n_e = (2.0 \pm 0.2) \times 10^{11} \text{ cm}^{-3}$ and temperature $T_e = 3.8 \pm 1.4 \text{ eV}$ measured before the experiment using a Langmuir probe. Lower panel: $p_g = 1 \text{ Pa}$, $P_{\text{abs}} = 175 \text{ W}$, corresponding to a plasma electron density $n_e = (1.7 \pm 0.1) \times 10^{11} \text{ cm}^{-3}$ and temperature $T_e = 3.3 \pm 0.9 \text{ eV}$.

3 Design and characterization of the Faraday rotation probe

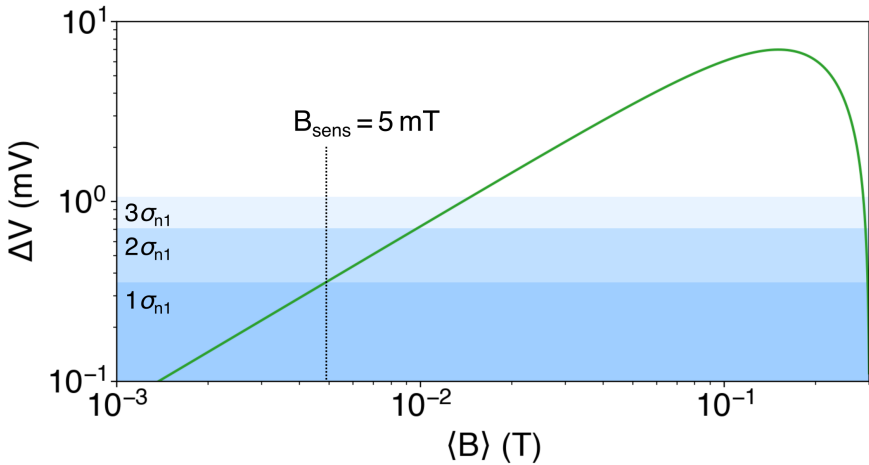
The setup of the time-resolved magneto-optic Faraday rotation probe is shown in Supplementary Figure 3. The inset in Supplementary Figure 3 also shows the arrangement of the Verdet crystal inside the plasma. Measurements of the Verdet constant, intrinsic noise and instrument response function are shown in Supplementary Figure 4. To calibrate the Verdet constant, the change in probe beam intensity (ΔV) is recorded when the TGG crystal is exposed to a permanent magnetic field (neodymium ring magnet K&J Magnetics RZ0Y0X0, 3" outer diameter, 2" inner diameter, 1" thickness). The field strength of the magnet is measured using a Hall probe. The intensities of the orthogonal polarization components change sinusoidally with the applied magnetic field strength, giving a Verdet constant $V = 217 \pm 15 \text{ rad T}^{-1} \text{ m}^{-1}$. The intrinsic electronic noise (of the photodiode and oscilloscope combination) is Gaussian-distributed with a standard deviation $\sigma_{n1} = 0.354 \text{ mV}$. For N multiple shots, the standard deviation of the mean signal is taken as $\sigma_n = \sigma_{n1}/\sqrt{N}$. The instrument response function is measured using mV-scale impulse signals produced by exposing the photodiode to an attenuated ultra-short femtosecond laser. The measured rise time is $t_{10-90\%} = 0.44 \text{ ns}$, and the instrument response function convolved with the temporal profile of the primary proton beam (Gaussian with $\sigma_t = 0.25 \text{ ns}$, rise time $t_{10-90\%} = 0.42 \text{ ns}$) is shown in Figure 4, demonstrating that changes in intensity on timescales of the beam duration can be detected. The magnetic field that corresponds to an observed change in probe beam intensity is shown in Figure 5. The 1- σ intrinsic noise results in an instrument sensitivity of $B_{\text{sens}} = 5 \text{ mT}$.



Supplementary Fig. 3 Design of the time-resolved magneto-optic Faraday probe. Green diode emission ($\lambda = 532 \text{ nm}$) is transported via an optical fibre to the position of the Faraday probe at the end of the plasma discharge. The laser is linearly polarized before it is passed through a 50:50 beamsplitter (BS). The transmitted beam (coupled into a fibre and measured using a photodiode) acts as a reference to changes in laser intensity. The reflected component is directed along a ceramic re-entrant tube to a TGG magneto-optic crystal suspended in the plasma. The rear surface of the crystal has a highly reflective dielectric coating, so the probe beam makes a double pass of the crystal, doubling the amount of Faraday rotation if the crystal is exposed to a magnetic field with a component along the direction of laser propagation. The probe beam makes a second pass of the beamsplitter and the transmitted component is passed through a second linear polarizer (with zero axis oriented at 45° to the first) before being transported to a photodiode which is used to measure changes in intensity resulting from Faraday rotation in the crystal. The inset shows the position of the probe crystal relative to the beam in the plane transverse to the beam axis.



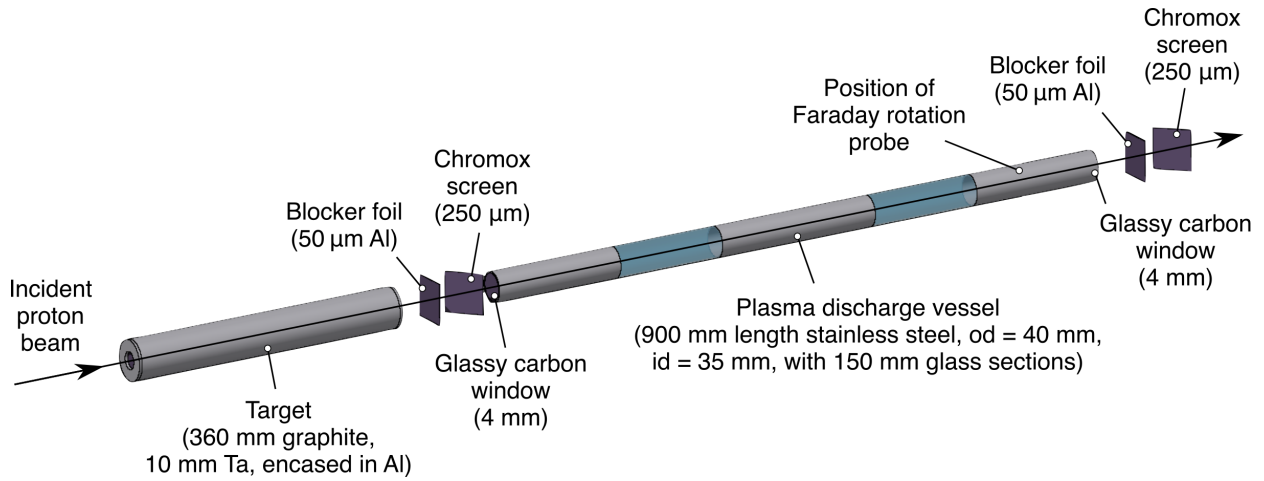
Supplementary Fig. 4 Performance of the Faraday probe. Left panel: The Verdet constant of the TGG crystal is measured by fitting a sinusoid to the change in probe beam intensity when exposed to a permanent magnet (as depicted in the upper left inset). The orthogonal components of linear polarization (labelled s-polarized and p-polarized) visibly change in intensity when the crystal is exposed to the magnetic field. The intrinsic electronic noise for a single measurement, which limits the probe sensitivity, is measured to be Gaussian with $\sigma_{n1} = 0.354$ mV, as shown in the lower right inset. Right panel: The instrument response function obtained from impulse measurements with an ultra-fast femtosecond laser is convolved with a Gaussian $\sigma_t = 0.25$ ns to show that changes in intensity on timescales of the beam duration can be detected.



Supplementary Fig. 5 Faraday probe sensitivity to magnetic fields. The change in probe beam intensity (ΔV) is plotted with respect to the mean magnetic field aligned with path of the laser beam through the crystal ($\langle B \rangle$): $\Delta V = V_0 [\cos^2(\langle B \rangle VL + 45^\circ) - \frac{1}{2}]$. The blue-shaded regions correspond to multiples of σ_{n1} , the intrinsic electronic noise for a single measurement.

4 Monte-Carlo simulations of the secondary beam generation

Monte-Carlo simulations of the secondary beam generation were performed using FLUKA to obtain the density and momentum distributions of the most abundantly produced secondary beam components (electrons, positrons, protons and pions). The simplified geometry of the experiment is shown in Supplementary Figure 6. The low-energy cutoff for particle transport in the simulation was 10 keV for $e^-/e^+/\gamma$ and 100 keV for hadrons. 10^5 primary protons were transported through the geometry, leading to agreement between the calculated and measured beam properties on the order of 1% in the regions of interest, as discussed in Ref. [1].



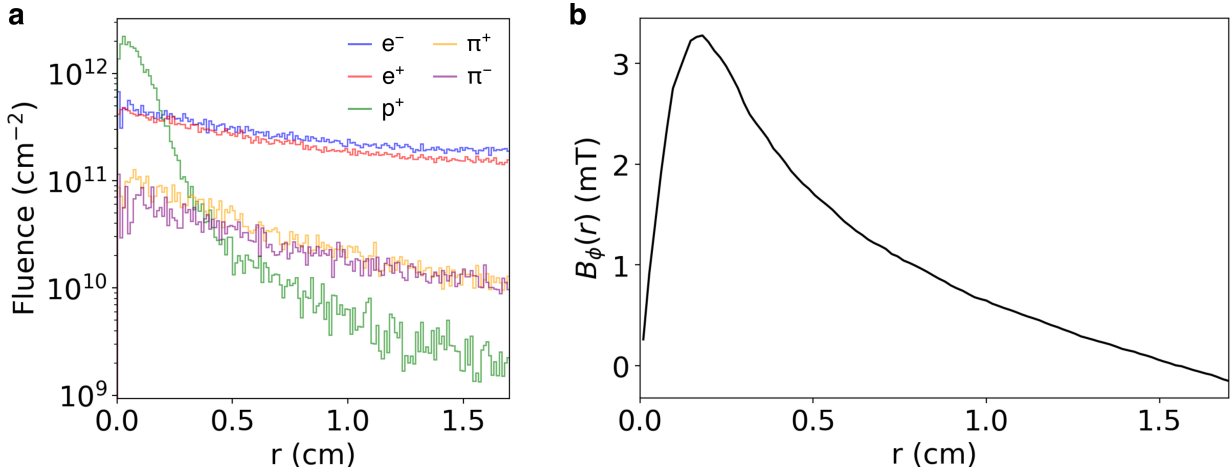
Supplementary Fig. 6 Simplified geometry of the experiment simulated using FLUKA. The plasma discharge vessel is modelled as a stainless steel tube with two glass sections where the inductive coils are located. The surrounding experimental area including the downstream beam dump as well as the concrete walls and shielding are also included in FLUKA simulations (not shown). The exact material compositions are used in all cases.

474 5 Obtaining a value for B_0

475 To obtain an upper bound on the instability's growth rate, the maximum inferred magnetic field measurement
 476 from the Faraday rotation diagnostic is compared with the expected measurement when no plasma is
 477 present. Given the density distribution of secondary particles at the probe position in a FLUKA simulation,
 478 the spatial distribution of the net current is used to calculate the magnetic field via Ampère's circuital law:

$$\oint_C \mathbf{B} \cdot d\mathbf{l} = \mu_0 \iint_S \mathbf{J} \cdot d\mathbf{S} = \mu_0 I_{\text{enc}}, \quad (6)$$

479 where I_{enc} is the current passing through an enclosed surface space, S , bounded by contour, C . The mag-
 480 nitude of the azimuthal magnetic field as a function of radius is shown in Supplementary Figure 7. The
 481 estimated magnetic field measurement in the absence of beam-plasma interaction is calculated from $B_\phi(r)$.



Supplementary Fig. 7 Obtaining the azimuthal magnetic field at the Faraday probe position in the absence of plasma using FLUKA simulations. (a) The particle fluence is plotted as a function of radius at the position corresponding to the Faraday probe inside the plasma vessel (obtained from a FLUKA simulation) for electrons (blue), positrons (red), protons (green), positive pions (orange) and negative pions (purple). (b) Ampère's circuital law is used to calculate the corresponding azimuthally-oriented magnetic field as a function of radius.

482 **6 Fitting analytical forms to the momentum phase space of**
 483 **secondary beam components**

484 From FLUKA simulations, the proton spectrum is split into the population that undergoes no signif-
 485 icant inelastic scattering ($N_{p^+} = 1.26 \times 10^{11}$, represented by a delta function in momentum space at
 486 $p = 440 \text{ GeV}/c$) and the population at lower momenta ($p < 440 \text{ GeV}/c$) generated in the hadronic cascade,
 487 which has a power-law momentum spectrum:

$$\frac{dN}{dp} = AN_{p^+} p^{k_1}, \quad (7)$$

488 where $N_{p^+} = 1.50 \times 10^{11}$, $k_1 = -0.81$, and the prefactor A is fixed by the normalization condition
 489 $\int_{x_{\min}}^{x_{\max}} \left(\frac{dN}{dp} \right) dp = 1$. The proton transverse momentum spread is Gaussian with a standard deviation
 490 $\sigma_{p_\perp} = 0.25 \text{ GeV}/c$. The density profile is Gaussian distribution in all dimensions:

$$\rho(r, z) = \frac{1}{(2\pi)^{3/2} \sigma_r^2 \sigma_z^2} \exp \left[- \left(\frac{r^2}{2\sigma_r^2} + \frac{z^2}{2\sigma_z^2} \right) \right], \quad (8)$$

491 with $\sigma_r = 0.11 \text{ cm}$ and $\sigma_z = 7.5 \text{ cm}$. Electrons and positrons are modelled in the spectral range $1 \text{ MeV} -$
 492 10 GeV with a multi-power-law distribution. The electron momentum spectrum is modelled by a triple-index
 493 power-law distribution:

$$\frac{dN}{dp} = AN_{e^-} p^{k_1} (p + p_{1,2})^{k_2 - k_1} (p + p_{2,3})^{k_3 - k_2}, \quad (9)$$

494 where $N_{p^-} = 5.48 \times 10^{12}$, $k_1 = -1.6$, $p_{1,2} = 0.012 \text{ GeV}$, $k_2 = 0.8$, $p_{2,3} = 0.25 \text{ GeV}$, $k_3 = -2.2$, and the
 495 prefactor A is fixed by the same normalization condition:

$$A \left[(k_1 + 1)^{-1} p^{k_1 + 1} (p + p_{1,2})^{k_2 - k_1} \left(\frac{p + p_{1,2}}{p_{1,2}} \right)^{k_1 - k_2} (p + p_{2,3})^{k_1 - k_3} \left(\frac{p + p_{2,3}}{p_{2,3}} \right)^{k_3 - k_1} \right. \\ \left. F_1 \left(k_1 + 1, k_1 - k_2, k_3 - k_1; k_1 + 2; -\frac{p}{p_{1,2}}, -\frac{p}{p_{2,3}} \right) \right]_{p_{\min}}^{p_{\max}} = 1, \quad (10)$$

496 where F_1 is the Appell hypergeometric function. The positron momentum spectrum is modelled by a double-
 497 index power-law distribution:

$$\frac{dN}{dp} = AN_{e^+} p^{k_1} (p + p_{1,2})^{k_2 - k_1}, \quad (11)$$

498 where $N_{e^+} = 4.27 \times 10^{12}$, $k_1 = 0.17$, $p_{1,2} = 0.19 \text{ GeV}$, $k_2 = -2.2$, and A is determined by

$$A \left[\left(\frac{p^{k_1 + 1} p_{1,2}^{k_2 - k_1}}{k_1 + 1} \right) {}_2F_1 \left(k_1 + 1, k_1 - k_2; k_1 + 2; -\frac{p}{p_{1,2}} \right) \right]_{p_{\min}}^{p_{\max}} = 1, \quad (12)$$

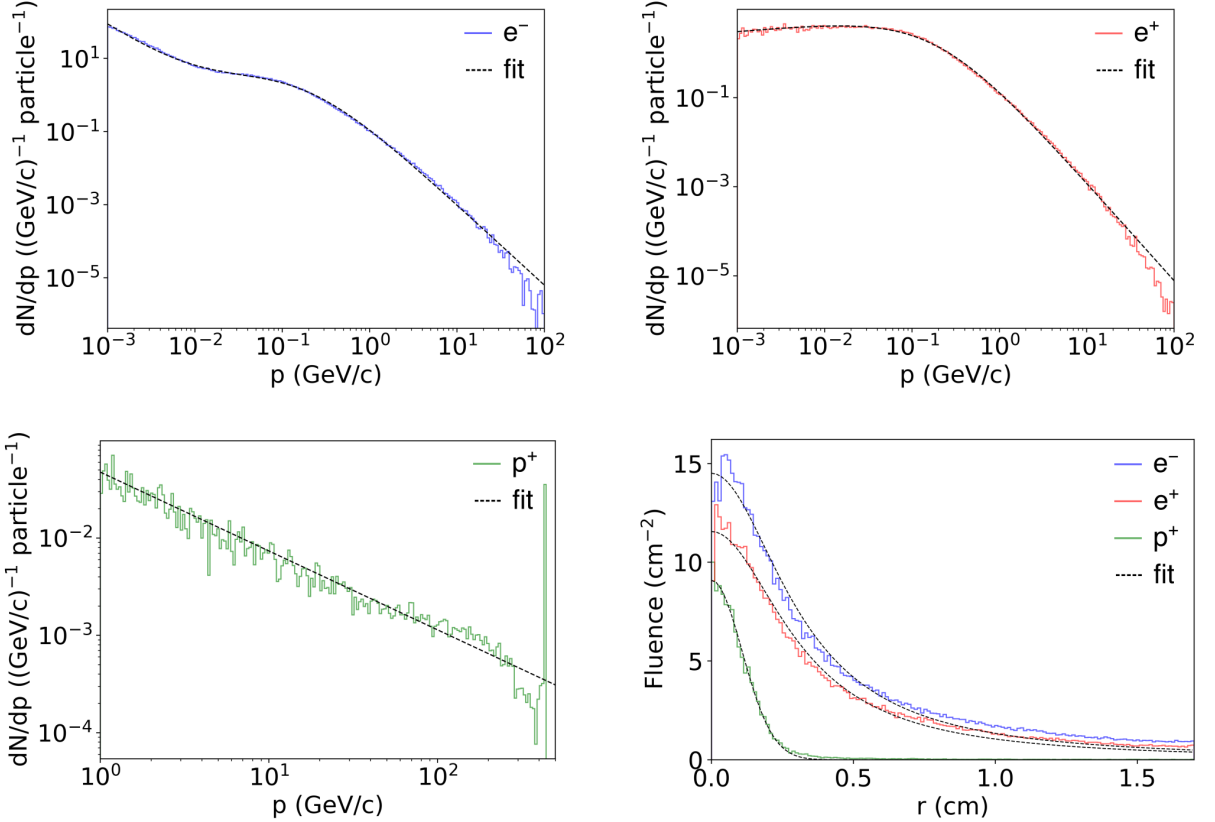
499 where ${}_2F_1$ is the hypergeometric function. The density profiles follow a Gaussian distribution longitudinally
 500 and a Cauchy distribution radially:

$$\rho(r, z) = \frac{1}{(2\pi)^{3/2} \sigma_z} \frac{\frac{1}{2} \Sigma_r}{(r^2 + (\frac{1}{2} \Sigma_r)^2)^{3/2}} \exp(-z^2/2\sigma_z^2), \quad (13)$$

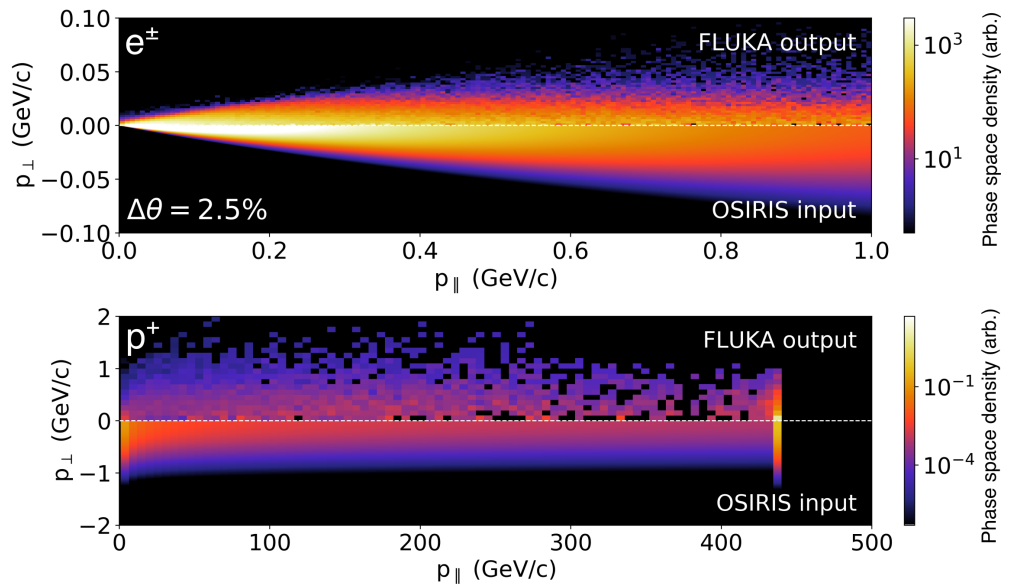
501 with $\sigma_z = 7.5 \text{ cm}$ and a radial half-width-half-maximum $\Sigma_r = 0.32 \text{ cm}$. In Eq. 1, the transverse momentum
 502 spread of pairs is defined $\Delta\theta \equiv \Delta p_\perp / p_\parallel = [\frac{1}{n_\pm} \int p_\perp^2 f_0 d\mathbf{p}]^{1/2} / \gamma_\pm m_e c$, where f_0 is the pair distribution
 503 function normalized by $n_\pm = \int f_0 d\mathbf{p}$. To obtain a value for $\Delta\theta$, the transverse momentum spread of pairs
 504 is fit to a Gaussian with a standard deviation that is a function of the longitudinal momentum:

$$\frac{d^2 N}{dp_\perp^2} = \frac{1}{2\pi \sigma_{p_\perp}^2} \exp(-p_\perp^2/2\sigma_{p_\perp}^2), \quad \sigma_{p_\perp} = p_\parallel \cdot \Delta\theta, \quad (14)$$

505 where $\Delta\theta = 0.025$ provides an appropriate fit (shown in Figures 8 and 9).



Supplementary Fig. 8 Fitted momentum and density distributions of beam species. The momentum and density distribution of electrons (blue), positrons (red) and protons (green), per incident primary proton, at the entrance of the plasma (after passing through the glassy carbon window), obtained from a FLUKA simulation and fitted to analytical forms (black-dashed).



Supplementary Fig. 9 Fitted momentum-space distributions of beam species. The fits to the full momentum-space distribution are shown for e^\pm (upper) and p^+ (lower). In each frame, the top half shows the momentum space obtained from a FLUKA simulation, and the lower half shows the analytical fitted function. For the e^\pm pairs, a Gaussian-distributed transverse momentum with $\sigma_{p_\perp} = p_{\parallel} \cdot \Delta\theta$ and $\Delta\theta = 0.025$ provides an appropriate fit. For the p^+ , $\sigma_{p_\perp} = 0.25 \text{ GeV}/c$.